THE IMPACT OF AEROSOLS AND LAND SURFACE PROPERTIES ON THE LIFTED TEMPERATURE MINIMUM IN THE NOCTURNAL ATMOSPHERIC BOUNDARY LAYER - FIELD AND LABORATORY EXPERIMENTS

A Thesis

Submitted for the degree of

DOCTOR OF PHILOSOPHY

By

Dhiraj Kumar Singh

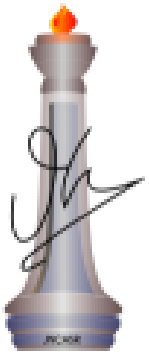

Engineering Mechanics Unit
Jawaharlal Nehru Centre for Advanced Scientific Research
(A Deemed University)
Bangalore – 560 064
OCTOBER 2013

Matha Pitha Guru Deivam

DECLARATION

I hereby declare that the matter embodied in the thesis entitled "**FIELD AND LABORATORY EXPERIMENTS ON AEROSOLS INDUCED COOLING IN THE NOCTURNAL ATMOSPHERIC BOUNDARY LAYER"** is the result of investigations carried out by me at the Engineering Mechanics Unit, Jawaharlal Nehru Centre for Advanced Scientific Research, Bangalore, India under the supervision of Prof. K. R. Sreenivas and that it has not been submitted elsewhere for the award of any degree or diploma.

In keeping with the general practice in reporting scientific observations, due acknowledgment has been made whenever the work described is based on the findings of other investigators.

Dhiraj Kumar Singh

CERTIFICATE

I hereby certify that the matter embodied in this thesis entitled "**FIELD AND LABORATORY EXPERIMENTS ON AEROSOLS INDUCED COOLING IN THE NOCTURNAL ATMOSPHERIC BOUNDARY LAYER**" has been carried out by Mr. Dhiraj Kumar Singh at the Engineering Mechanics Unit, Jawaharlal Nehru Centre for Advanced Scientific Research, Bangalore, India under my supervision and that it has not been submitted elsewhere for the award of any degree or diploma.

_____

Prof. K. R. Sreenivas

(Research supervisor)

ACKNOWLEDGEMENTS

I owe my gratitude to Prof. K.R.Sreenivas for his constant encouragement and support. His expertise in experiments and deep physical insights into the problem was crucial for my work. His immense patience with me helped me overcome difficult times. I especially value the freedom, both intellectual and otherwise, that he gave me for carrying out my work.

I am grateful to Prof. Ganesh Subramanian for a fruitful collaboration. His enthusiasm, abundant scientific inputs and constructive criticism during discussions helped me understand my research problem better and inspired me to work hard.

I thank Prof. Santosh Ansumali for extending help and support whenever necessary.

I am grateful to Prof. Rama Govindarajan for laying strong foundations through her course on fluid mechanics. I also thank Prof. Meheboob Alam for allowing me to use his lab for experiments.

I would like to thank binu for her full time support and help during various stages of my research work. Without her help, I may not have written papers and thesis. She also assiduously went through a pre-final draft of the thesis.

I thank my senior Mukund and batch mate Ponnu for discussions on experiments and theory. Their deep understanding of the problem helped me obtain a better perspective.

My PhD journey in JNC would have been extremely difficult without my friends (and sports buddies). It is my pleasure to thank everyone for making my stay joyful. I would like to thank Sunil for starting the culture of football in JNC without which I would have been at a complete loss. Thanks to everyone who has ever played football with me. Those times were memorable. I thank all my other friends in JNC.

I am also grateful to my lab mates Dinesh, Vivek, Rajapandian, JK, Shreyas, Devranjan, Vishwanath, Vybhav, Siddharth, Shashank, Bejan and Paaji for helping me in conducting the experiments.

I would like to thank the summer interns Sourab, Siddharth, Dhrub, Anirban, Harsha, Srikant and countless others for making the summers interesting and helping me with experiments.

I would also like to thank my friends in EMU Ratul, Gayatri, Dabade, Sourabh, Subbu, Ashish, Harish, Sumesh, Anubhab, Aditya, Saikishan, Rohith, Navaneeth, Milind, Reddy, Shahajhan, Ansari, Vicky, Croor, Jose, DK, PP, Rajesh, Saikat, Deepthi, Ujjain, Vinay, Priyanka and Srikanth for the entertainment, discussions and the occasional treats.

I would also like to extend my gratitude to Mr. Krishnoji, the fabricator, whose knowledge of fabrication and punctuality in delivering the product helped my work to a great deal.

I thank our Administrative officer, admin staff and academic staff for their support at various times. I thank the doctors of Dhanvantri, the hostel staff, the security staff and JNC transport staff for making my life easy in JNC.

I thank JNC and DST for providing me all the financial and infrastructural support to pursue my PhD and attend IRS-2012 in Germany. I am sincerely grateful to them.

Finally nothing would have been possible without the support from my family members. I will always be indebted to them.

ABSTRACT

The thesis focuses on the effect of radiation forcing by atmospheric aerosols on the nocturnal boundary layer close to ground. This study is on the anomalous temperature profile that develops after sun-set, under calm, clear-sky conditions, and which is characterized by the occurrence of minimum temperature a few decimeters above the ground. This phenomenon was first reported by Ramdas and Atmanathan in 1932, and is referred in the literature as '*Lifted temperature minimum'* (LTM), or '*The Ramdas effect'*. In the thesis, we present results from both field observations and laboratory experiments on this phenomenon. Temperature profile close to ground, in the nocturnal boundary layer, influences the surface energy budget, and plays an important role in many micrometeorological processes including the formation of inversion layers, and radiation-fog. Research work on this topic, by our group, has shown that a homogeneous atmosphere does not cause the preferential cooling necessary for the development of an LTM-type profile [Mukund *et. al.* (2010); Ponnulakshmi *et. al*. (2012a), (2012b)].

In the thesis a laboratory experimental setup is presented, in which the boundary conditions for the radiation is decoupled from those for conduction and convection. With this arrangement, the anomalous temperature profiles, similar to those observed in the field experiments (LTM profiles), were reproduced in the laboratory, under controlled conditions. Using this experimental setup, we show that radiation forcing due to suspended aerosols is the cause for the observed preferential hyper-cooling close to ground. The presence of aerosols is not normally accounted for in radiation models. However, by incorporating aerosol effects in radiation models, one can resolve the apparent conflict between observations of radiative cooling that produce LTM profile, and near-surface warming in a homogeneous atmosphere predicted by earlier radiation models (without aerosols). A radiative model involving aerosols also eliminates the need for an ad-hoc temperature slip at the ground, often assumed in atmospheric simulations [Mukund et al. (2013)]. In the thesis, we present a non-dimensional parameter, the Ramdas-Zdunkowski factor (R_{zf}), which determines the type of temperature profile that develops over the ground in the nocturnal boundary layer (NBL), depending on surface property and the prevailing conditions.

Another aspect of the LTM phenomenon is its stability [Larson (2001); Mukund et al. (2013)]. In this regard, in the first phase, experiments were carried out with naturally occurring atmospheric aerosols in the test section to characterize aerosol-induced radiation forcing. These experiments were done with stable stratification and coupled radiation-conduction boundary conditions. The radiative-conductive equilibrium temperature profiles, in an aerosol laden air layer, show that the radiation forcing due to aerosols results in a significant deviation from the linear conduction profile, unlike that for a homogeneous participating medium without aerosols. Notably, the magnitude and the sign of the deviation from the conduction profile, strongly depend on the boundary emissivities. In the next phase, in another set of experiments, with decoupled boundary conditions for radiation and conduction, effect of aerosol-forcing on the onset of convection was investigated. For the first time, in our experiments, we observe that the critical Rayleigh number for the onset of convection is enhanced by up to seven times more than that in the case of standard Rayleigh-Bénard convection. This has been explained by faster time response of the system (determined experimentally) and modified temperature profiles with reduced temperature gradient at the core region due to radiative-forcing. Even when the convection is observed, both the convective velocities and the temperature fluctuations are markedly lower due to radiation-stabilization compared to those observed in standard Rayleigh-Bénard convection (without radiation stabilization).

Apart from above laboratory experiments, the thesis further consists of results from the field experiments where the night-time vertical temperature profiles, humidity and wind speed were measured near the ground surface. Experimental setup consists of a mast carrying thermocouples to record temperatures at various vertical positions, portable Mini-LDV system for monitoring wind speed and aerosol-number density, a vertical laser sheet and Nikon- D90 digital camera for flow visualization. For monitoring humidity, a humidity sensor is mounted on the mast at a height of 25 cm above the ground. When turbulence levels were lower, convection rolls were obsorved in the LTM-region. In the field, radiation fog occurs at few decimeters above the ground rather than on the ground, also during this period the ground

temperature is much higher than the dew point temperature. Thus, we show that the presence of aerosols must be modeled for predicting the formation radiation fog. The vertical temperature profiles near the surface shows a marked difference before and during the fog period. The results presented in the thesis thus helps in the parameterization of transport process in the NBL, and highlight the need for accounting the effects of aerosols and ground emissivity in climate models and in modeling other micro-meteorological processes.

TABLE OF CONTENTS

LIST OF TABLES

LIST OF FIGURES

Chapter 1

1.1 Introduction

The part of the atmosphere which is directly influenced by the presence of surface and responds to surface forcing with a time scale of about an hour or less is termed as the atmospheric boundary layer [Stull (1988)]. During daytime, the earth's surface absorbs solar radiation, and it is at a higher temperature than the overlying air layers. This unstable stratification results in turbulent convection and a transfer of to heat to the overlying air layers [Stull (1988)]. Similarly in night, in the absence of advection, conventional wisdom dictates that, starting at sunset, the earth's surface being a good emitter in the infrared regime, cools radiatively, much faster than the overlying air layers, leading to a stable inversion layer over the surface [Stull (1988)]. But careful temperature measurements near the ground shows this is not actually the case. The air layers in fact, cool much faster than the ground resulting in a non-monotonic temperature profile typically known as the Lifted Temperature Minimum (LTM). The first report of the LTM was made by Ramdas and Atmanathan in 1932. In honor of the original discoverer, the phenomenon is referred to as the Ramdas paradox [Lettau (1979)]. A LTM-type profile may be characterized by the height of the minimum (the LTM height) and the difference between the ground temperature and the minimum (the LTM intensity). After Ramdas's initial observation, many researchers have shown subsequently that the occurrence of LTM-type profiles is quite common, and such profiles have since been observed in different parts of the world [Lake (1956); Lettau (1979); Mukund (2008); Oke (1970); Raschke (1957)]. The phenomenon was initially thought to be restricted to the tropics. However, it has since been shown to be quite robust, having been

observed all over the world over varied surfaces including rough soil, bare soil, Aluminum and concrete surfaces etc. under relatively calm cloudless conditions [Albani (1951); Brawand & Kohnke (1952); Lake (1956); Mukund et al. (2010); Oke (1970) ; Raschke (1957)]. The Rayleigh number calculated based on the height and intensity of the LTM is O (10^6), a factor of 1000 greater than the familiar critical threshold one would estimate [Chandrasekhar (1981)]. The apparent persistence of the LTM throughout the night, with no perceptible indication of an overturning instability, is again perplexing. It is thought that the stabilizing effects of cooling due to long-wave radiation may play a role, although there exists no quantitative prediction in this regard. Stability of LTM is one of the issues addressed as a part of this thesis.

Initial observations of the LTM were variously attributed to instrumentation error and advection of horizontal inhomogeneities (cold air from the horizontal area). However, more definitive experiments by Raschke (1957), and very recently by Mukund et al. (2010), have established that radiation plays a key role in the phenomenon. The Ramdas layer highlights in general the important but subtle role played by radiative processes in the stable atmospheric surface layer. Apart from its fundamental significance, the need to accurately resolve the temperature variation in the lowest meters of the atmosphere is also of particular importance in agricultural meteorology (the occurrence of frost and its adverse effect on crops [Lake (1956)], radiation fog and remote sensing for determination of true surface temperatures and surface emissivities [Snyder (1998)].

The initial observations were made by Ramdas & Atmanathan (1932) and his co-workers in 1932 in Pune. It was suggested that, the warming up of the ground is greater in the tropics

(due to higher solar insolation) and the ground cooling after sunset is not so rapid as to bring the surface temperature below that of the air layers. This is the reason for the initial skepticism that this phenomenon is restricted only to tropics. Further, the initial observational site was in a low-lying area and the drainage of air from the neighboring slopes could have affected the measured temperature profile. However, later measurements by other researchers confirmed that this phenomenon is not restricted to tropics alone and measurements over large fetch-to-height ratio sites showed the presence of LTM-type profiles. The suggestion was that radiation could play a role in determining the temperature profile.

1.2 Previous work (Observations)

Lake (1956) established the presence of this phenomenon over bare soil using thermometers and thermistors. The author put forward the mechanism for the occurrence of this phenomenon: "the air on a clear night must lose heat by some mechanism other than convection and conduction to the surface Radiation exchange may provide a mechanism for such cooling. In this case, the air would continue to lose heat by radiation until it reached radiative equilibrium with its surroundings and this process might be retarded or assisted by other heat transfer processes such as conduction and eddy diffusion. The author further summarized that the periodic fluctuations in the inversion layer could be due to a breakdown of the Ramdas layer. Experiments by Raschke (1957) confirmed the existence of this phenomenon beyond any doubt. Based on careful measurements, the author classified the nocturnal temperature profile into two types; (i) LTM-type profiles with minimum at some height above the surface and (ii) inversion profiles. The role of turbulence and wind speed on LTM characteristics were studied carefully. The observations indicated, when wind speeds

increase, the intensities of the minima decrease, and occasionally, the LTM-type profiles were replaced by inversion profiles. Further, LTM was vulnerable to turbulence. When the turbulence levels increased the minima disappeared but reappeared in a few minutes once the turbulence level came down. Oke (1970) reported observations over bare soil, rough soil, snow and grass close to the ground, on calm, clear nights, with sensitive instruments, and on a site where advective influence was small (fetch is around 180 m). The observations showed strong minima over bare soil (LTM intensity was 3^{o}C and height of minima was around 50 cm), and minima with weaker intensities over rough surface (LTM intensity being 0.3^{o}C). The striking feature of these observations was the occurrence of minima over snow (which has a high emissivity in the IR spectrum, and is an insulator), in contrast to previous experiments by Lutzke (1960) didn't observe LTM over snow. Over grass, the minimum in temperature occurred over the grass tip (there is a clear distinction between the grass tip minimum and the LTM-type profile; the grass tip minima is where the minimum temperature occurs at the tip of the blade instead of the root). In the case of the LTM, the grass tip should be considered as the 'true active surface' and the measurements done over that surface must help discriminate between an inversion or LTM. Further, the role of clouds was also studied. The intensity of minimum was found to decrease during the passage of a cloud cover. A special type of the minimum was observed when an altostratus cloud layer covered the sky and this was attributed to the warming of ground by the cloud. Recently, Mukund (2008) carried out very careful experiments to study the effect of thermophysical and radiative properties of the surface on the characteristics of the LTM-type profile. The experiments were carried over concrete (high emissivity, high thermal inertia), concrete + aluminum (low emissivity, high thermal inertia), foam (high emissivity, low thermal inertia) and foam +

aluminum (low emissivity, low thermal inertia) [Mukund et al. (2013)]. For instance, Funk (1960) measured radiative cooling in the developing boundary layer where the vertical extent of warming is likely restricted very close to the ground. Lieske & Stroschein (1967) measured radiative warming over snow where the vertical temperature profile shows a strong and deep inversion, and the radiative warming is likely spread over larger heights. Hoch (2005) also measured radiative warming over snow. The observation of an increase or decrease in cooling rate with height depends upon the relative locations of the layers under observation relative to the inversion top [Hoch (2005)]. Wind speed also plays an important role in determining the vertical distribution of radiative fluxes. Experiments by Prasanna (2012) have studied the role of radiation on convective transfer via experiments where the medium interacts with a radiative sink. However, the temperature of the top plate (polythene sheet) in these experiments is determined by the interaction of the polythene sheet with the overlying cold sink, and was not independently maintained as necessary in the LTM experiments described above. These experiments were mostly aimed at assessing the feasibility of using participating gases in passive cooling technology. The idea behind this method is to achieve cooling by exposing the participating medium that emits effectively in the atmospheric window, to a cold radiative sink. The effect of the surface emissivity of the bottom plate was also studied.The gist of the observational studies may be summarized as follows: The LTM phenomenon is real and robust, wind speed and turbulence levels affect the intensity of the minimum, and may even modify the profile from an LTM-type profile to an inversion and the response of the near-surface air layers to the passing clouds suggest that the phenomenon is radiative in origin, and that there is a strong interaction of low-lying air layers.

1.3. Previous work (Theory)

The currently accepted theoretical explanation for the origin of the LTM is the so-called VSN model proposed in 1993 [Vasudevamurthy et al. (1993)]. More detailed accounts of various aspects of the original theoretical formulation, and with the inclusion of additional factors such as turbulence, have since appeared elsewhere in a series of later papers [Narasimha (1994); Narasimha & Vasudevamurthy (1995); Ragothaman et al. (2001); Vasudevamurthy et al. (2005)]. The theory is essentially an application of the well-known flux-emissivity scheme for radiative heat transfer [Liou (2002)], in the form proposed by Garratt & Brost (1981) for ground with emissivity, to a water-vapor-laden atmosphere. The earlier calculation by Zdunkowski (1966a), although based on an inhomogeneous atmosphere, had to assume an unphysically low value of the molecular conductivity of air to explain the origin of this phenomenon. Hence, this model is not accepted in the literature. Although the Zdunkowski (1966a) claims that, with the correct thermal conductivity, the model continues to predict an LTM, the results haven't been published. Further, later field studies (those are aware of Zdunkowski (1966a) model) do not observe any haze layer near the ground [Oke (1970)]. The initial radiative slip, due to a preferential cooling of the near-surface air layers in an isothermal homogeneous atmosphere, is thus crucial to the prediction of the LTM. Further, such a sub-layer is predicted to occur only for a non-black surface [Vasudevamurthy et al. (1993)]. Both the cooling in the emissivity sub-layer and the resulting temperature minimum in presence of conduction are spurious effects resulting from a "band cross-talk" [Ponnulakshmi et al. (2012a)]. The latter error was discussed in detail in [Ponnulakshmi (2013)] and refers to, a physically incorrect coupling between the most opaque and most

transparent bands in the water vapor emission-spectrum due to the use of an erroneous broadband transmissivity for the reflected radiation.

The resultant stable inversion temperature profile, unlike the diurnal boundary layer, is not well understood [Edwards (2009)]. In the absence of clouds, and under calm conditions, turbulence can be subdominant and longwave radiation may play a dominant role in determining the vertical structure of the NBL. Radiation warming arises because, for air layers sufficiently close to ground, the cooling-to-space contribution is dominated by opaque-band exchanges with warmer overlying air layers [Edwards (2009a); Fleagle (1953)]. As noted by Edwards (2009a), starting at sunset, this latter length scale increases with time throughout the night. Hence, the time during which the measurements are done, assumes significance. For instance, whether the measurements have been done during the transitional period or a later period of boundary layer development becomes important, since the resolution required to access the region of radiative warming is different in the two cases.

1.4 Objective of present work

The prevailing explanation for LTM phenomenon [Vasudevamurthy et al. (1993)] is based on a broadband flux-emissivity scheme. The model predicts an LTM to occur only over non-black surfaces. It is shown herein that the prediction of an elevated temperature minimum is based on the aforementioned incorrect extension of the broadband emissivity scheme to non-black surfaces. A preferential cooling leading to a temperature minimum near the surface cannot occur in a homogeneous atmosphere [Ponnulakshmi et al. (2012)]. Heterogeneity on the length scale of the LTM is necessary to explain this phenomenon [Ponnulakshmi et al. (2012)].

For eighty years after the first observation of LTM by Ramdas & Atmanathan (1932), correct observational explanation about LTM had been missing. Steeneveld (2007) & Steeneveld et al. (2010) have measured radiative fluxes over grass at various heights. The maximum radiative cooling was observed immediately after the sunset, which then decreases with time, similar to the observation of Sun et al. (2003). In Steeneveld et al. (2010) study the first observation starts from 10 cm (over the vegetative growth) above the ground and next observation is at a height of 1.5 m. There are no temperature measurements in between, and hence we cannot comment on the LTM formation in their study. Other important point to be noted in Steeneveld et al. (2010) paper is the inability of MM5 radiation-model, in capturing cooling observed close to the surface.

In this thesis, through various experimental observations, the steep concentration gradient of suspended aerosols near the ground is proposed to be responsible for the preferential cooling.

1.5 Organization of thesis

This thesis contains six chapters, inclusive of the current chapter. A summary of the chapters have been provided below.

- In chapter 1, the current chapter, provides review of literature on Lifted Temperature Minimum (LTM). The previous work done on the LTM, both observations and theory, is discussed. Finally, the motivation for, and objectives of the present work are presented.
- In chapter 2, a laboratory experimental set up is developed that is capable of capturing the thermal structure of the NBL, close to ground, under various conditions. The effect of aerosol

on LTM, aerosol number density in the test section and "cloud events" are discussed. Finally, experimental observations and theoretical results have been compared.

- In chapter 3, experiments are carried in a traditional Rayleigh-Benard setup where the participating medium is confined between two parallel opaque plates leading to monotonic non-linear radiative-conductive equilibrium profiles. We have modeled the experiments. The theoretical results compare well with the experimental findings for an exponentially decaying aerosol concentration profile.
- In chapter 4, Radiative effect on the onset of instability is investigated experimentally in case of aerosols-laden, near-surface air layers. We present enhancement of stability in the LTM-region due to presence of radiatively participating medium. We also present the effect of radiation on classical Rayleigh Bernard convection for different optical depth of radiatively participating medium. We have also studied the stabilizing and destabilizing effect of radiation (sink and source) in aerosols-laden air layers. Further, we have estimated radiation time constant for aerosols-laden air layers before the onset of instability (stable regime).
- In chapter 5, the field experiments were carried out over a bare soil ground with surface properties is high emissivity and high thermal inertia. In addition to measures of vertical temperature profile, wind speed, humidity and image of aerosols were monitored. In the field experiments, convection in the LTM-region has been investigated. We present radiation fog in the field and roll of LTM-type profile on radiation fog. Further we discuss about the effect of rain on LTM-type profiles.
- In chapter 6, we summarize the conclusions of the thesis.

[1]Chapter 2

Experiments in the participating medium with decoupled boundary condition for radiation from that for convection and conduction

2.1 Introduction

Heat transfer processes in the nocturnal boundary layer (NBL) determine the vertical temperature profile, which in turn controls the formation of inversion layers, the occurrence of radiation fog [Mukund et al. (2010); Funk (1960)], and pollutant dispersal. The temperature profile also determines the surface energy budget through the boundary condition at the ground. In the absence of drainage flows (advection), after sunset it is generally argued that the ground being a good emitter, cools radiatively faster than the overlying air layers. Thus the faster cooling the ground leads to formation of stable inversion layer [Stull (1988)]. The expected transition in the temperature profile, through sunset, is shown in Fig. 2.1a; however, this is true only under certain conditions. Field experiments involving temperature measurements close to the ground, under calm (low wind and turbulence levels) and clear sky conditions (negligible cloud cover) instead indicate the transition shown in Fig. 2.1b [Ramdas & Atmanathan (1932); Ramdas (1953)]. Here, the air layers just above the ground are the fasted to cool after sunset, resulting in an anomalous temperature-profile with the minimum temperature occurring a few decimeters above the ground (level BC in Fig. 1b). In honor of the original discoverer, the phenomenon is referred

[1] Some part of the material presented in this chapter has been appeared in Q . J . R . Meteorol . Soc . (2013) http://onlinelibrary.wiley.com/doi/10.1002/qj.2113/pdf .

to as the Ramdas-paradox [Lettau (1979)] and the temperature profile itself has been referred to as the lifted temperature minimum (LTM). An LTM-type profile may be characterized by the height of the minimum (the LTM height) and the difference between the ground temperature and the minimum (the LTM intensity). Schematic of Ramdas layer is shown in Fig. 2.2. In the region bounded by curves AO and BC, one continues to observe the standard inversion profile. It is worth mentioning that although Ramdas's initial observations [Ramdas & Atmanathan (1932)] were met with skepticism [Geiger (1995)], researchers have subsequently shown that the occurrence of LTM-type profiles is quite common, and such profiles have since been observed in different parts of the world [Lake (1956); Mukund (2008); Oke (1970); Raschke (1957)]. The phenomenon is robust [Raschke (1957)], and LTM-type profiles have been observed over different types of surfaces including bare soil, snow, concrete and Aluminum [Mukund (2008); Mukund et al. (2010); Oke (1970)]. The nocturnal conditions required for the development of an LTM-type profile are (a) clear skies and (b) calm conditions with the wind speed (at the relevant heights) being around $1ms^{-1}$; under these conditions turbulence plays little or no role compared to radiation. The occurrence of such conditions is common in the tropics [Agarwal et al. (1995); Anfossi et al. (2005)]. For instance, Liu et al. (2008) report, from over 40 years of observation at a particular tropical site, that the frequency of occurrence of calm conditions is over 75% . The occurrence of an LTM-type profile implies that the near-surface air layers, rather than the ground, drive the cooling after sunset. This is in contrast to conventional wisdom that explains the onset of a stable inversion based on the ground driving the post-sunset cooling process [Stull (1988)]. Thus, the occurrence of an LTM-type profile changes the very nature of the surface boundary condition to be used in weather and climate models. A radiative

origin for the phenomenon has been suggested by earlier authors [Lake (1956); Raschke (1957)]. The sign of the near-surface radiative flux-divergence under stable conditions remains controversial and significantly, inversion and LTM-type profiles correspond to near-surface flux divergences of opposite signs. Many observations have recorded a cooling of the lowest air layers [Ramdas & Atmanathan (1932); Raschke (1957); Funk (1960); Oke (1970); Nkemdirim (1978); Sun et al. (2003)], though some indicate a warming [Lieske & Stroschein (1967); Hoch (2005)].

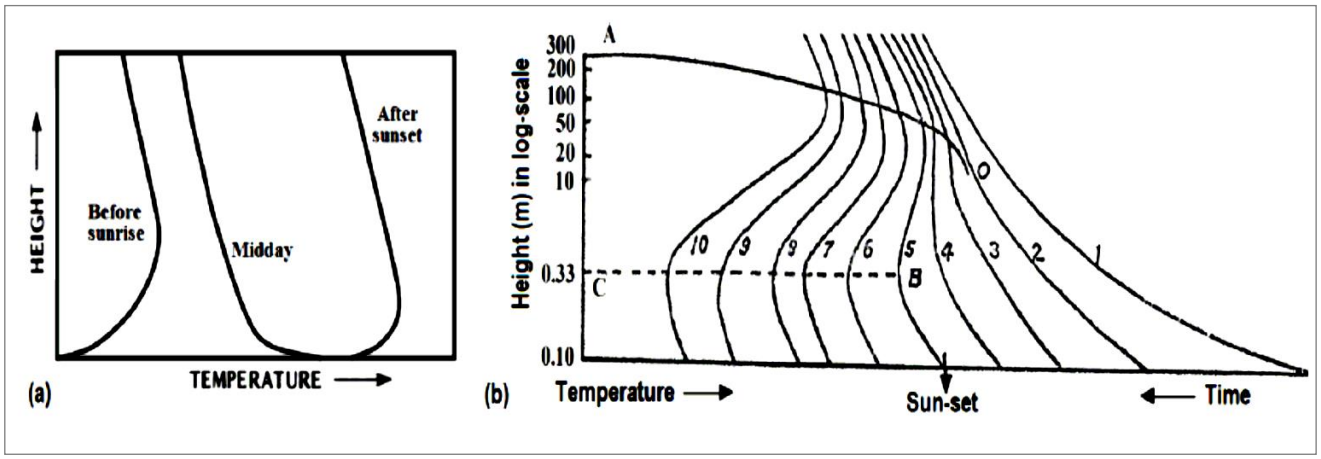

Figure 2.1 (a) Schematic of expected transitions in the temperature profiles during a day [Stull (1988)] and (b) Transitions observed in the temperature profiles across sunset [Ramdas (1953)] when measurements were made close to the ground in presence of an LTM; temperature profiles 1-10 correspond to the times 17.00, 18.00, 19.00, 19.30, 20.00, 20.30, 21.00, 23.00 3.00 and 7.00 respectively. The region bounded by curves AO and BC is the inversion profile. Line BC represents location of the minimum temperature, the height at which the minimum temperature occurs, remains more or less constant even as the height of the inversion layer grows with time by diffusion.

There appears to be no agreement in theoretical and modeling studies as well, with a warming predicted by some studies [Fleagle (1953); Räisänen (1996); Hoch (2005); Savijärvi (2006); Edwards (2009)], and a cooling by others [Andre and Mahr (1981); Garratt and Brost (1981);

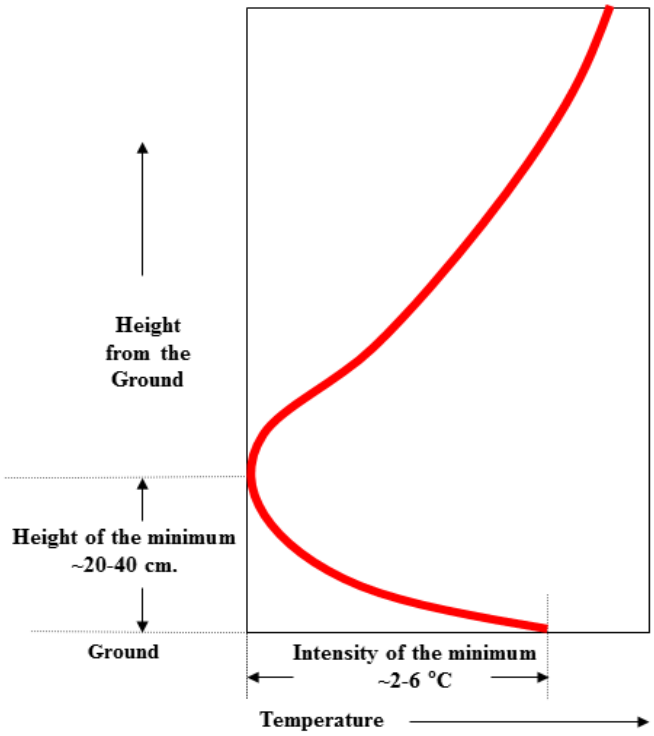

Figure 2.2 Schematic of Lifted Temperature Minimum (Ramdas layer).

Vasudevamurthy (1993); Ha and Mahrt (2003); Varghese (2003); Varghese et al. (2003b); Savijärvi (2006)]. Closer observation of those models that predict a cooling show that this lack of agreement is only apparent. Ha and Mahrt (2003), for instance, had to arbitrarily specify the ground temperature to be lower than the air temperature immediately above, in

order to obtain a (cooling) flux-divergence consistent with observations [Sun et al. (2003)]. Varghese et al., 2003b; and Savijärvi, 2006 adopt a similar approach. This cannot explain the persistence of an LTM-type profile where the air layers are cooler than the ground. On the other hand, Garratt and Brost, 1981 Andre and Mahrt 1981; Vasudevamurthy et al., 1993; and Varghese, 2003 obtain an intense near-surface cooling in a homogeneous atmosphere over non-black ground even in the absence of a temperature slip at the ground (the term 'homogeneous' refers to compositional homogeneity of the principal radiatively participating component). In fact, Vasudevamurthy et al. (1993) and Varghese (2003) regard this cooling as an explanation for the development of an LTM-type profile only over non-black ground. However, recent studies [Edwards (2009); Ponnulakshmi et al. (2009); Mukund et al. (2010); Ponnulakshmi et al. (2012)] have conclusively demonstrated that such preferential cooling cannot occur in a homogeneous atmosphere. The cooling predicted in the aforementioned studies arises from the use of an incorrect frequency-averaged transmittance for the reflected flux [Ponnulakshmi et al. (2012)]. Thus, the cooling in both simulations and theoretical studies is either due to an assumed slip, an insufficient vertical resolution leading to an apparent slip, or due to an erroneous treatment of the reflected radiation. In fact, the correct formulation predicts, a radiative warming near the ground [Edwards (2009)], and a decrease in the ground emissivity leads to a mild enhancement in this warming. The conditions leading to the spurious near-surface cooling, and the implications with regard to frequency-parameterized radiation schemes in general, have been examined in detail in Ponnulakshmi et al. (2012).

The above discussion reveals that though the correct theoretical prediction in a homogeneous atmosphere is that of a radiative warming near the surface, there remain

widespread observations of preferential radiative cooling near the ground both via temperature measurements [Ramdas And Atmanathan (1932); Lake (1956); Raschke (1957); Mukund (2008)] and via direct measurements of the difference between the (net) radiative fluxes [Funk (1960); Sun et al. (2003)]. In an earlier paper [Mukund et al. (2010)], support for a radiative origin for the LTM was obtained in the laboratory by reproducing LTM-type profiles in a specially designed laboratory set up. It was proposed that aerosols provided the heterogeneity needed for the observed preferential cooling near the surface. Experiments in the laboratory set up were used to provide some support for this hypothesis. Laboratory experiments were designed to explore the possibility of reproducing LTM-type profiles under controlled conditions. By doing so, one could eliminate the vagaries of weather, advection effects and conduct a controlled study of the phenomenon including its dependence on parameters like the surface emissivity, the effective sky temperature, and so forth. An intriguing issue related to the LTM is its apparent stability. The temperature variation close to ground in an LTM-type profile results in an increase in air density with height from the ground until the location of the minimum; the Rayleigh number for this layer is $O(10^5 - 10^7)$. Our observations indicate that the LTM height and intensity are nevertheless robust. While the laboratory experiments were originally expected to elucidate the origin of this apparent stability, it turned out, in light of the prevailing erroneous explanation [Vasudevamurthy et al. (1993)], that the most important role of these experiments was in elucidating the origin of the LTM phenomenon itself; in particular, providing evidence for the heterogeneity underlying the observed intense cooling in the field observations. Although there has been no previous attempt to simulate LTM-type profiles in the laboratory, there have been experiments that study the influence of radiation on convection and/or conduction.

Our laboratory setup was designed to capture the essential ingredients (clear skies and calm conditions) underlying the formation of the field LTM. The formation of an LTM-type profile is driven by radiative cooling due to an effective 'sky' temperature, T_{sky}, which is much lower than the temperatures prevailing in the inversion layer (by up to 20 K, [Ezekwe (1986)]). On the other hand, the local temperatures are the ones relevant to conduction and convective transport processes. Thus, the non-local character of radiation and the transparency of the earth's atmosphere act to de-couple the radiative boundary condition from those for conduction and convection. It is this de-coupled character of the local and non-local transport processes that must be achieved in the lab in order to reproduce an LTM-type profile. Such a decoupling is absent in the earlier efforts, [Goody (1964); Hutchison and Richards (1999)], that investigated the role of radiation in the context of the classical Rayleigh-Benard problem. The only work that attempts to incorporate a decoupled radiation boundary condition is that of Whitehead and Chen (1970) who examined the onset of penetrative convection in a fluid medium subject to a non-monotonic stratification, the stratification being setup by non-local radiative heating. However, unlike the present case, the fluid medium (mineral oil) was optically thick, and the radiation penetration depth was only of the order of centimeter. As a result, while radiation was crucial to obtaining the base-state, the stabilizing effects of the radiative source term were negligible, and the convection observed in the experiments were interpreted in terms of the usual Rayleigh number.

In this chapter, the LTM-type profiles obtained in the laboratory for various bottom boundaries are presented and compared with those obtained from previous experiments done in the field [Mukund (2008)]. The effect of aerosols on the LTM-type profiles is studied in

detail and the variation with seasons (pre-monsoon and during monsoon) is discussed. The "cloud effect" (blocking and unblocking experiments) where the radiation time constants for various emissivities of the bottom boundary as well as temperature of the radiation boundary and the bottom boundary has been characterized. Finally, the role of the test section's height for specific boundary emissivities is discussed.

2.2 Experimental set up

A schematic of the laboratory setup in which radiative boundary condition is decoupled at the top of a participating gas layer is shown in Fig. 2.3. The test section, which is the region of interest, contains a radiatively participating gas. It has a cross-sectional area of 1600 cm^2 (80 cm by 80 cm), and its height can be varied from 10 to 20 cm.

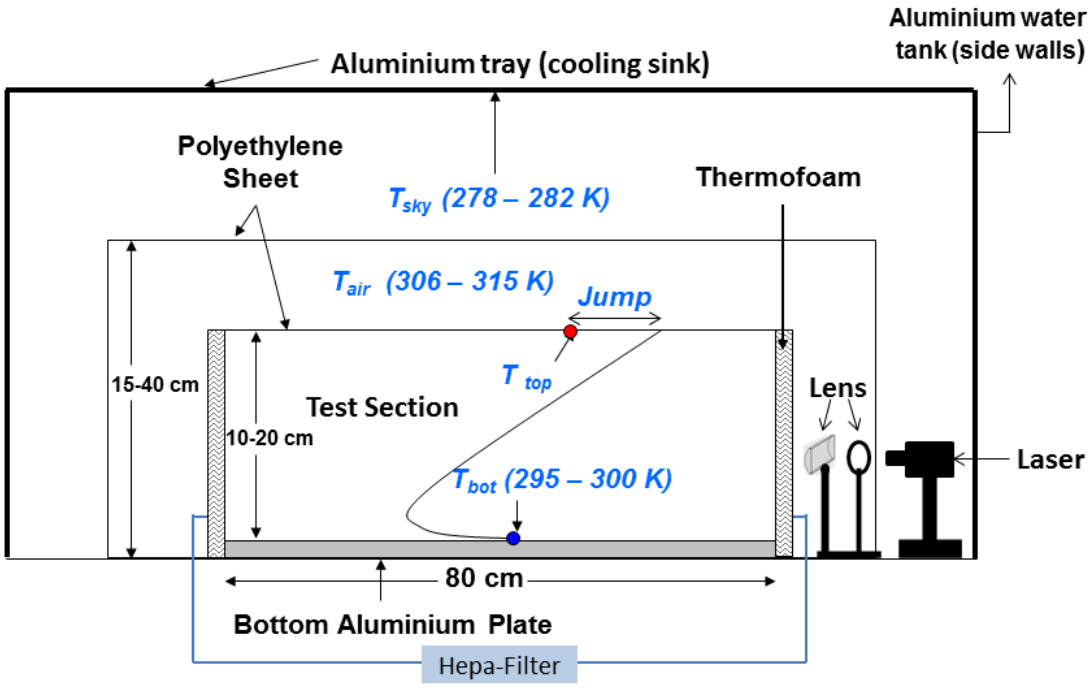

Figure 2.3 Schematic and notation of laboratory set up.

The test section contains ambient air, which may be regarded as the representative of the air layers near the ground. The bottom of the test section is made with 5 mm thick anodized aluminum plate. The bottom of this plate is in contact with water in a tank and the tank is provided with pipes for circulating water at an appropriate temperature, thus fixing the bottom boundary temperature of the test section. Both sides of the four walls of the test section are made of 40 mm thick thermofoam to prevent near-wall convection due to side wall heating. Further, the inner side of the walls of the test section is covered in Al foil (low emissivity- reflective) to reduce radiation from side walls. The ceiling of the test section is made of transparent polythene (with an effective transmissivity that is better than 80% in the 2 μm to 30 μm wavelength range). The test section is enclosed by another enclosure made of polythene, which having a cross section of 110 cm by 110 cm, and its height can be varied from 15 cm to 40 cm. The region between this polythene enclosure and the test section is the circulation section. With the help of a heater-blower unit, air is circulated at a specific temperature T_{circ} (measured at the outlet of the heater- blower unit), through this region. This fixes the temperature T_{top} of the top boundary of the test section. T_{top} provides the conduction or convection boundary condition for the upper boundary of the test section. Thus, by controlling the temperature of the bottom plate of the test section and that of the air being circulated through the circulation region, an appropriate temperature differential (stable or unstable) can be established across the test section. The entire unit (comprising the test section and the circulation region) is enclosed on all sides and at the top by an aluminum outer chamber, which acts as the radiation boundary condition, and provides the decoupled radiation forcing for the participating medium in the test section (Fig 2.3 and Fig 2.4). The four side walls are made by assembling four narrow aluminum-containers, while the ceiling

of the chamber is a shallow tray. The side walls of the chamber as well as on the top tray are provided with pipes for circulating chilled/hot water as required. By filling the side containers and the tray with water and circulating water at a desired temperature through the embedded pipes, the temperature T_{Sky} of the outer chamber or the radiation sink (source) can be controlled. The transparent polythene sheets of the circulation-section and the top boundary of the test section, allow the participating gas layer in the test section to interact radiatively with the aluminum chamber enclosure (a radiation source/sink). At the same time, due to the circulation of the gas in the circulation region, the upper boundary of the test section is maintained at a desired temperature and provides a conduction or convection boundary condition. Hence, in the experimental setup the conduction-convection and radiation boundary conditions are decoupled.

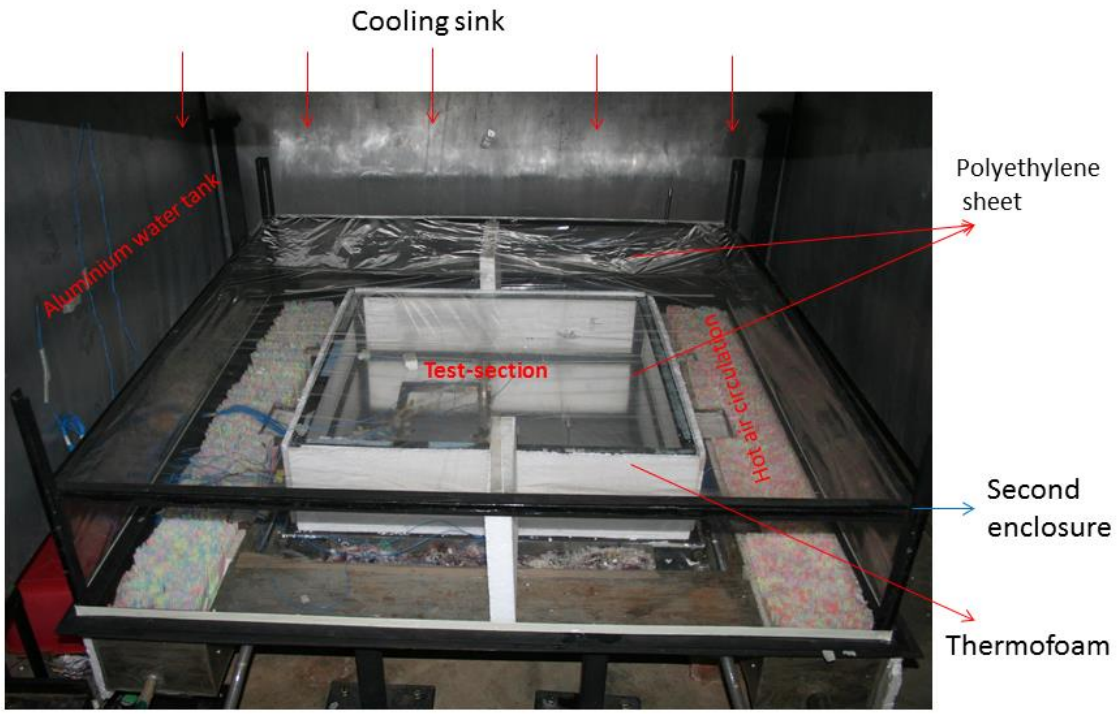

Figure 2.4 Laboratory experimental set up.

For the experiments, to demonstrate the formation of LTM profile, atmospheric air (ambient air) was used both in the test section, and for circulation through the circulation region. The temperature profiles in the test section were measured using K-type (Chromel-Alumel) thermocouples. Preliminary measurement indicated strong temperature gradients near the boundaries. This, combined with relatively small height of the test section, necessitated a special arrangement to measure the temperature profiles in the test section. Chromel and Alumel wires of each K-type thermocouple were butt-welded, i.e., were laid along a line (approaching from opposite directions) with their tips touching, and fused at the point of contact. This results in a junction, which is of the same thickness as that of the individual wire, which is 0.25 mm. These were stretched across a metal frame at different heights, in a single row. With the help of a traveling microscope, the junctions of each thermocouple were adjusted to the desired height above a plane surface. Thermocouples with flattened, disc shaped junctions (thickness 0.20 mm) were used to measure the temperature of bottom side wall and top boundary by sticking them to the surface with a layer of thermally conducting paste. A programmable data logger (HP-34970A) was used to record the temperatures at all measurement locations at regular intervals of time (5 s). The measurements were done by varying the emissivity of the boundaries of the test section either by coating them with black paint (high- emissivity surface) or by covering them with a highly polished aluminum sheet (low-emissivity surface).

A cooling sink at T_{sky} is provided by an aluminum outer enclosure containing an ice-water mixture. This enables the air layers in the test section to radiatively cool to the sink via the transparent polythene sheet (T_{sky} is 10-20 k lower than T_g). We refer to this set of

experiments as the 'three-plate experiments'; here, the conduction and convection boundary conditions are decoupled from the radiation boundary condition. When producing an LTM-type profile, the top boundary of the test section is maintained at a higher temperature, mimicking the nocturnal stable boundary layer, while the radiation sink (representing T_{Sky} "SKY-temperature") is maintained at a temperature lower than both top and bottom boundaries ($T_{Sky} < T_g$, T_{top}) of the test section. With the above arrangement, air in the test section is bounded by horizontal surfaces at temperatures T_g and T_{top}, with $T_g < T_{top}$, as in the nocturnal inversion layer. However, unlike almost all earlier experiments reported in the literature, and described above, air layers in the test section can, in addition, radiatively cool to the (ice-water) sink via the transparent polyethylene sheet (T_{sky} is 10-20 K lower than T_g; Ezekwe 1986).

The measurements were also done with different aerosol concentrations in the test section. The concentration of aerosols in the atmosphere varies with the season (low during monsoon and high during the pre-monsoon season). The air in the test section is sucked out through a port, and after filtering, is re-admitted into test section through another port. The duration of filtration is varied to get various aerosol concentrations. Air from the test section is filtered using an air filter (HEPA[2]). In the HEPA filter, there are two filters, one is pre-filter, which removes particles of size greater than 5 μm and the other is the main filter which removes all particles of size ≥ 0.3 μm. For flow visualization and measurement of number density of aerosols, we used a laser-sheet. For velocity measurement in the test section, we used Laser Doppler Velocitymetry (LDV). Details of the laser sheet and LDV are given in Chapter 5 under the Instrument Section.

[2] High Efficiency particulate Air

Experiments have been done with four different bottom boundaries of varying emissivity and thermal inertia. Following are the details of the chosen bottom boundaries:

1 Plate + aluminum foil – low emissivity and high thermal inertia

2 Plate + black paint - high emissivity and high thermal inertia

3 Plate + Thermofoam + black paper - high emissivity and low thermal inertia

4 Plate + Thermofoam + aluminum foil - low emissivity and low thermal inertia

2.3 Aerosols and their history

Aerosols, in general, being better emitters and absorbers than gases could play an important role in the cooling and heating of atmosphere. For modeling radiative transfer processes involving aerosols, we need to know their life cycle, chemistry, number density, and size distribution profiles in the atmosphere apart from their radiative properties. In recent study, has shown that natural aerosols can have an impact on the radiation budget [Charlson et al. (1992)]. For example, dust aerosols can heat the atmosphere (from the surface to about 5 km altitude) by absorbing solar radiation. Dust aerosols are good emitters and hence they can cool the atmosphere by increasing the emission of infrared radiation to space [Ramanathan et al. (2001)]. The presence of aerosols decreases the solar radiation reaching the surface of the earth and usually increases the solar radiation reflected to space. In the infrared region, the presence of aerosols increases the atmospheric radiation reaching the surface and decreases the atmospheric radiation emitted to space. It should be noted that aerosols are also good absorbers in the infrared region and hence the infrared radiation emitted by the surface will be absorbed by aerosols and reemitted to the surface. This will partly offset the reduction in solar radiation at the surface [Srinivasan (2002)].

Various groups have studied the vertical number-density profile of aerosols in the atmosphere. In a variety of situations, a layer of suspended particles exhibits a sharp decrease in particle concentration with layer height due to a balance between sedimentation and turbulent mass diffusion [Graf and Cellino (2002); Nielsen and Teakle (2004)]. Classically, the number density variation with height in suspension is described by a Rouse profile [Nielsen and Teakle (2004)]. In the stable, nocturnal boundary layer, aerosol concentration profiles, measured by LIDAR [Devara and Raj (1993)], show an increase in concentration towards the surface and can be fitted by Rouse profile. Most of these measurements are done a few tens of meters from the ground level.

2.3.1 Settling velocity of aerosols

The gravitational settling velocity of aerosol particles in homogeneous turbulent and random flow fields can be calculated from the average settling velocity in homogeneous turbulence of a small rigid spherical particle, subjected to a stokes drag force. The settling velocity is shown to depend on the particle inertia and the free-fall terminal velocity in still fluid. With no inertia, the particle settles on average at the same rate as in still fluid, assuming there is no mean flow. In a turbulent flow an aerosol particle is subjected to fluctuating drag forces produced by the turbulent velocity fluctuations in the surrounding fluid. For rapidly settling particles, the turbulent dispersion coefficient in the vertical direction may be up to twice of that in the horizontal direction owing to the ‘continuity effect’ in the compressible turbulent flow [*C.Sandy* (*1963*)].

The equation of motion for a small spherical aerosol particle of radius a and mass m will then be given by (C. Sandy 1963):

$mdv / dt = 6\pi a\mu\,(u(Y(t),t) - V(t)) + mg$;

$dv / dt = \alpha\,(u(Y(t),t) - V(t)) + w$;

where w is stokes settling velocity, terminal fall velocity in still fluid.

W=mg/6πaμ;

Stokes drag law can be replaced by a more general, nonlinear drag law independent of the instantaneous Reynolds number, R of the relative motion. If the dimensionless drag coefficient C_d is dependent only on R, the equation of particle motion for negligible inertia is

$C_d = 24\,(1 + 0.1\,R^{0.68}) / R$.

Particles of the size in the 0.01 μm to 10 μm range are commonly suspended in the air. The settling velocity of 0.1 μm particle is 4 $X10^{-5}$ cm/sec, for 1 μm is 4 $X10^{-3}$ cm/sec and for 10 μm is 0.3 cm/sec.

2.3.2 Aerosol Suspension (Rouse-profile)

Above certain critical shear stress conditions, sediment particles are maintained in suspension by the exchange of momentum from the fluid to the particle. The vertical sand mass flux at a specific height is defined as the mass passing a unit cross-sectional area in unit time. This flux can be obtained from the following equation if the corresponding particle concentration C and mean particle velocity u are known

Sediment concentration profile is given by: Q = $\int_0^{\delta} u.C\,dz$

In this study, Rouse's (1937) equation was selected from several suspended sediment transport equations for fluvial sand transport, because it is the simplest equation. Rouse's concentration profile was derived from the diffusion equation by considering the effect of the settling velocity of sand, and it was expressed as

$$\frac{C}{C_a} = \left(\frac{z}{z_a}\right)^{-p} \tag{2.1}$$

$$P = \frac{w}{k\, u_*} \tag{2.2}$$

Where C is the concentration at height z above the mean bed, C_a is the reference concentration at a height $z = z_a$, p is the Rouse number, w is the settling velocity, κ is the von Karman constant, and u_* is the bed shear velocity.

P = > 2 No suspension

0.8 < P = < 2 Incipient suspension

P = < 0.8 Full suspension

The data from field observations from Devara (1999) has been taken. The particle number density at height 50 cm from the ground is 10840 m^{-3} and p = 0.74. The rouse profile is fitted with Devara data and is shown in Fig. 2.5.

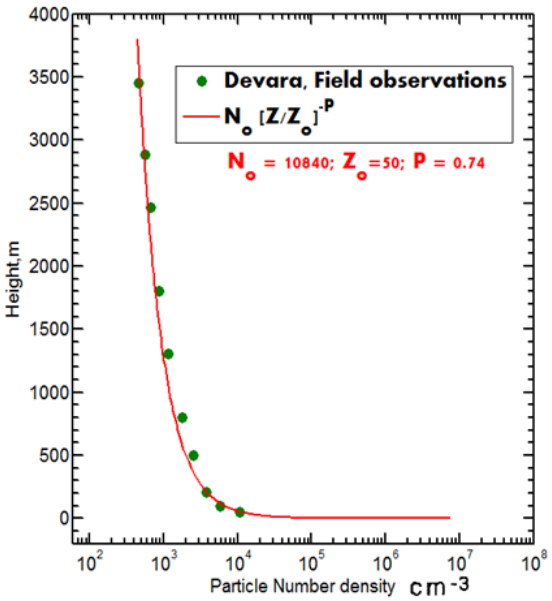

Figure 2.5 Vertical variation in the number density in a stable, nocturnal boundary layer reported by Devara [Devara And Raj (1999); Devara et al. (1993)] along with a Rouse profile fit to the data.

2.4. Data Processing and Uncertainty

The height of the thermocouple was monitored with a traveling microscope with a least count of 0.01 mm. K-type (Chromel-Alumel) thermocouple with bead- size of 0.3 mm were used for laboratory experiments. The bead size is also measured by a traveling microscope. The near-surface gradients and radiative cooling rates require the first and second spatial derivatives of the vertical temperature profile at any instant. Obtaining derivatives from experimental data is, however, unreliable in general and small errors are highly magnified in the process [Mukund (2008)]. Currently, the most widely followed procedure for differentiating experimental data is to first fit a set of polynomial or spline curves to the data and subsequently differentiating it analytically. Even so, the results cannot be guaranteed to be reliable. In spite of these difficulties, however, it is valuable to have at least a rough estimate of the near-surface gradients and cooling rates. Hence, two different procedures were used for filtering the vertical temperature profiles at any instant and a comparison of the function or derivative values obtained from these two procedures gave an idea of the errors involved in the estimates. In the first procedure, a Savitzky-Golay filter [Savitzky and Golay (1964)] with a span of seven points was used. A MATLAB-program was written to provide the filtered vertical profile as well as first and second derivatives. The other procedure was to fit the data with a least squares-spline (with quadratic polynomials) as implemented by the spap-2 routine in MATLAB and subsequent differentiation. As already stated, filtering hardly affects the temperature profiles themselves, and the two procedures agree to better than $\pm$ 0.1^{o}C. The uncertainty estimates for quantities derived from the first and second derivatives are discussed in the relevant sections. It must be noted that the two different

procedures are used only to get an idea of the errors involved in estimates. The filtered data points for the vertical temperature profiles (and quantities like gradients that are derived from the profiles) shown are the ones obtained by the seven point Savitzky-Golay filter. Emissivity of the black boundary (high emissivity) is 0.90 ± 0.02 and that of the aluminum boundary (low emissivity) is 0.04 ± 0.02. The transmitivity of the polythene sheet has been measured by using IR interferometer, which is more than 85% transparent to IR radiation.

2.5 Results

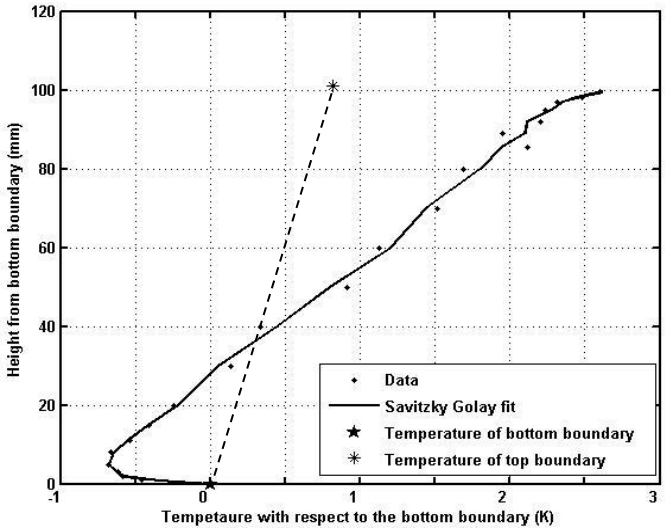

Figure 2.6. Typical profile obtained in the laboratory showing lifted temperature minimum [Mukund (2008)].

Punit Tiwari (2006) and Mukund (2008) have reproduced LTM-type profiles in the laboratory and typical LTM-type profile shown in Fig. 2.6. Mukund (2008) has also done field experiments with various surfaces parameters. The properties of modified surfaces have been shown in table 2.1. He has obtained highest intensity of minimum in case of low emissivity and high thermal inertia surface parameter and an inversion profile is obtained in case of high emissivity and high thermal inertia (thermofoam) and shown in Fig. 2.7. For the

laboratory experiments, similar surface parameters have been taken as in field experiments and results will be shown in next section.

Table 2.1. Properties of modified surfaces [Mukund (2008)]

	Surface	Property	Emissivity
1.	Concrete	High ε, low β	0.9
2.	Concrete + Al	Low ε, low β	0.05
3.	Thermofoam	High ε, high β	0.9
4.	Thermofoam + Al	Low ε, high β	0.05

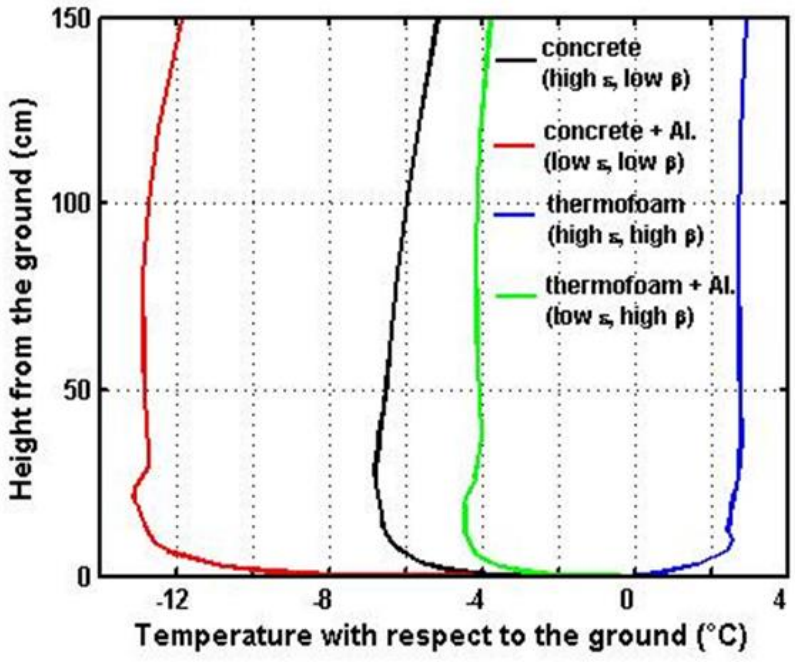

Figure 2.7 The vertical temperature profiles near the earth surface at various surfaces [Mukund (2008)].

2.5.1 Types of bottom boundaries

Experiments have been done with four different bottom boundaries of varying emissivity and thermal inertia. The typical temperature traces in the test section are shown in Fig. 2.8. Temperature at various heights in the test section is plotted with respect to time. Before t=2.33 min air layers in the test section including top and bottom boundary are in conductive equilibrium state. At t=2.75 min, the cooling source (sky) is turned on and after ~ 20 min, the new steady state is achieved. During this period (23-40 min), data have been taken to plot temperature profile, temperature gradient and cooling rate.

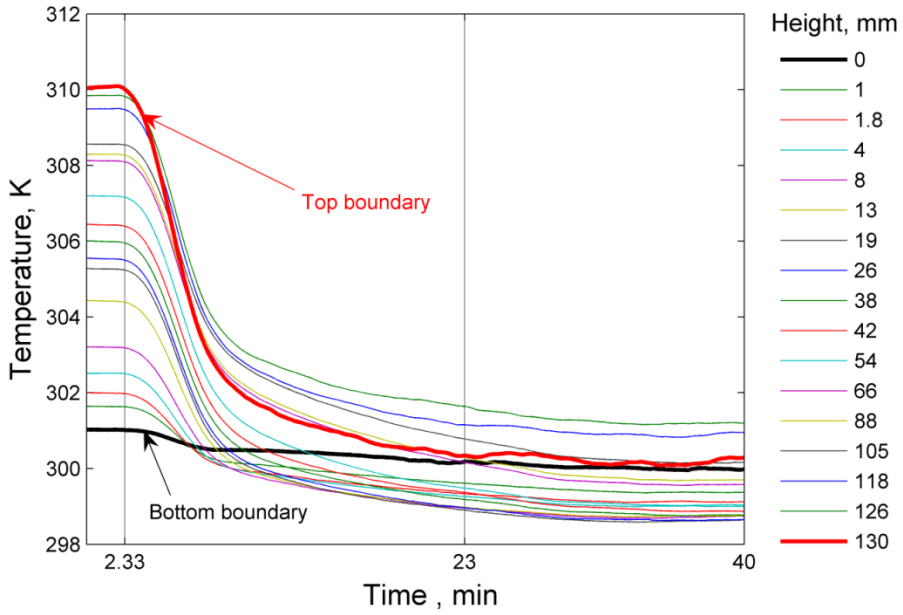

Figure 2.8. Temperature of air layers in the test section, with respect to time, at various vertical positions. Red and black lines represent the temperature of the top and bottom boundary respectively.

In Fig. 2.9, vertical temperature profiles in the test section with respect to height have been plotted for various bottom boundaries. The LTM-type profile has been observed in the case

of bottom boundary with high emissivity and high thermal inertia, and intensity of minimum is 1.2 K. The temperature profile on the 'Plate + Al' bottom boundary shows that lowering the emissivity increases the intensity of the minimum. Due to high cooling rates, the profile over the 'foam' surface is no longer an LTM, but an inversion with the minimum temperature at the bottom boundary. A comparison of the profiles on the 'Al+foam' and 'foam' again highlights the role of boundary emissivity. A lower emissivity on the 'Al+foam' surface changes the inversion profile into a very weak LTM profile. Therefore, observations are in agreement with the field study measurement in Mukund (2008).

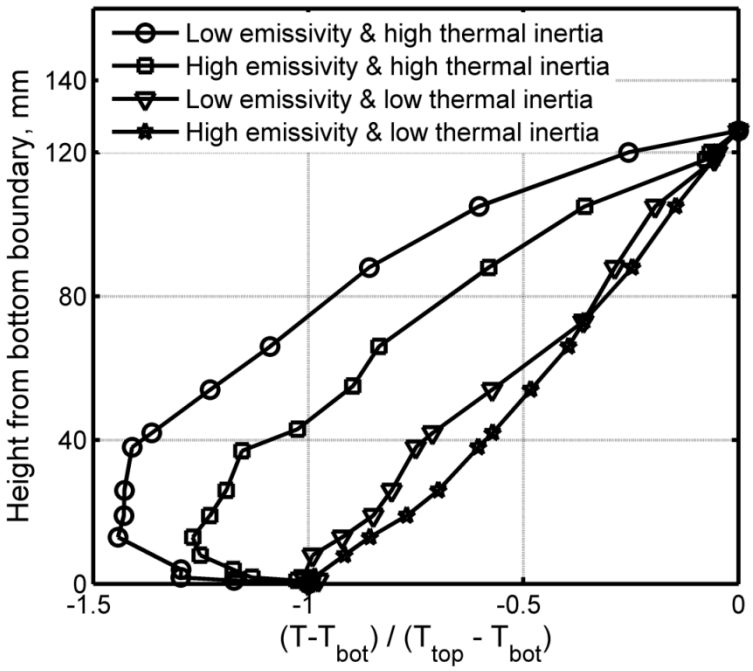

Figure 2.9 Normalized temperature profiles over various bottom boundaries plotted with respect to height. T_{Sky} is held at 280 K while T_g is at 300 K and T_{top} is temperature of air at 126 mm (temperature of last thermocouple in air in the test section). Except over the thermofoam bottom boundary, an LTM-type profile is observed on all other bottom boundaries. The maximum intensity is observed over the bottom plate covered with low-emissivity aluminum foil.

2.5.2 Radiative flux divergence and temperature gradient near the bottom boundary

To analyze the experimental profiles, we begin with the heat equation

$$\frac{\partial T}{\partial t} = k\frac{\partial^2 T}{\partial z^2} + \frac{1}{\rho C_p}\frac{\partial F}{\partial z} \qquad (2.3)$$

Here, T is the temperature, t is time, z is the vertical coordinate measured from the bottom boundary, k is the thermal diffusivity, and ρ and C_p are the density and specific heat capacity of air, respectively. $\partial F/\partial z$ represents the source term due to radiation and an estimate is obtained by determining $\partial T/\partial z$ and $\boldsymbol{\partial}^2\mathrm{T}/\boldsymbol{\partial}\mathrm{z}^2$ from the temperature data. The source term arises due to the radiative flux-divergence and helps to maintain a non-linear vertical temperature profile. From our observation of the temperatures at various vertical positions, a curve is fitted to the vertical temperature data to obtain smooth temperature profiles at each instant. The second derivative of this profile at a particular instant yields the conductive term ($\kappa\ \partial^2\mathrm{T}/\partial\mathrm{z}^2$). Similarly, taking the difference at each height between two consecutive profiles (in time) and using the time interval between the two profiles gives an estimate of ($\rho c_p\ \partial\mathrm{T}/\partial\mathrm{t}$). With these two terms and using equation (2.1), we estimate the radiative source term ($\frac{1}{\rho C_p}\frac{\partial F}{\partial z}$). Also note that $\frac{\partial T}{\partial t}$ term is much smaller than ($k\frac{\partial^2 T}{\partial z^2}$) term. The temperature gradient as a function of height is presented in Fig. 2.10, while the radiative flux-divergence obtained, as a function of height, is shown in Fig. 2.11 for various bottom boundary emissivities.

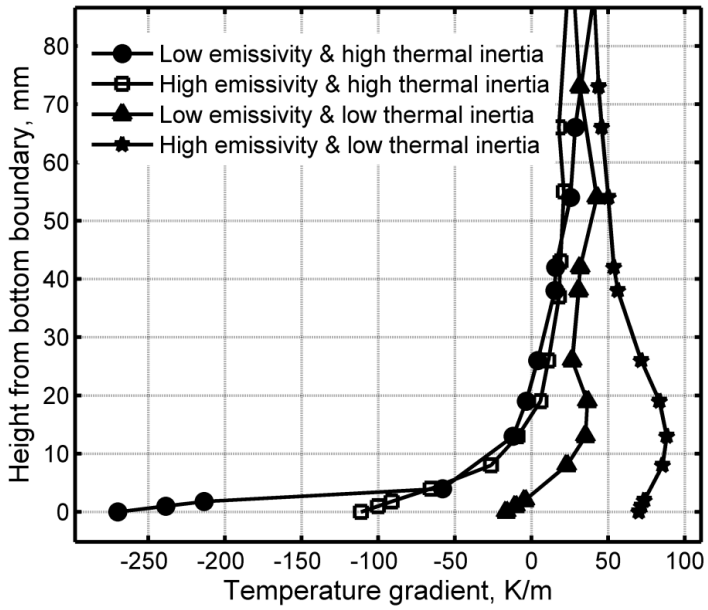

Figure 2.10 Temperature gradient profiles observed over different types of bottom boundaries. In all cases, except over the high-emissivity thermofoam surface, air cools the bottom boundary. In the case of high emissivity thermofoam surface an inversion profile is observed and air is being cooled by the bottom boundary

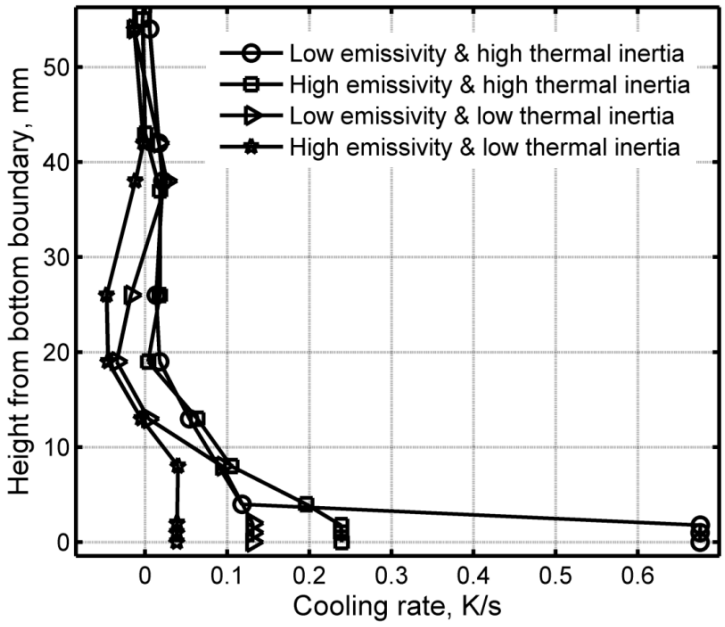

Figure 2.11 Radiative flux divergence profiles observed over different types of the bottom boundaries. Near the bottom boundary cooling rates estimated from the data, showing very high cooling rates confined to within a few centimeter from the bottom boundary.

The near bottom boundary temperature gradient over the black (high emissivity) bottom boundary is thus typically 110 K/m and decay over the length scale O (20 mm). The temperature gradient over the 'Plate+Al' (low emissivity) bottom boundary is higher at around 270 K/m near the bottom boundary and decay over the length scale O (20 mm). The temperature gradient over the 'Plate+foam+Al' (low emissivity) bottom boundary is quite lower, being around 20 K/m near the bottom boundary and decay over the length scale O(20 mm). The temperature gradient over the 'Plate+foam+black' (high emissivity) bottom boundary is very low with opposite sign at around 60 K/m near the bottom boundary and decay over the length scale O (20 mm).

Near the bottom boundary cooling rate over the black (high emissivity) bottom boundary is 0.24 K/s and decay over the length scale O (20 mm). The cooling rate over the 'Plate+Al' (low emissivity) bottom boundary is higher at around 0.68 K/s near the bottom boundary and decay over the length scale O (20 mm). The cooling rate over the 'Plate+foam+Al' (low emissivity) bottom boundary is lower at around 0.12 K/s near the bottom boundary and warming beyond 15-25 mm. The cooling rate over the 'Plate+foam+black' (high emissivity) bottom boundary is quite lower at around 0.02 K/s near the bottom boundary and warming beyond 15-25 mm approximately. In Table 2.2, the results of temperature profiles over surfaces with differing values of the surface emissivity and thermal inertia are summarized. A comparison of the profiles over the different surfaces shows that (Fig. 2.9) lowering the thermal inertia decreases the intensity of the minimum, to the extent that the minimum may be replaced by an inversion. This is consistent with the observations of Oke 1970, who found that much calmer conditions were required for the development of the LTM on snow as

compared to soil. Further, the intensity of the minimum developed over snow was weaker and at a lower height compared to the bare soil.

Table 2.2 Summary of the various surfaces over which observations were made in Laboratory and comparison with field experiments. The field observational data has been taken from Mukund (2008).

Type of surface		**Boundary properties**	**Intensity of LTM**	
Laboratory	Field		Lab	Field
Aluminium plate with black paint	Bare Concrete patch	High emissivity with $e_g = 0.91$, & high thermal inertia	0.68 K	2 - 7 K
Aluminium plate with Aluminium foil	Concrete covered with Aluminium foil	Low emissivity with $e_g = 0.05$, & high thermal inertia	1.2 K	7 – 13 K
Aluminium plate with thermofoam with brown paper as its top surface	Concrete covered by thermofoam With brown paper as its top surface	High emissivity with $e_g = 0.89$, & low thermal inertia	No LTM Inversion	No LTM Inversion
Aluminium plate with thermofoam with Aluminium Foil as its top surface	Concrete covered by thermofoam with Aluminium foil as its top surface	Low emissivity with $e_g = 0.05$, & low thermal inertia	0.2 K	2 – 5 K

Lutzke reported observing the LTM over soil, but not over snow [Oke (1970)]. Lowering the emissivity, on the other hand, increases the intensity of the minimum. This effect of emissivity of the bottom boundary of the test section is confirmed in the laboratory experiments. LTM type profiles were obtained in a specially designed laboratory set up described in section 2.2, showing that the phenomenon can be reproduced by purely radiative

means. Such profiles have not been observed in earlier investigations of radiative-conductive equilibria in the parallel-plate geometry, as there was no decoupling of the radiation and conduction-convection boundary conditions crucial to the establishment of a LTM profile. Here, it is worth noting the quantitative differences in lab-LTM characteristics, when compared to field observations:

(a) The lab-LTM intensity over the high-emissivity surface is only about 0.5 K in the laboratory, whereas the field LTM is in the range of 2-7 K; and

(b) The lab-LTM height is about 5-8 mm whereas the field LTM is in the range of 20-30 cm. The main reason for these differences is the compressed vertical scale in the laboratory setup that enhances the conduction fluxes (by a factor of 8 to 10) in relation to radiative fluxes. For the very same reason, the normalized temperature deviations obtained here (from the linear conduction profile) due to the radiative source term are much larger than those in earlier experiments, where similar experiments involved much thinner gas layers.

2.5.3 Effect of aerosols on LTM

The laboratory setup is a useful tool to study various aspects of the LTM, and to verify the hypotheses concerning its formation. It is mentioned in the introduction that a homogeneous atmosphere does not support the preferential cooling necessary for an LTM-type profile, and that the latter may only form in an atmosphere that is heterogeneous on the same scales. The field observations do not indicate a haze layer, as assumed by Zdunkowski (1966) in an earlier effort to explain the LTM phenomenon. Keeping in mind the observed insensitivity of LTM characteristics to humidity changes, the only candidate for such a heterogeneity would

therefore seem to be suspended micron-sized aerosols - those that are invisible under normal conditions. The experimental evidence for this hypothesis is obtained using our laboratory setup. An arrangement was made to remove the aerosol particles from the air in the test section by continuously sucking air out from the test section and readmitting it after having passed through an HEPA filter that removes particles with sizes greater than 0.3 μm. In addition, to capture images of the aerosol particles in the test section, a 2.5 mm thick light sheet from an Nd-Yag pulsed laser was used to illuminate a vertical plane close to the center of the test section. Images covering 60% of the height of the test section (from 2 cm to 8 cm above the bottom boundary) were captured using a Nikon D-90 digital camera.

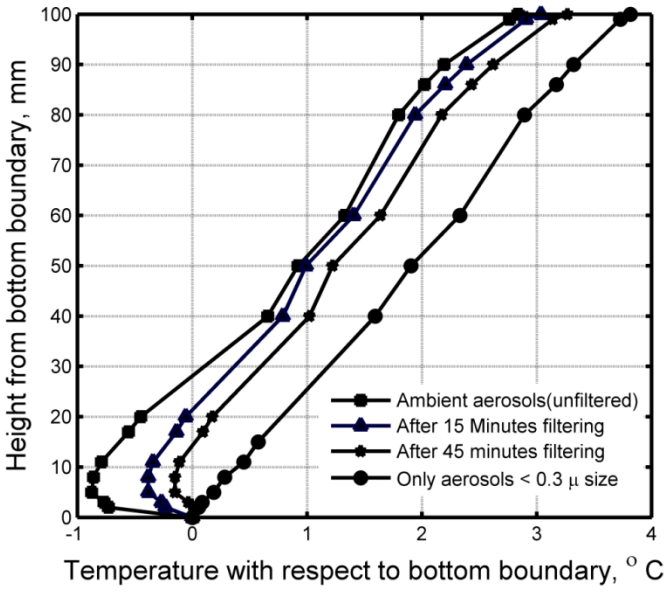

Figure 2.12 Temperature profiles with low emissivity surface ($\varepsilon_g \approx 0.05$) with ambient air (normal aerosols) and for different durations (15, 45 and over 60 minutes) of filtering using an HEPA filter. With filtering, the intensity of the LTM progressively decreases, and eventually, the elevated minimum completely disappears while the profile transitioning to a linear conduction profile. T_{Sky} is held at 280 K and T_g is at 300 K for all such cases.

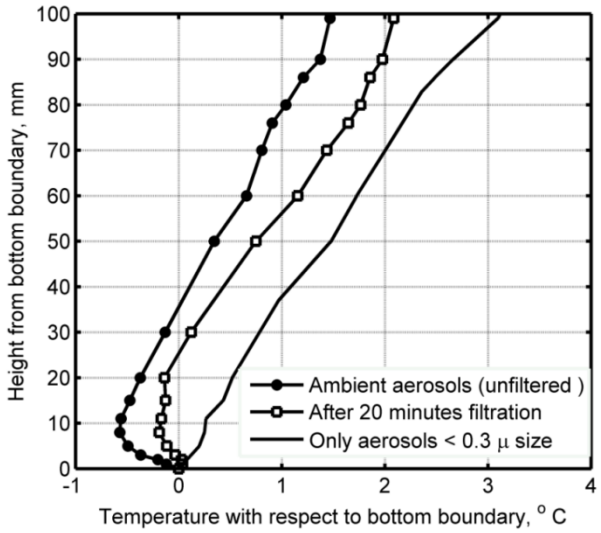

Figure 2.13 Temperature profiles with high emissivity surface ($e_g \approx 0.9$) with ambient air (normal aerosols) and for different durations (20 and over 60 minutes) of filtering using HEPA filter. With filtering, the intensity of the LTM progressively decreases and eventually, the elevated minimum completely disappears, the profile transitioning to a linear conduction profile. T_{Sky} is held at 280 K and T_g is at 300 K for all such cases.

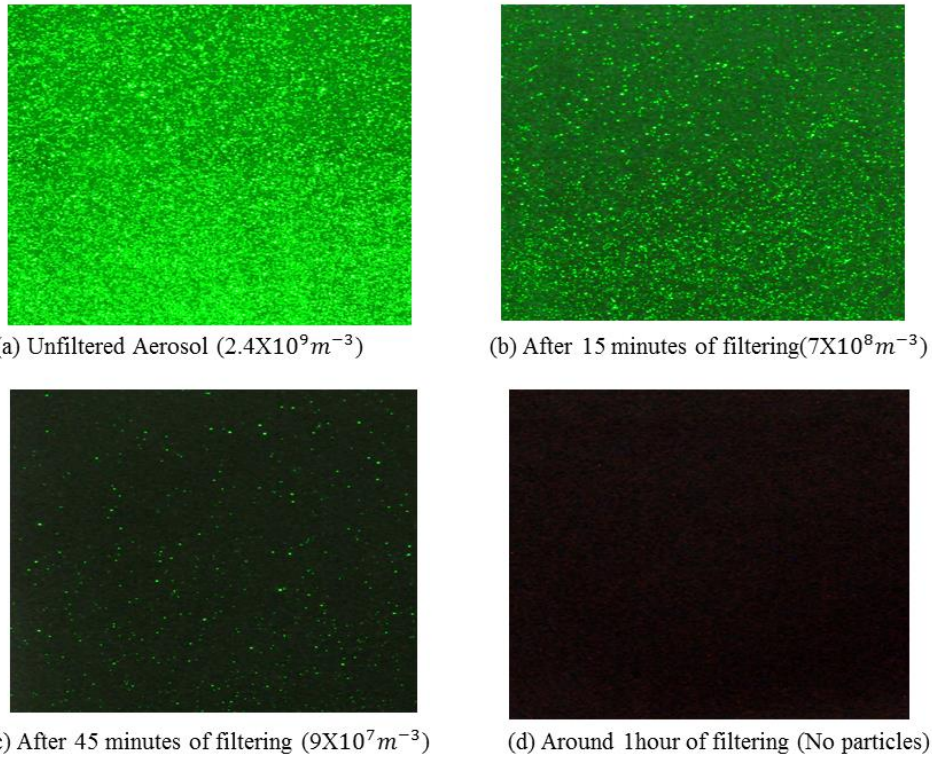

(a) Unfiltered Aerosol ($2.4X10^9 m^{-3}$)

(b) After 15 minutes of filtering($7X10^8 m^{-3}$)

(c) After 45 minutes of filtering ($9X10^7 m^{-3}$)

(d) Around 1hour of filtering (No particles)

Figure 2.14 Aerosol concentration in the laboratory setup (a) before filtering and after filtering for different durations (15, 45 and over 60 minutes) using HEPA filter.

Initially, before any filtration (with ambient aerosols), an experiment was performed to obtain an LTM profile. Next, the filtering was carried out for a fixed duration and the system was allowed to settle thereafter for about 2 hours so as to establish a new concentration profile. The temperature profile is then measured with the same T_{sky} and T_{top} as before (though the relative humidity decreased during filtration, the system relaxes and the final relative humidity after 2 hours is close to the initial value). Fig. 2.12 and Fig. 2.13 show the temperature profiles in the test section and Fig. 2.14 shows the images of aerosols captured after various durations of filtering up to a maximum of one hour. It can be seen that the particle number density and the intensity of the minimum decrease with an increase duration of filtering. With a filtering duration of 60 minutes, the temperature variation follows a linear conduction profile and there is no longer an elevated minimum.

2.5.4 Average aerosol number density in the test section

2.5.4.1 Image analysis method

Using the images of aerosols, particle number densities have been estimated. In order to calculate particle number density, the images have been first converted into binary format. The threshold value for this conversion is obtained from a Matlab code. The number of particles with respect to the threshold value (0 to 1) for an image in the test section in plotted in Fig. 2.15. In Fig. 2.15, the number of particles varies with respect to threshold, but the number of particles is approximately constant for a particular range of threshold values. This value has been taken as the number of particles. The size of particles is difficult to find with present method because of diffraction limit.

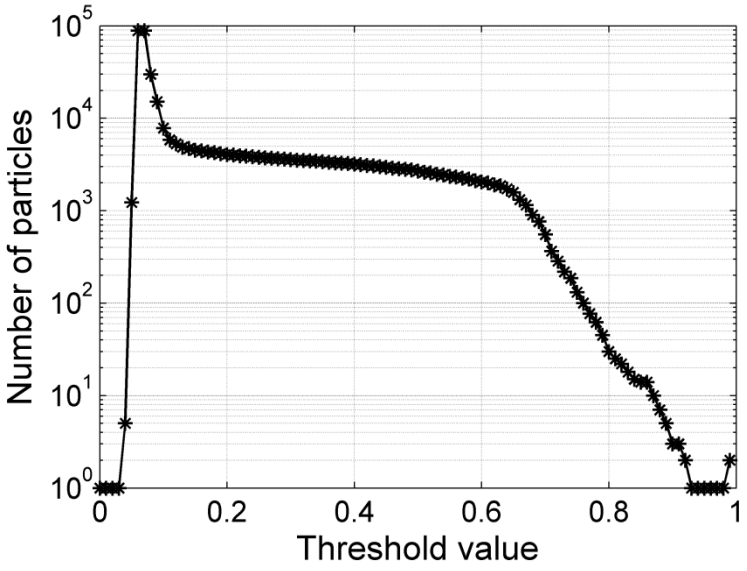

Figure 2.15 Number of particles with respect to threshold value for a typical image (6 cm X 4 cm X 0.25 cm) in the test section with 2.5 mm thick laser sheet.

A point source in the object field will spread out into an Airy function on the image plane. The diameter of the diffraction-limited point spread function, in the image plane, is given by [Adrian et. al (1991)]

$$d_s = 2.44\,(1 + \mathrm{M})\mathrm{F}\lambda \tag{2.4}$$

Where M is magnification of lens (1.01), λ is wavelength of laser (532 nm) and F is f-number of lens (9), which is ratio of focal length and lens aperture.

The diameter of point-spread function in our experiment is approximately 23 μm. The actual images taken on the camera is the convolution of diffraction-limited image with the geometric image [Adrian et. al (1991)]. Both the geometric and diffraction-limited images are approximate Gaussian functions. The resulting convolution is a Gaussian function with an effective particle diameter d_e, where

$$d_e = \sqrt{[M^2 d_p^2 + d_s^2]} \tag{2.5}$$

Here, M, d_p and d_s are magnification, diameter of particle in object plane and diameter of particle in image plane respectively, which is diffraction limited and Hence d_e > 23 μm in our case.

Typically, particles of size 0.01 μm – 10 μm are suspended in the lower atmosphere. Images have been converted into binary using the appropriate value of threshold then ‘‘Regionprops’’ Matlab command is used for calculation of number of particles. The size of the particles cannot be calculated by the present method. The sizes of all particles present in the test section are imaged approximately to the same size in the image plane due to the diffraction limit. However, after converting the image into binary, it can be seen that area of all the particles are not the same. The ratio of maximum area to minimum area in a typical image is O (100). The dimension of the image in the object plane is 6 X 4 X 0.25 cm^3 and the area is 24 cm^2. The fraction of area of particles in the image plane is the ratio of the sum of the area of particles in the image plane and total area of the image (frame).

If N is effective number of particles equivalent of 1 μm, then,

$$N = \frac{Sum\ of\ area\ of\ particles\ in\ image\ plane}{Area\ of\ 1\ \mu m\ particle\ in\ image\ plane\ X\ volume\ of\ frame\ in\ object\ plane}$$

By using the above method, the estimated average number density of particles in the test section for the case of ambient aerosols (unfiltered aerosols) is 1 x 10^{10} m^{-3}. The average number density of particles in case of after 15 minutes filtration is 3.6 x10^9 m^{-3}. The average number density of particles in case of after 45 minutes filtration is 5.2 x10^8 m^{-3}. After 1 hour of filtration, few particles of size < 0.3 μm are present in the test section. It should be noted that there are two difficulties in the present method. First, we could not measure particles less

than 0.3 μm in size and second, it is very difficult to measure number density very close (below 1 cm) to the ground where particles are more.

2.5.4.2 Metone airborne particle counter (model –A2400)

The particle size distributions were also measured by pumping the air out and passing it through a Metone airborne particle counter (model-A2400). In a typical experiment, before filtration, the particle number densities measured were as follows: 0.3 μm - 0.5 μm: 3.72×10^9 m^{-3}; 0.5 μm -1 μm: (2.60×10^8 m^{-3}); 1 μm - 5 μm: (2.77×10^7 m^{-3}); 5 μm - 10 μm: (2.18×10^7 m^{-3}); and greater than 10 μm: (1.93×10^7 m^{-3}). After filtration for more than 60 minutes, virtually no particles with sizes greater than 0.3 μm were observed. The above numbers correspond to an average over the entire test section, and in terms of surface area available for radiative interactions, the measured polydisperse mixture is approximately equivalent to a vertically averaged number density of 4.3×10^9 1μm particles/m^3 of air in the test section. Even in this method, we could not measure particles less than 0.3 μm in size as well as those very close to the ground.

For the formation of an LTM-type profile, air, being a poor emitter and absorber of radiation, has to cool faster than the ground. The observations also show that the cooling of the air layers to be intense close to the ground, decreasing rapidly with height thereafter. In the section, we argue that the faster cooling of air-layers is due to the presence of suspended aerosols acting as efficient radiators in the atmospheric window. Further, the intense near-ground cooling is argued to be due to the inhomogeneous vertical distribution of aerosols on length scales corresponding to the LTM. The first part of the evidence that hinges on the necessity of aerosols for the formation of an LTM-type profile was demonstrated in the laboratory setup using an HEPA filter (Fig. 2.12 and Fig. 2.13). Although aerosols in the

laboratory air are not visible under normal circumstances, their presence nevertheless becomes evident if a laser light-sheet is used for illumination in the dark. In Fig. 2.16, we present images of aerosols captured in the laboratory using laser sheet illumination and a Nikon-D90 digital camera. These images indicate the presence of aerosols in large numbers and also provide support for the second part of the evidence above that relies on the inhomogeneous vertical distribution of aerosols - there is a ten-fold increase in the particle number density at 1.5 cm (Fig. 2.16 a) compared to that at 10 cm height (Fig. 2.16 c).

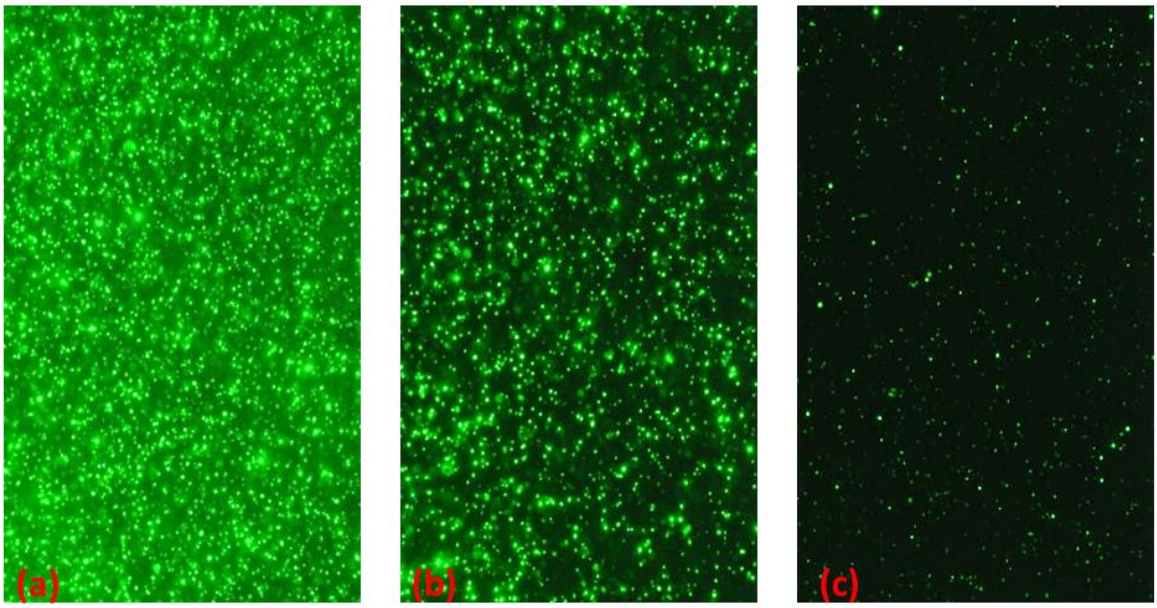

Figure 2.16 Aerosols imaged in the laboratory in a horizontal plane at different levels (a) at 1.5 cm 2.68×10^{10} particles m^{-3}, (b) at 3 cm 1.08×10^{10} particles m^{-3}, and (c) at 10 cm 2.6×10^{9} particles m^{-3}, above the ground. The image area is about 1.5 cm x 1 cm, the light-sheet is 2.5 mm thick, F/14 and illumination is by Nd-Yag pulsed laser (150 mJ $pulse^{-1}$; 7 ns pulse width).

The non-uniform vertical distribution of aerosols, as indicated in Fig. 2.16, is the primary reason for the observed hyper-cooling being close to the ground. Such a steep variation in number density is common for particulate matter suspended in a fluid [Soulsby (1997); Nielsen and Teakle (2004)] and is often modelled using a Rouse-profile. The evidence for the applicability of a Rouse-profile to the vertical variation in the aerosol number density in the NBL is presented in Fig. 2.18a [Devara and Raj (1993); Devara et al. (1997)]. Here, a Rouse-profile curve has been fitted to observations of varying aerosol number densities in a stable NBL which indicate a sharp increase in the number density close to ground. In this context, it is worth noting that the measured [Raj et al. (2008)] number of aerosols per square meter of air column (from 50 m to 200 m height) at the tropical site (Pune, India) varies from 10^{11} to 10^{13}. However, the observation starts from a height of 50 m and extends up to 4 km; which is typical of height ranges reported in the literature obtained using lidar. Particle number densities have been estimated in the test section Using the laser and camera. There are four points in the test section, where images have been taken. The minimum height from bottom boundary where images have been taken is 8 mm. According to the observation, estimated number density in the test section as a function of height is plotted in Fig. 2.17.

To summarize, the evidence presented in Fig. 2.16 and Fig. 2.17 suggests a sharp increase in the particle number density close to the ground, which in turn must lead to an intense cooling of air right above the ground and the formation of an LTM-type profile.

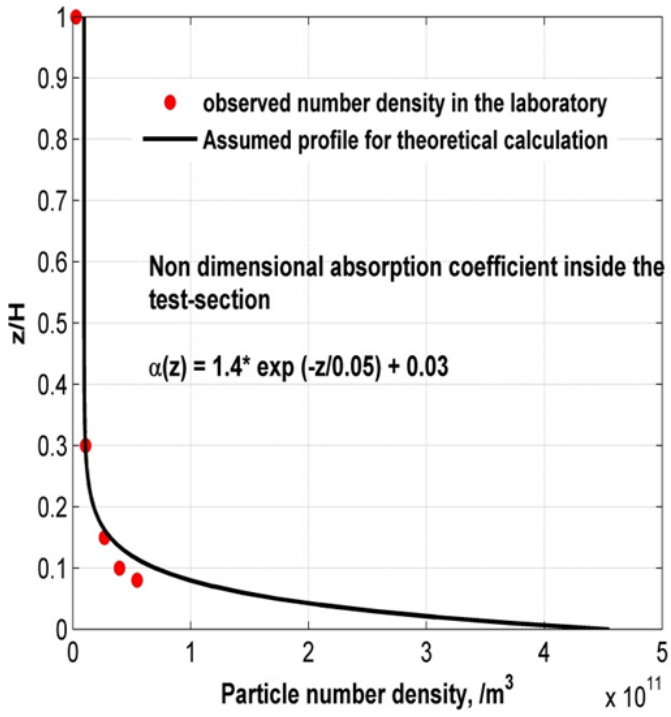

Figure 2.17. Vertical number density, in the laboratory test section plotted with respect to normalized length scale.

2.5.4.3 Aerosol number density using integral heat balance

Knowledge of the aerosol particle size distributions and the vertical variation of the number density for each size may, in principle, be used to estimate the radiative cooling rates and the response times for the aerosol-laden near-surface air layers. Since the details of the vertical distribution of the aerosol number density are not known, we use an integral heat balance to estimate the total aerosol number and the response times of the air layers. To this end, we consider the aerosol-laden air in the test section as the control volume (Fig. 2.18).

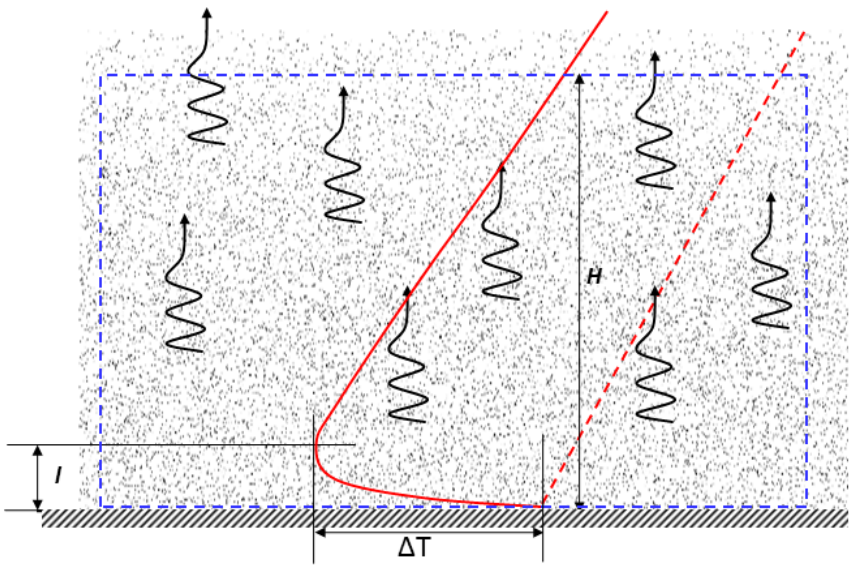

Figure 2.18 Schematic diagram indicating laboratory setup of height *H* with aerosol laden air layer having net-radiative emission. The blue broken line indicates the control-volume; the red solid and dashed lines indicate the observed temperature profiles with and without aerosols respectively in the experiments. ΔT_{min} is the intensity and *l* is the height of the observed LTM in the laboratory setup.

When the system is at steady state, the net heat gained by conduction at the top (q_t) and bottom (q_b) boundaries has to be radiated out by the aerosols distributed within the control volume. If the associated radiant flux is Q_R W/m^2 of the test section, then

$$q_b + q_t = K_{air}\left(\left.\frac{dT}{dz}\right|_b + \left.\frac{dT}{dz}\right|_t\right)$$
$$= 0.02(130+20) = 3\,W/m^2 = -Q_R \qquad (2.6)$$

Where homogeneity in the horizontal directions has been assumed and the temperature gradients at the top and bottom are readily obtained from the laboratory LTM type profile.

If the total projected area of the suspended aerosols (summed over all sizes and integrated over the test section height) per m^2 of the test section, is A,

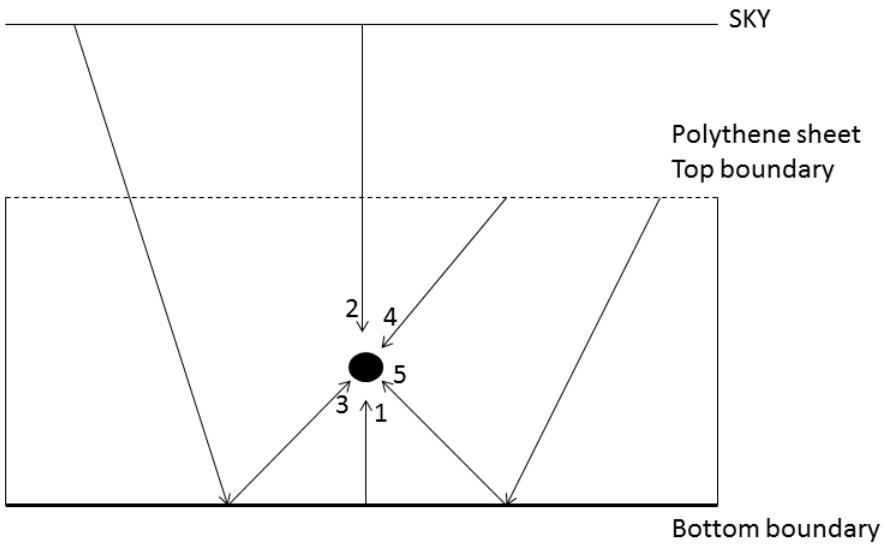

Figure 2.19 Schematic of radiation flux on aerosols in the test section.

1. Radiation flux from ground = $\varepsilon_g \boldsymbol{\sigma T_g^4} \varepsilon_p$

2. Radiation flux from Sky = $\varepsilon_{sky} \boldsymbol{\sigma T_{sky}^4} (\mathbf{1} - \varepsilon_t) \varepsilon_p$

3. Radiation flux reflected from ground = $\varepsilon_{sky} \boldsymbol{\sigma T_{sky}^4} (\mathbf{1} - \varepsilon_t)(\mathbf{1} - \varepsilon_g) \varepsilon_p$

4. Radiation flux from top boundary = $\varepsilon_t \boldsymbol{\sigma T_t^4} \varepsilon_p$

5. Radiation flux reflected from ground = $\varepsilon_t \boldsymbol{\sigma T_t^4} (\mathbf{1} - \varepsilon_g) \varepsilon_p$

Heat flux radiated by aerosols in both direction (upward and downward) = $2\varepsilon_p \boldsymbol{\sigma T_p^4} \varepsilon_p$

Then one may write the following energy balance

Net radiation flux:

$$Q_R = -A[\varepsilon_g \sigma T_g^4 \varepsilon_p + \varepsilon_{sky} \sigma T_{sky}^4 (1-\varepsilon_t)\varepsilon_p + \varepsilon_{sky} \sigma T_{sky}^4 (1-\varepsilon_t)\varepsilon_p + \varepsilon_t \sigma T_t^4 \varepsilon_p + \varepsilon_t \sigma T_t^4 (1-\varepsilon_g)\varepsilon_p 2\varepsilon_p \sigma T_p^4 \varepsilon_p].$$

$$Q_R = -A\sigma\varepsilon_p [\varepsilon_g T_{g+}^4 \varepsilon_{Sky} T_{Sky}^4 (1-\varepsilon_t)(2-\varepsilon_g) + (2-\varepsilon_g)\varepsilon_t T_t^4 - 2T_p^4]$$

$$A = \frac{-Q_R}{\sigma\varepsilon_p[\varepsilon_g T_{g+}^4 \varepsilon_{Sky} T_{Sky}^4 (1-\varepsilon_t)(2-\varepsilon_g) + (2-\varepsilon_g)\varepsilon_t T_t^4 - 2T_p^4]} \quad \text{..... (2.7)}$$

in the dilute limit (when radiative interactions either absorbing or scattering, among aerosols is negligible). In (3), T_g is the ground temperature, T_{sky} is the sky temperature, T_t is the top boundary temperature, ε_g is the ground (bottom plate) emissivity, ε_t is the top boundary emissivity and ε_P is an area-averaged aerosol emissivity. Using values that correspond to the laboratory experiments viz. $T_g = T_t = 300$ K, $T_{sky} = 278$ K, $\varepsilon_g = \varepsilon_P = 0.9$, and $\varepsilon_t = 0.2$ one obtains $A = 0.0258$ m^2/m^2

From this value of A and by knowing the height of the test section, one may calculate the equivalent number density of 1μm particles required for sustaining a laboratory LTM-type profile, and this works out to be about 2.8×10^{11} m^{-3}. The average aerosol concentration in the laboratory set up estimated by; (a) Image-Analysis method is 10^{10} m^{-3} (b) Metone airborne particle counter is 4.3×10^9 m^{-3} and (c) Integral heat balance is 2.8×10^{11} m^{-3}. The average aerosol concentration estimated by heat balance is about 20 times higher and about 50 times higher than the vertically averaged concentration as measured by Image-Analysis method and Metone airborne particle counter respectively. However, it has to be noted that the particle counter (Metone, model-A2400) cannot detect particles below 0.3μm and that its detection efficiency between 0.3-0.5μm is only 50%. There is a further fluid mechanical bias that is expected to

lead to a systematic under-sampling of aerosols close to the bottom plate (the region of highest concentration) due to the relative weak induced flow in this region. These factors may account for the particle number density being underestimated by the particle counter. Similarly, the Image-Analysis method, cannot detect less than 0.3 μm. We cannot measured very close (less than 1 cm) to the bottom boundary. It should also be noted that the aerosol number density estimated at 1.5 cm from the bottom boundary is about 10 times greater than at 10 cm from the bottom boundary as shown in Fig. 2.16. Hence we can say that the theoretical estimate is in reasonable agreement with experimental observation.

2.5.5 Pre-monsoon and monsoon aerosols

Experiments have been done in two seasons, before and during the monsoon. Keeping the bottom boundary similar, and with low emissivity (0.05), the air quality in the test section is varied. In the first case, the air in the test section is drawn from the field during the pre-monsoon season (March-April, 2011). In this case, the aerosol concentration is expected to be high due to the prevailing dry conditions. In Fig. 2.20a, vertical temperature profiles have been plotted and in this case, the intensity of the minima is 1.22 ± 0.03 K and height of the minima is 26 ± 1 mm. The experimental results agree well with the theoretical calculations for an assumed exponential distribution of aerosol particles and the resulting optical thickness distribution is $\hat{\alpha}(z) = 1.6 \exp(-z/0.1)+0.02$. Details of the theoretical calculations will also be discussed in section 2.6. In the second case, the air in the test section is taken from the field during the monsoon season (July-August 2011). In this case, the aerosol concentration is expected to be low. In Fig. 2.20b, the intensity of the minima is 0.74 ± 0.03 K and height of the minima is 20 ± 1 mm. The experimental results agree well with the

theoretical calculations for an assumed exponential distribution of aerosol particles and the resulting optical thickness distribution is $\hat{\alpha}(z)$ =0.5 exp(-z/0.1)+0.02. Radiation flux divergence and temperature gradient near the bottom boundary is 0.85 K/s and 290 K/m respectively in the case of pre-monsoon air; while they are 0.45 K/s and 145 K/m respectively in case of monsoon air.

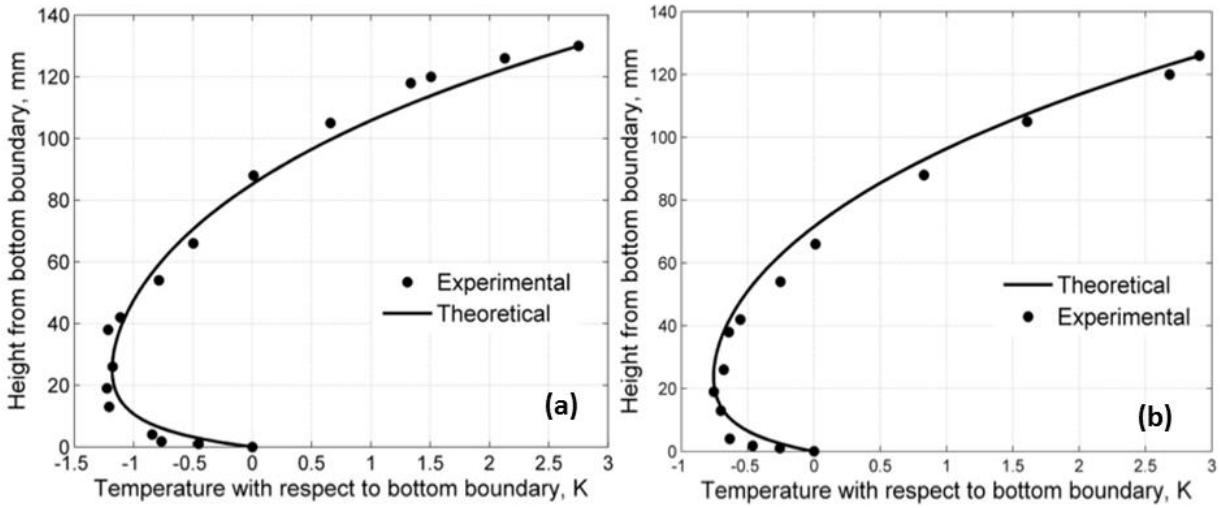

[3]Figure 2.20 (a) Vertical temperature profile in test section for reflective ($\varepsilon_{g\approx}$ 0.05) bottom boundary during pre-monsoon. T_{sky} is held 280 K, while T_g is at 300 K. solid marker correspond to experimental observation. Solid curve represent theoretical estimation, where optical thickness is α(z) =1.6 exp(-z/0.1)+0.02. (b) Vertical temperature profile in test section for reflective (ε_g 0.05) bottom boundary during monsoon. T_{sky} is held 280 K, while T_g is at 300 K. solid marker correspond to experimental observation. Solid curve represent theoretical estimation, where optical thickness is α(z) =0.5 exp(-z/0.1)+0.02.

[3] SINGH, D. K., PONNULAKSHMI, V. K., MUKUND, V., SUBRAMANIAN, G. ,AND SREENIVAS, K. R.,(2013), Radiation forcing by the atmospheric aerosols in the nocturnal boundary layer. AIP Conf. Proc. 1531, 596 (2013); http://dx.doi.org/10.1063/1.4804840.

The estimated average number density calculated using the imaging method is 3 x 10^9 m^{-3} and 1.3 X10^9 m^{-3} in case of pre-monsoon and monsoon respectively and is shown in Fig. 2.21. In the case of pre-monsoon, the intensity of minima and cooling rate of LTM-type profile is 1.5 times greater than in case of monsoon.

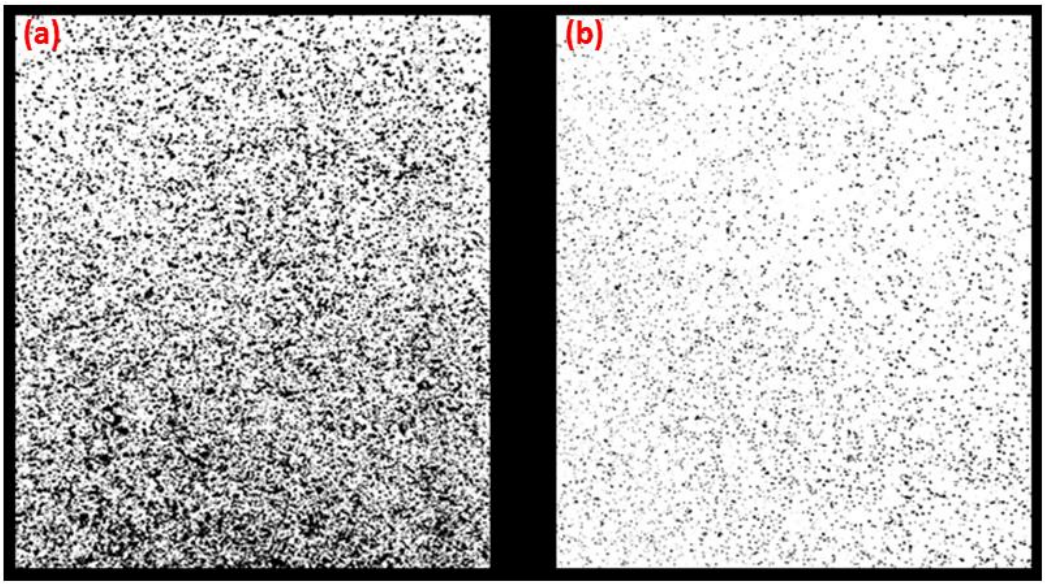

Figure 2.21 Aerosols image in the test section. (a) Pre-monsoon. (b) During monsoon.

2.5.6 Laboratory cloud event for various bottom boundaries

In order to study the response of aerosols, a 'blocking experiment' is simulated where an opaque sheet is inserted to prevent any interaction between the aerosols and the cold sink. This resembles a passing cloud-cover in the atmospheric context. The 'cloud event' is incorporating a sudden change in the radiative sink temperature. In addition to highlighting the distinction between LTM-type and conduction-type equilibria, the laboratory setup may also be used to characterize the transient response resulting from the aerosol-induced

radiative cooling, and the resulting transition of the system from one equilibrium to the other. We conducted four set of experiments in which, after obtaining a steady LTM-type profile, an opaque plate was inserted between the circulation chamber and the outer aluminum enclosure. With the opaque plate in place, the air layers in the test section cannot radiatively cool to the model sky, and the system accordingly transitions to a new (non-LTM) radiative-conductive equilibrium; the situation being similar to the response to a passing cloud cover in the field experiments [Oke (1970)].

For the first case with bottom boundary having low emissivity and high thermal inertia, the temperature traces in the test section are shown in Fig. 2.22. Temperature at various heights in the test section is plotted with respect to time. Before t=2.75 min in Fig. 2.22 temperature of air layers, top and bottom boundary of the test section are in conductive equilibrium state. At t=2.75 min, the cooling source (sky) is turned on and after ~ 30 min, the new steady state is achieved. At t=31.5 min, an opaque sheet was inserted between 2nd chamber and the sky and at t=39 min, the opaque sheet was removed. For the second case of bottom boundary with high emissivity and high thermal inertia, the temperature traces in the test section are shown in Fig. 2.23. The temperature at various heights in the test section is plotted with respect to time. Before t=8 min, temperature of air layers in the test section including top and bottom boundary are in conductive equilibrium state. At t=8 min, the cooling source (Sky) was turned on. At t=55 min, opaque sheet was inserted between 2nd chamber and Sky (blocking), and at t=37.5 min, opaque sheet was removed (unblocking). For the third case of bottom boundary with high emissivity and low thermal inertia, the temperature traces in the test section are shown in Fig. 2.24. Temperature at various heights in the test section is

plotted with respect to time. Before t=79 min temperature of air layers in the test section including top and bottom boundary were in conductive equilibrium state. At t=79 min, the cooling source (Sky) was turned on. At t =110 min, an opaque sheet was inserted between the 2^{nd} chamber and the Sky and at t=114 min, the opaque sheet was removed. For the fourth case of bottom boundary with low emissivity and low thermal inertia, the temperature traces in the test section are shown in Fig. 2.25. Temperatures at various heights in the test section are plotted with time. Before t=3 min, temperature of air layers in the test section including top and bottom boundary were in conductive equilibrium state. At t=3 min, the cooling source (Sky) was turned on. At t=26 min, opaque sheet is inserted between 2^{nd} chamber and Sky and at t=32 min, the opaque sheet was removed.

The time-temperature traces and the vertical temperature profiles before, during, and after blocking are presented in Fig . 2.26 and Fig. 2.27. Immediately after blocking, the temperatures at all locations start increasing, and the initial LTM is soon destroyed. The temperature profile at 3.2 minutes (Fig. 2.26) clearly indicated the absence of an LTM. At 3.2 mins, the plate was removed and the LTM is re-established (Fig. 2.27, profile at 7.5 mins).

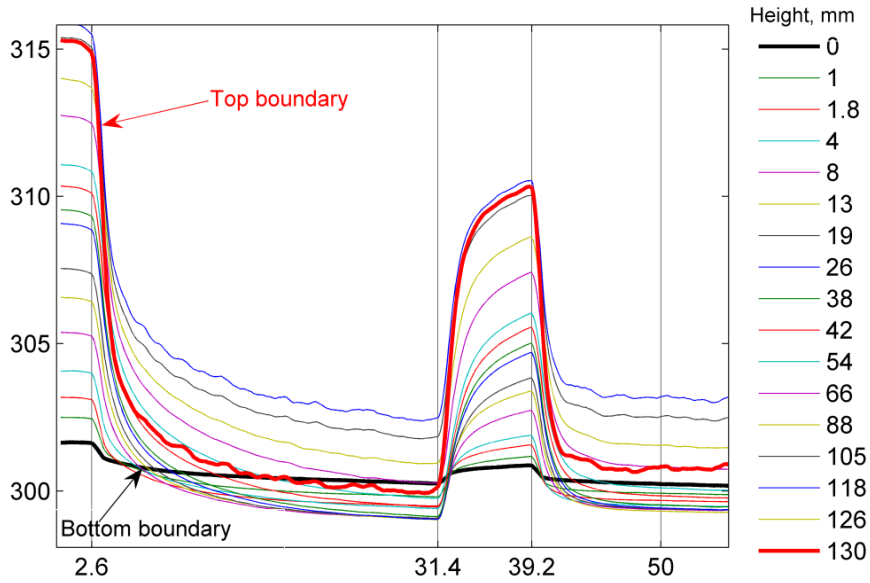

Figure 2.22 Temperature of air layers in the test section, with respect to time, at various vertical position in the test section, and for bottom boundary with low emissivity and high thermal inertia. Red and black lines represent the temperature of top and bottom boundary respectively.

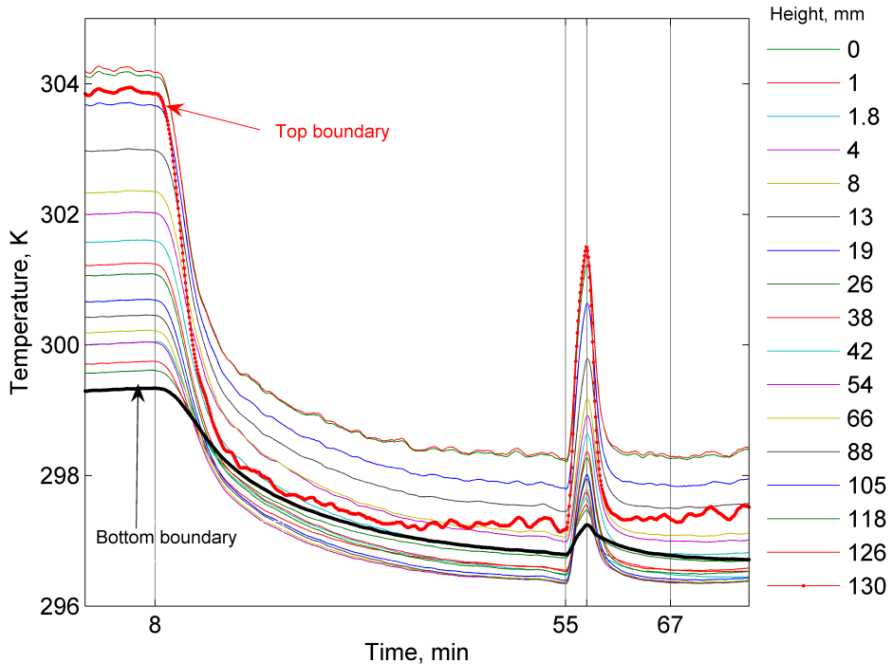

Figure 2.23 Temperature of air layers in the test section, with respect to time, at various vertical positions in the test section, and for bottom boundary with high emissivity and high thermal inertia. Red and black lines represent the temperature of top and bottom boundary respectively.

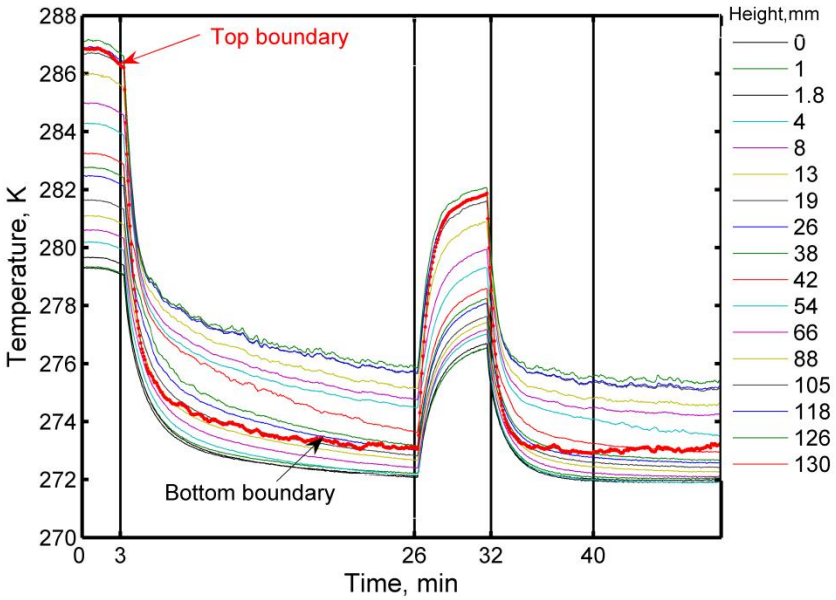

Figure 2.24 Temperature of air layers in the test section, with respect to time, at various vertical positions in the test section, and for bottom boundary with high emissivity and low thermal inertia. Red and black lines represent the temperature of top and bottom boundary respectively.

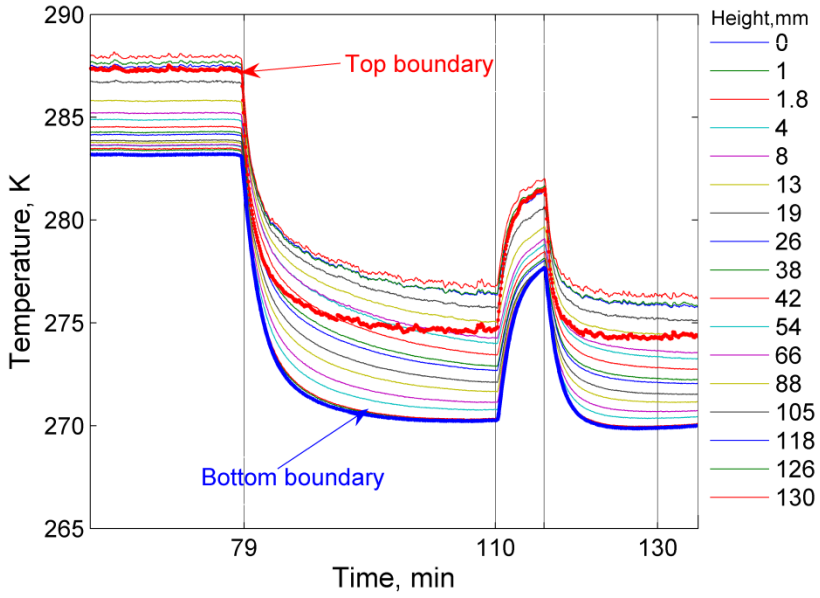

Figure 2.25 Temperature of air layers in the test section, with respect to time, at various vertical positions in the test section, and for bottom boundary with low emissivity and low thermal inertia. Red and blue lines represent the temperature of top and bottom boundary respectively

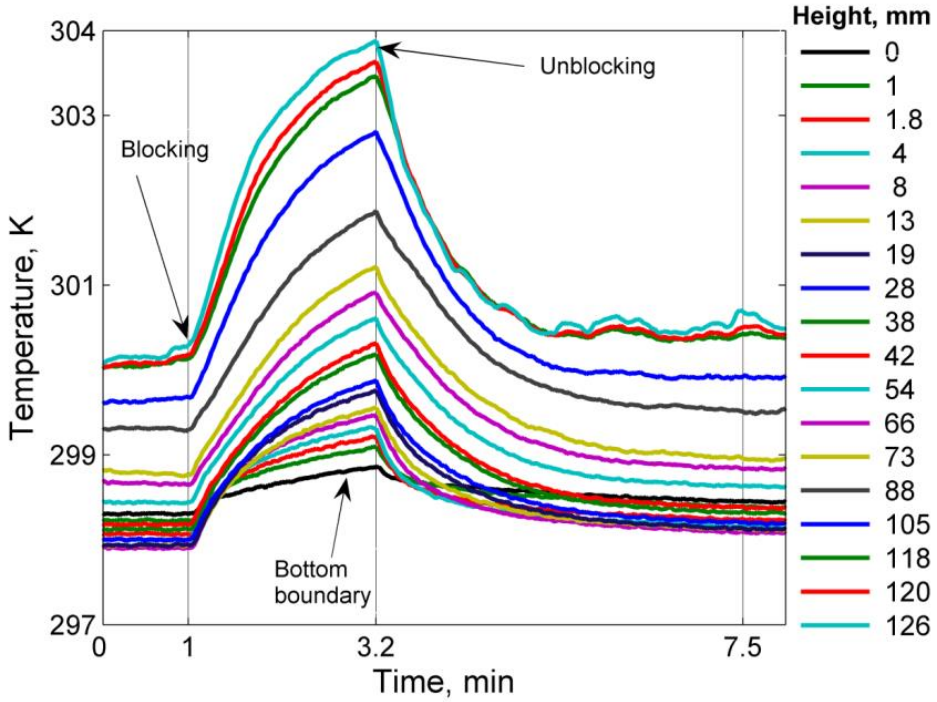

Figure 2.26 Experiments to estimate time constant of the system - temperature traces in the test section plotted with respect to the bottom plate at various vertical locations. Blocking (at 1 min) and unblocking (at 3.2 min) times have been marked.

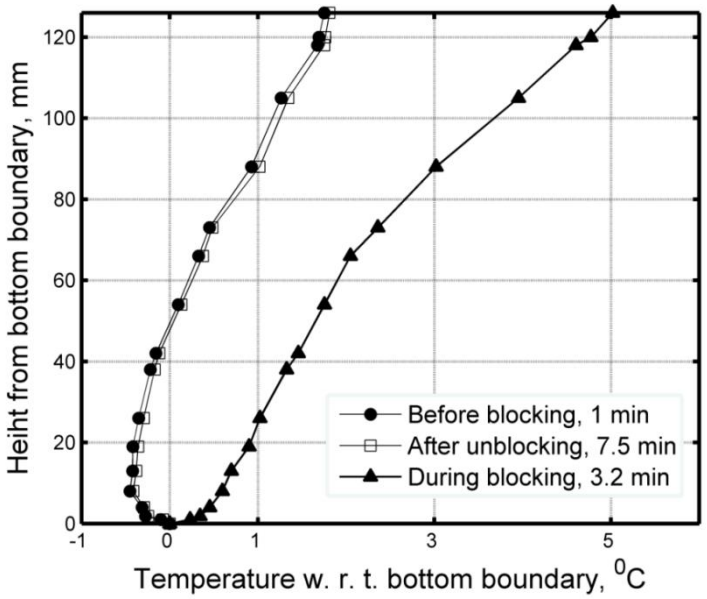

Figure 2.27 Vertical temperature profiles before blocking, during blocking, and after unblocking the radiation interaction with the model-sky.

By normalizing the temperature at each vertical location, so the normalized temperature, θ (z), falls between 0 and 1, and by taking a vertical average (to obtain $\bar{\theta}$), one may obtain an averaged time scale for the response of the system. Fig. 2.28 shows $\bar{\theta}$ plotted against time with zero on the time axis corresponding to the instant at which the sky is blocked; at t = 2.13 minutes, the block was removed. The averaged response, during both the blocking and unblocking phases, may be fitted reasonably well with an exponential, and the resulting characteristic time scale (in both cases) is about 50 s.

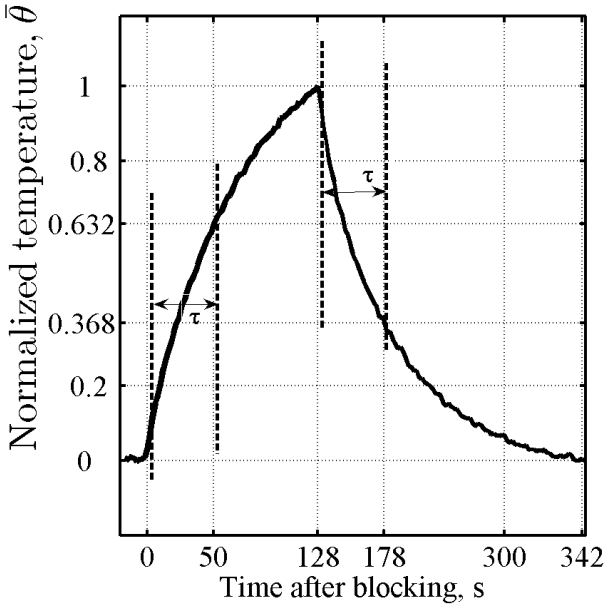

Figure 2.28 Averaged, normalized temperature varying with time; τ is the time constant of the the system for both blocking and unblocking. Blocking is done at time, t=0 s and blocking is removed (unblocked) at time, t=128 s.

By knowing the number density and size of the aerosol, we can estimate the response time for the aerosol laden surface layer as follows: net heating/cooling rate for the aerosol laden air layer is equals to the Radiation from (sky + Ground) - particle emission.

If the instantaneous temperature of the particle is T_P having a diameter ϕ_P, exchanging heat by radiation with sky at temperature T_{sky} and the ground at T_g and with the emissivity of the particle is ε_P and the ground is ε_g, then

$$mC_p \frac{dT_p}{dt} = 5.67x10^{-8}\ \varepsilon_p\ [(2-\varepsilon_g)T_{sky}^4 + \varepsilon_g T_g^4 - 2T_P]\ \pi D_P^2$$

Where m is the total mass of air and particle mixture

$$mC_P = m_a C_{Pa} + m_p C_{Pp} \quad \text{if } \lambda \text{ is the inter-particle spacing } \lambda = 1x10^{-2}/N^{1/3}$$

Where, N is the particle number density expressed as N particle per cc.

$$\therefore\ mC_P = \rho_p C_{Pp} \frac{\pi}{6} D_p^3 \left[1 + \frac{\rho_a C_{Pa}}{\rho_p C_{Pp}} \left(\frac{\lambda}{D_p}\right)^3\right] = m_p C_p f \quad \text{where} \quad f = \left[1 + \frac{\rho_a C_{Pa}}{\rho_p C_{Pp}} \left(\frac{\lambda}{D_p}\right)^3\right]$$

$$\therefore \rho_p C_{Pp} f \frac{\pi}{6} D_p^3 \frac{dT_p}{dt} = 5.67x10^{-8}\ \varepsilon_p\ [(2-\varepsilon_g)T_{sky}^4 + \varepsilon_g T_g^4 - 2T_P]\ \pi D_P^2$$

$$\frac{dT_P}{dt} = \frac{12\sigma\varepsilon_P}{D_p \rho_p C_{Pp} f}(a^4 - T_p^4) \quad \text{where } a^4 = \frac{[(2-\varepsilon_g)T_s^4 + \varepsilon_g T_g^4]}{2}$$

If $T_m = 0.5(T_{pf} + T_{pi}) = 0.5(a + T_{pi})$ and $\Delta T = (a - T_p)$;

$$\therefore dT_p = -d\Delta T \quad \text{and } d(a^4 - T_p^4) = 4T_m^3 = 0.5(a + T_{pi})^3 \Delta T$$

$$\frac{d\Delta T}{dt} = -\frac{6\sigma\varepsilon_P}{D_p \rho_p C_{Pp} f}(a + T_{pi})^3 \Delta T = -K\Delta T$$

$$\therefore\ \Delta T = e^{-Kt} \quad \text{weher } K = \frac{6\sigma\varepsilon_P}{D_p \rho_p C_{Pp} f}(a + T_{pi})^3$$

$\tau_{rad} = \frac{n(u)V\rho^{aero}C_p^{aero} + \rho^{air}C_p^{air}}{8f_w\sigma T_{rad}^3 A\varepsilon_p n(u)}$ ----- (2.8) where $T_{rad}^4 = \frac{[(2-\varepsilon_g)T_{sky}^4 + \varepsilon_g T_g^4]}{2}$, n (u) is the number density, V is the volume, A is area, ρ^{aero} and ρ^{air} is the density of the aerosol

and air respectively, C_p^{aero} and C_p^{air} are the specific heat capacity of aerosol and air respectively. ε_p and ε_g are the emissivity of particle and ground respectively.

2.5.7 Laboratory cloud event with controlled boundary conditions

In addition to highlighting the distinction between LTM-type and conduction-type equilibria, the laboratory setup could also be used to characterize the transient response resulting from the aerosol-induced radiative cooling, and the resulting transition of the system, from one equilibrium to the other. We conducted a set of experiments in which after obtaining a steady LTM-type profile, an opaque plate was inserted between the circulation chamber and the outer aluminum enclosure. With the opaque plate in place, the air layers in the test section cannot radiatively cool to the model sky and the system accordingly transitions to a new (non-LTM) radiative-conductive equilibrium. The temperature of the opaque sheet lying on the second chamber starts increasing during blocking and after ~ 15 min, it attains a constant value (315 K) along with the air layers in the test section. The opaque sheet then behaves as the hotter radiation boundary and air layers in the test section including boundaries can radiatively interact with the opaque sheet. We have estimated radiation time constant numerically and experimentally in the previous section. In the previous blocking and unblocking experiments, the temperature of the boundaries was changing during the blocking. During the blocking, first LTM disappeared and then started heating with respect to conduction linear profile due to hotter radiation boundary (opaque sheet). In this section, the aim of the experiment is to control the temperature of the boundaries as well as the temperature of the opaque plate during blocking and to estimate the only radiation effect, and neutralize the boundaries effect. For this, experiments have been conducted in the following

ways during blocking: a) Cold air has been circulated in the circulation chamber. b) The opaque plate has been placed away from the second chamber and near the model sky. c) Al foil (low emissivity) on the bottom of the opaque sheet to reduce emittance. After completing all the above procedures during the blocking experiments, the temperature of the boundaries of the test section is approximately controlled. With controlled boundary, the top boundary's temperature increased by 0.4 K, and by 6 K in the case of without controlled boundary. During the blocking, the temperature of the opaque sheet was also controlled and it was 295 K, 310 K in case of without controlling. In the previous case, the emissivity of the opaque sheet was 0.9, in the present case it is 0.05. The time evolution of the temperature traces at various heights is shown in Fig. 2.29a. These are raw temperature traces, without the window-averaging. The vertical temperature profiles before, during, and after the blocking are shown in Fig. 2.29b. Immediately after blocking, the temperatures at all locations start increasing, and the initial LTM is soon destroyed. The temperature profile at 5.25 min (Fig. 2.29b) clearly indicates the absence of an LTM. At 8 min, the plate was removed and the LTM was re-established (Fig. 2.29b, profile at 14 min). By normalizing the temperature at each vertical location, so the normalized temperature, $\theta(z)$, falls between 0 and 1, and by taking a vertical average (to obtain T), one may obtain an averaged time scale for the response of the system. Fig. 2.30 shows normalized temperature plotted against time with zero on the time-axis corresponding to the instant at which the sky is blocked; at $t = 2.67$ min, the block was removed. The averaged response, during both the blocking and unblocking phases, may be fitted reasonably well with an exponential, and the resulting characteristic time scale (in both cases) is about 25 s.

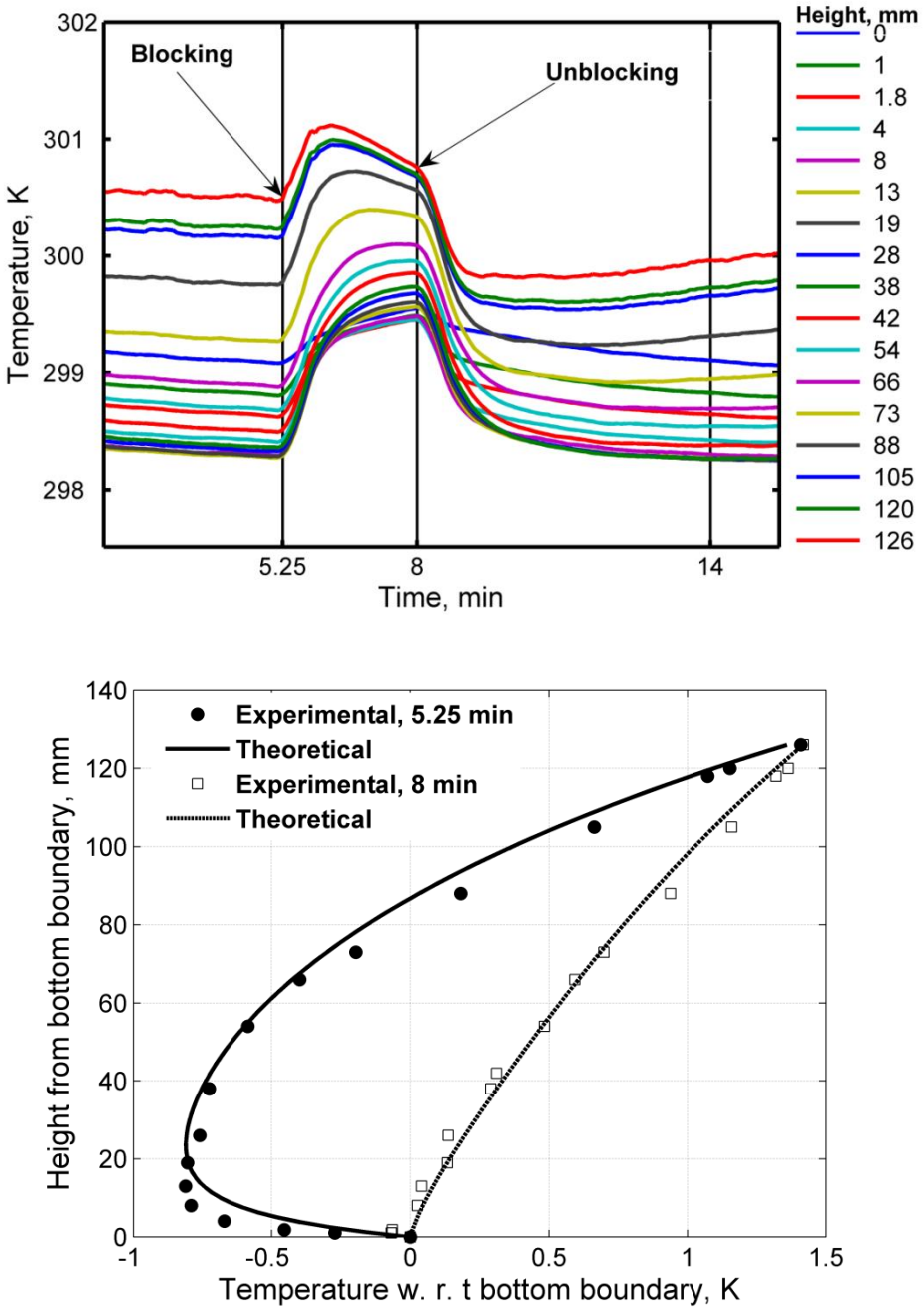

Figure 2.29 Experiments to estimate time constant of the system: (a) temperature traces in the test section is plotted at various vertical locations, blocking (at 5.25 min) and unblocking (at 8 min) times have been marked and (b) vertical temperature profiles before blocking, during blocking, and after the unblocking the radiation interaction of air layers in the test section with the model-sky. Theoretical analysis carried out by Ponnulakshmi (2013).

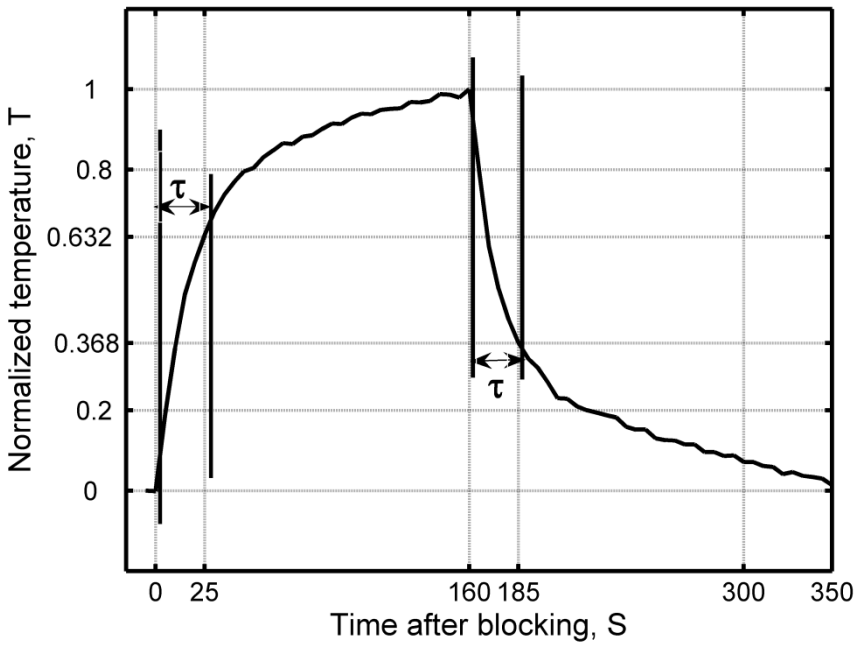

Figure 2.30 Averaged, normalized temperature varying with time; τ is the time constant of the system for both blocking and unblocking. Blocking is done at time, t=0 s and unblocking at time, t=160 s.

One may now characterize the above transient response based on a simple analysis that again uses an integral heat balance with the air in the control volume being initially isothermal and at the ground temperature. If m is the mass of the aerosol-laden air per square meter of the test section, C_P its specific heat, and q_C is the instantaneous conductive flux into the control volume, one may write the transient energy balance equation as follows

$$mc_P \frac{d\Delta T}{dt} = Q_R - q_C(t) \quad \text{Where,} \quad q_C(t) = \left(Q_R \frac{\Delta T}{\Delta T_{min}} \right)$$

$$mc_P \frac{d\Delta T}{dt} = Q_R \left(1 - \frac{\Delta T}{\Delta T_{min}} \right) \quad \therefore \quad \frac{d\Delta T}{\left(1 - \frac{\Delta T}{\Delta T_{min}} \right)} = \frac{Q_R}{mc_P} dt$$

$$\Delta T = \Delta T_{min} \left(1 - e^{-t\left(\frac{Q_R}{\Delta T_{min} mc_P} \right)} \right) = \Delta T_{min} \left(1 - e^{-\frac{t}{\tau_{rad}}} \right)$$

$$\Delta T = \Delta T_{min} \, (1 - e^{-t/\tau_{rad}}) \qquad (2.9)$$

Where the simplest possible form (linear in ΔT) is assumed for the conductive flux term that is zero at the initial instant (consistent with isothermality) and balances Q_R in the eventual equilibrium state. The predicted time scale for cooling (T_{rad}) is -($mC_P\Delta T_{min}$)/ Q_R. Again, using the typical values corresponding to the experiments - m ~ 0.135 kg, C_P ~ 1000J/kg-K, ΔT_{min} ~ 0.76 K and Q_R~ 4.13 W/m^2, one finds τ_{rad} ~ 24 s, which is close to that obtained from the experiments above.

2.5.8 Ramdas-Zndunkowski factor (R_{zf}):

Data has been taken from field observations [Mukund (2008)] and our laboratory experiments for various conditions of bottom surfaces. The field observations [Mukund (2008)] clearly show that the nature of the vertical temperature profile depends crucially on surface characteristics. Observations of LTM-type profiles on bare concrete are in contrast to the occurrence of an inversion layer on thermofoam. This suggests that the nature of the

observed temperature profile depends on the magnitude of the surface cooling rate in relation to those of the overlying air layers - if the surface cools faster than the overlying air-layers, one obtains an inversion profile; an LTM-type profile results in the opposite scenario. The cooling rates under consideration are, in turn, dependent on the thermophysical properties of the underlying surfaces and the near-surface aerosol concentrations (The laboratory cloud event experiments in section 2.5.7 show the time scale characterizing the cooling of the air layers, for typical aerosol concentrations to be about 25 s).

A non-dimensional number, the Ramdas-Zdunkowski factor (R_{zf}) is defined as the ratio of the cooling rates of the near-surface air layers to that of ground. An O (1) value of R_{zf} should serve as a threshold, helping to discriminate between the inversion and LTM regimes in the lowest meter of the NBL. If one starts with the air layers and the ground, initially at a uniform temperature (over the relevant length scales), established by an episode of turbulent mixing for instance, then the air temperature at a later time may be written as $T = T_{rad} + \Delta T_i$. Here, ΔT_i is a measure of the driving force, i.e., the temperature difference between the initial isothermal temperature and radiative equilibrium temperature over length scales relevant to the LTM, between the near-surface air-layers (T) and the (hypothetical) radiative equilibrium state (T_{rad}). Assuming the primary mechanism of cooling under calm conditions to be of a radiative character, the cooling rate of the near-surface air layers may be written in the form $\Delta T_i/\tau_{rad}$, τ_{rad} being the intrinsic relaxation time scale obtained in section 2.5.7; see Eq.(2.6). Accounting for the thermal penetration depth of $O(\sqrt{k_s \tau_{rad}})$ within the surface, the surface cooling rate is given by $F_s/[\rho_s C_{ps} \sqrt{k_s \tau_{rad}}]$, where F_s is the net upward radiative flux from the surface; ρ_s,C_{Ps} and κ_s are, respectively, the density, specific heat capacity and thermal

diffusivity of the surface (Fig. 2.31). The ratio between these two cooling rates leads to the required expression for the Ramdas-Zdunkowski factor (R_{zf}) as

$$R_{zf} = Cooling\ rate\ of\ air / Cooling\ rate\ of\ ground$$

$$R_{zf} = \frac{\Delta T_i}{F_s} \rho_s C_{ps} \sqrt{\frac{k_s}{\tau_{rad}}} \qquad (2.10)$$

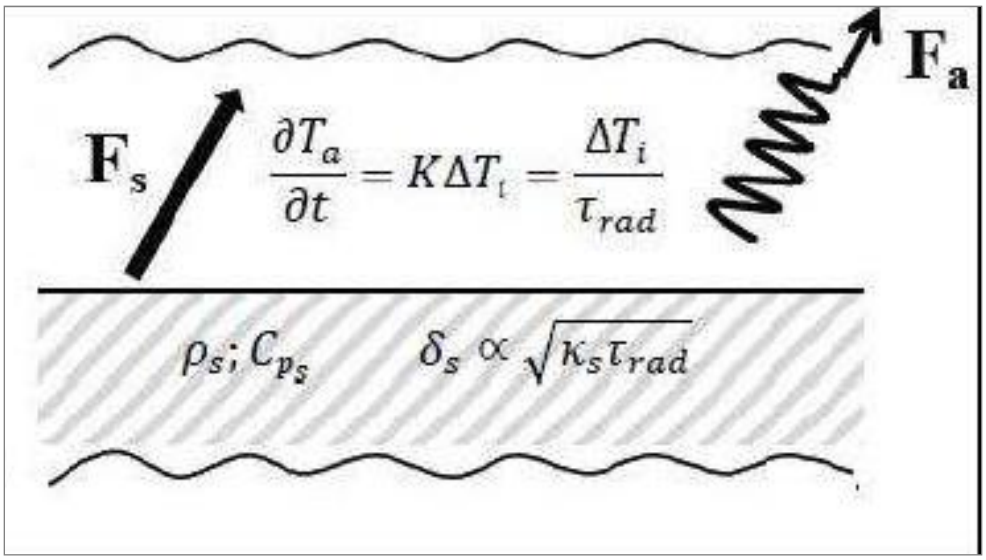

Figure 2.31. The cooling processes for the air layer and the underlying surface are shown in the diagram. The rate of change in the air layer is from (provided appropriate equation) the sub-surface layer of thickness $\delta_S = \sqrt{\kappa_S \tau_{\text{rad}}}$ cools due to upward radiative flux F_S from the surface. R_{zf}, the *Ramdas-Zdunkowski factor* $(R_{zf} = F_a / F_S)$ is the non-dimensional ratio between cooling rates of air and the underlying surface.

Calculation of R_{zf} for field observations

Based on field experiments**,** we take ΔT_i = 10K and τ_{rad} = 25 s. Now, F_s for the high-emissivity surface is about 100 -110 Wm^{-2}, while that for the low-emissivity surface is about 8 −10 Wm^{-2}. Further, the thermal heat capacity ($\rho_s C_{Ps}$) for concrete is about 2×10^6 J $m^{-3}K^{-1}$ and that for thermofoam is about 5×10^4 J $m^{-3}K^{-1}$. The estimated R_{zf} 's, using these values, are tabulated in Table 2.3. As expected, R_{zf} attains its lowest value (~0.7-1) for the thermofoam surface while it is maximum for bare concrete covered with aluminum foil (~ 250-395).

Calculation of R_{zf} for laboratory observations

We take ΔT_i = 1.2 K and τ_{rad} = 25 s for low emissivity and high thermal inertia (Plate + aluminum foil). Now, net flux in upward direction

$$(F_s)=\mathcal{E}_b \boldsymbol{\sigma} T_b^4 + (\mathbf{1} - \boldsymbol{\mathcal{E}_b}) \boldsymbol{\sigma} T_s^4 \mathcal{E}_s f_1 - \boldsymbol{\mathcal{E}_b \mathcal{E}_s \sigma} T_s^4 f_1 \quad (2.11)$$

Where $\mathcal{E}_b$ and $\mathcal{E}_s$ are emissivity of bottom and Sky boundary respectively, $f_1$is fraction of radiation reaching in the test section from Sky.

By using the value of $\mathcal{E}_b$= 0.05, $\mathcal{E}_s$= 0.9, T_b = 300 K, T_s = 280 K and f_1 =0.7 and

$\mathcal{E}_b$= 0.9, $\mathcal{E}_s$= 0.9, T_b = 295 K, T_s = 280 K and f_1 =0.7. We obtained F_s is 217 Wm^{-2} and

200 Wm^{-2} respectively. Further, the thermal heat capacity ($\rho_s C_{Ps}$) for aluminum plate is about 2 × 106 J m-3K-1, and that for thermofoam is about 5 × 104 J m-3K-1.The estimated value of R_{zf} using these values is 8.5 for low emissivity and high thermal inertia and 0.08 for high emissivity and low thermal inertia.

Table. 2.3 Ramdas-Zdunkowski factor (R_{zf}) for various surfaces in case of field and laboratory case.

Type of surface	Boundary properties	R_{zf}		Expected profile	Intensity of LTM	
		Field	Lab		Lab	Field
Aluminium plate with black paint	High emissivity with $e_g = 0.91$, & high thermal inertia	20 - 32		LTM	0.68 K	2 - 7 K
Aluminium plate with Aluminium foil	Low emissivity with $e_g = 0.05$, & high thermal inertia	250 - 395	8.5	Strong LTM	1.2 K	7 – 13 K
Aluminium plate with thermofoam with brown paper as its top surface	High emissivity with $e_g = 0.89$, & low thermal inertia	0.7 - 1	0.05	Inversion	Inversion	Inversion
Aluminium plate with thermofoam with Aluminium Foil as its top surface	Low emissivity with $e_g = 0.05$, & low thermal inertia	9 - 14		Weak LTM	0.28 K	2 – 5 K

2.5.9 Effect of Sky temperature (T_{Sky})

The LTM-type equilibrium profile is initially obtained where radiation boundary temperature is 280 K. An opaque sheet of thermofoam is then inserted between the circulation region and the sky (radiation boundary). In such a case, the air layer in the test section cannot interact with the sky, leading to disappearance of the LTM-type profile and a steady state profile is obtained after a period of ~ 15 min. However, the temperature of opaque sheet lying on the second chamber starts increasing and after ~ 15 min, it attains a constant value (315 K) along with the air layers in the test section. The opaque sheet then behaves as the hotter radiation boundary and the air layer as well as the boundaries can radiatively interact with the opaque

sheet (hot sky resulting temperature profile shows heating with respect to the linear conduction profile. The temperature difference between boundaries are different in both the cases (before and after blocking) and after normalization, in case of LTM-equilibrium, the deviation from conduction profile is 58% (cooling with respect to linear conduction profile) where temperature of radiation boundary is at 280 K and 22% (heating with respect to linear conduction profile) where temperature of radiation boundary is at 315 K. These observations are shown in Fig. 2.32a.

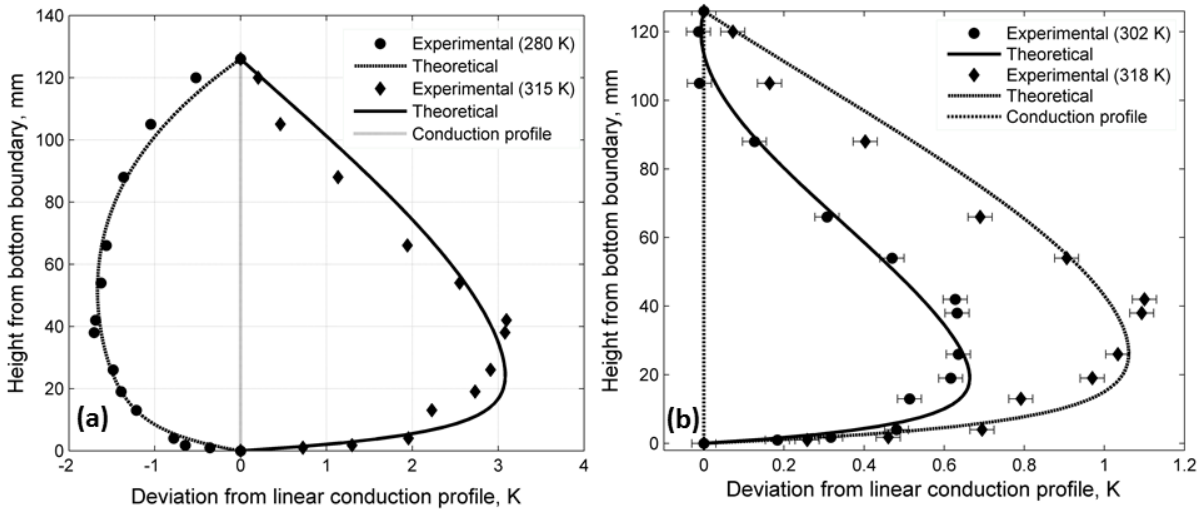

Figure 2.32 Deviation from linear conduction profile in case of different radiation boundary temperatures. (a) Solid circle symbol corresponds to radiation boundary temperature is 280 K and solid diamond symbol corresponds to radiation boundary temperature is 315 K. The solid lines represent theoretical results where optical thickness distribution is $\hat{\alpha}(z) = 1.4 \exp(-z/0.05)+0.03$. (b) The solid circle symbol corresponds to radiation boundary temperature which is 302 K and solid diamond symbol corresponds to the radiation boundary temperature which is 318 K. The solid lines represent theoretical results where optical thickness distribution is $\hat{\alpha}(z) = 1.4 \exp(-z/0.05)+0.03$.

The experiments have been performed with the temperature of the radiation boundary at 302 K and 318 K. In this case, aerosol distribution and emissivity of the bottom boundary are same. In Fig. 2.32b, deviation from linear conduction profile in case various radiation boundary have been plotted with respect to height. The maximum deviation is at around 40 mm and 0.65 K and 1.1 K for temperature of radiation boundary is 302 K and 318 K respectively. In Fig. 2.33, the cooling and heating profiles are plotted with respect to the linear conduction profile. The maximum deviation from the linear conduction profile is obtained at around 40 mm from the bottom boundary. In Fig. 2.32, theoretical calculation has been plotted for an assumed exponential distribution of aerosol particles; the resulting optical thickness distribution is $\hat{\alpha}(z) = 1.4 \exp(-z/0.05)+0.03$. There is a good agreement between the experimental and theoretical results.

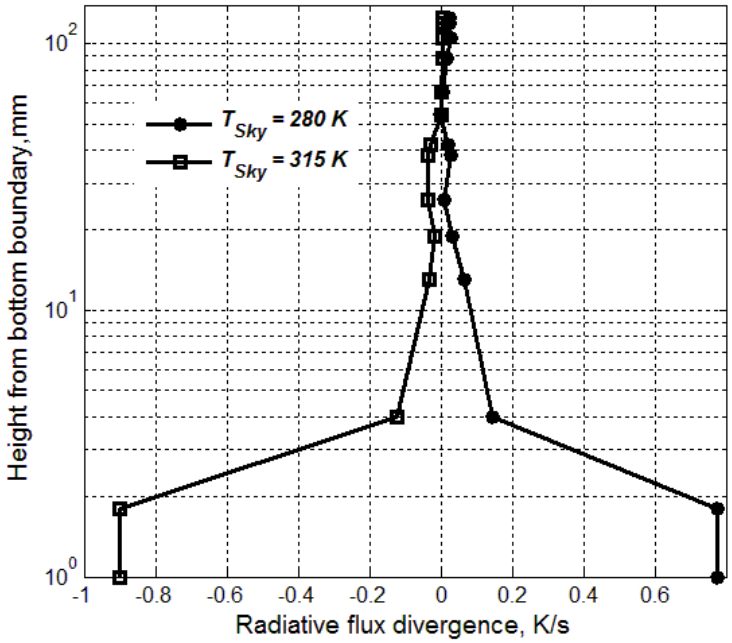

Figure 2.33 Cooling and heating rate with respect to height from the bottom boundary. Temperature of radiation boundary is 280 K and 315 K, in case of cooling and heating respectively.

The radiation flux divergence for sudden change in sky temperature is also estimated. The cooling rate is around -0.9 K/s near the bottom boundary in case of LTM- equilibrium and its decay till the height of 40 mm from bottom boundary. The heating rate is also approximately the same and it is 0.8 K/s near the bottom boundary and it decays till the height of around 40 mm from the bottom boundary. Thus, the large cooling and heating rate near the bottom boundary predicted is solely due to the radiative effects of the inhomogeneous aerosol concentration field.

2.6 Experimental observations and theoretical[4] results for LTM-type profiles

The theoretical analysis involves several simplifying assumptions. We work within a plane parallel formulation where the radiatively participating heterogeneous medium is conformed between infinite parallel plates. The plates are isothermal and are gray diffuse emitters and reflectors. Since a stable temperature stratification is maintained in the experiments, the heat transfer is assumed to be due to conduction and radiation alone. With regard to radiation modeling, we assume the participating medium to be gray. The dominant radiative forcing in the experiments arises from suspended aerosol particles; the gray medium assumption is a reasonable one in this case, since the absorption coefficients of solid and liquid in general are far smoother functions of the wavelength (in the IR range) when compared to gases. Finally, the integration over zenith angles that account for the directional nature of radiative transfer is accounted for via a diffusivity factor.

[4] Details of the theoretical calculation are given in Ponnulakshmi (2013).

The one dimensional energy balance to the gas layer is $\rho C_p \frac{dT}{dt} = k\frac{d^2T}{dz^2} - \frac{dF_z}{dz}$ (2.12) where k is the thermal conductivity, ρCp the medium heat capacity, and F_z the vertical component of the radiant flux. Since radiation is a non-local phenomenon, the governing equation for radiative transfer is an integro- derential equation in the general case. However, with the use of the Milnc-Eddington differential approximation [Goody (1956), Larson (2011)],

one may obtain a differential equation governing F_z:

$$\frac{d^2F_z}{dz^2} - \left(\frac{1}{\alpha}\right)\left(\frac{d\alpha}{dz}\right)\left(\frac{dF_z}{dz}\right) - 3\alpha^2F_z = 4\alpha\sigma\frac{dT^4}{dz} \qquad \ldots\ldots\ldots\ldots \quad (2.13)$$

Here, α is an effective absorption coefficient that includes contributions from both radiatively participating gases as well as suspended particulates. When radiative forcing due to aerosols is dominant then it can be written as $\alpha = A\alpha_h n(z)$ where n(z) is the aerosol number density field, and $A\alpha_h$ is the absorption cross section of a single aerosol particle. The above expression for α is valid in the dilute limit, when the aerosol contribution is linearly related to the number density. The number densities, inferred from a match with experimental observations, do fall in the dilute regime, and any form of radiative interactions between aerosol particles (absorption or multiple scattering) is therefore neglected.

Equation (2.13) may be linearized (since the temperature difference between the boundaries is small), and combined with the energy equation (2.12). At steady state, the resulting non-dimensional equation governing the temperature field is

$$\frac{d^3\theta}{dz^3} - \left(\frac{1}{\hat{\alpha}}\right)\left(\frac{d\hat{\alpha}}{dz}\right)\frac{d^2\theta}{dz^2} - 3\hat{\alpha}^2\left(\frac{d\theta}{dz}\right) - 3\hat{\alpha}\chi\left(\frac{d\theta}{dz}\right) = 3\hat{\alpha}^2\eta\psi \qquad (2.14)$$

Where $\chi = \frac{16\sigma T_c^3 h}{3k}$, $\hat{\alpha} = \alpha h$ and $\eta = \frac{\sigma T_c^4 h}{k(T_1 - T_0)}$ .here $\theta = \frac{T - T_0}{T_{1-T_0}}$ is the normalized temperature,

T_c is the mean of bottom and top plate temperatures, h is the separation of the plate, T_0 and T_1 are the bottom and top plate temperatures respectively, ψ is the (constant) total heat flux, $\hat{\alpha}$ is the dimensionless optical thickness in unit of medium depth. $\frac{\chi}{\hat{\alpha}}$ is the ratio of radiative to thermal conductivities, and η denotes ratio of radiative flux to conductive fluxes. Since there are 4 unknowns (3 integration constants and the unknown total heat flux), four boundary conditions are needed. The first two are no-slip conditions at the top and bottom boundaries: θ = 0 at z = 0, & θ = 1 at z = 1. As mentioned earlier, fixing the plate temperature fixes both the conductive and radiative boundary conditions. Additional boundary conditions for the radiative fluxes, originally given by Goody (1956), are:

$$\left.\frac{d^2\theta}{dz^2}\right|_{z=0} = \left(2\upsilon_1\hat{\alpha}\eta\psi + 2\upsilon_1\hat{\alpha}\frac{d\theta}{dz}\right)_{z=0}$$

$$\left.\frac{d^2\theta}{dz^2}\right|_{z=1} = \left(-2\upsilon_2\hat{\alpha}\eta\psi - 2\upsilon_2\hat{\alpha}\frac{d\theta}{dz}\right)_{z=1}$$

In non-dimensional form, where $\boldsymbol{\varepsilon}_1$ and $\boldsymbol{\varepsilon}_2$ are the bottom and top plate emisivities, respectively, and

$\upsilon_1 = 2\left(\frac{1}{\varepsilon_1} - \frac{1}{2}\right)$ and $\upsilon_2 = 2\left(\frac{1}{\varepsilon_2} - \frac{1}{2}\right)$ Equation (2.15)

Can be solved numerically using a linear shooting method Curtis Gerald and Patrick Wheatley (2003). The numerical code is validated using known analytical results for a gray

homogeneous medium. For instance, the solution for the two-plate problem, in the linearized approximation, is given by Goody (1956)

$$\theta(z)=\frac{Le^{pz}}{p}-\frac{Le^{(1-z)p}}{p}-\frac{\eta\psi z}{1+\chi}-\frac{L(1-e^{p})}{p} \qquad (2.16)$$

Where $L= 2\hat{\alpha}\,\chi\,\left[p(e^{p}-1)+2\hat{\alpha}(e^{p}+1)+\frac{4p\chi(e^{p}-1)}{3\hat{\alpha}(1+\chi)}\right]^{-1}$

where $p=\sqrt{3\hat{\alpha}^{2}\,(1+\chi)}$ is the inverse of the conductive boundary layer thickness.

LTM experiments have been performed with various heights of the test section and emissivity of the bottom boundary. For comparing the experimental and theoretical results, experiments at 130 mm height of the test section has been considered. For these experiments, the aerosol number density is maintained in the same level as far as possible. For theoretical calculation, we need the temperature of the bottom boundary and radiation boundary, as well as the emissivity of bottom and sky boundary. These data have been taken from the corresponding experiment. Only 60% cold radiation (from SKY) can enter into the test section as there are two chambers of transparent polythene sheets. The aerosol number density near the ground is not available. However, the average aerosol number density is estimated in the test section and it is around 10^{10}/ m^3. The details of the distribution of aerosols have been given in section 2.5.4 and it is a heterogeneous distribution in the test section; the resulting optical thickness distribution is $\hat{\alpha}(z)$ =1.4exp(-z/0.05)+0.03. In Fig. 2.34, a good agreement between experimental observations and theoretical calculations is demonstrated. In this case, the bottom boundary of the test section is reflective (low emissivity ~0.05); the intensity of the minima is 1.22 ± 0.03 K and height of the minima is 26

± 1 mm at steady state. For the same experiment, temperature gradient and cooling rate have been plotted with respect to height of the test section. The temperature gradient and radiative flux divergence are in shown in Fig. 2.35. Fig. 2.35a and indicate a large temperature gradient O (350 K/m) near the bottom boundary and decays over a length scale of the order of 40 mm. The radiative flux divergence near the bottom boundary is 0.78 K/s and decays over a length scale of the order of 40 mm. Decay length scale highly depends on LTM-height.

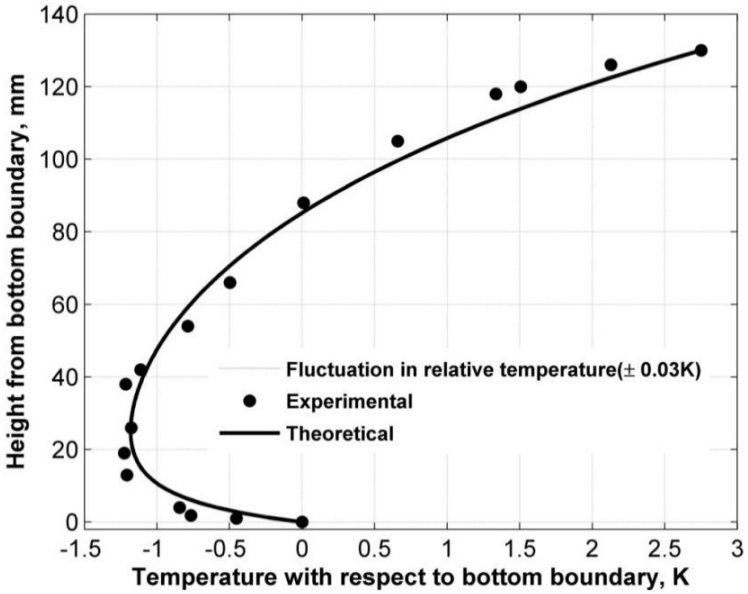

Figure 2.34 Temperature profiles in the test section for reflective ($\varepsilon_g \approx 0.05$) bottom boundary. T_{sky} is held at 280 K, while T_g is at 300 K. Solid symbols correspond to experimental observation. Solid curve represents the result of theoretical calculation, where optical thickness distribution is $\hat{\alpha}(z) = 1.4 \exp(-z/0.05)+0.03$.

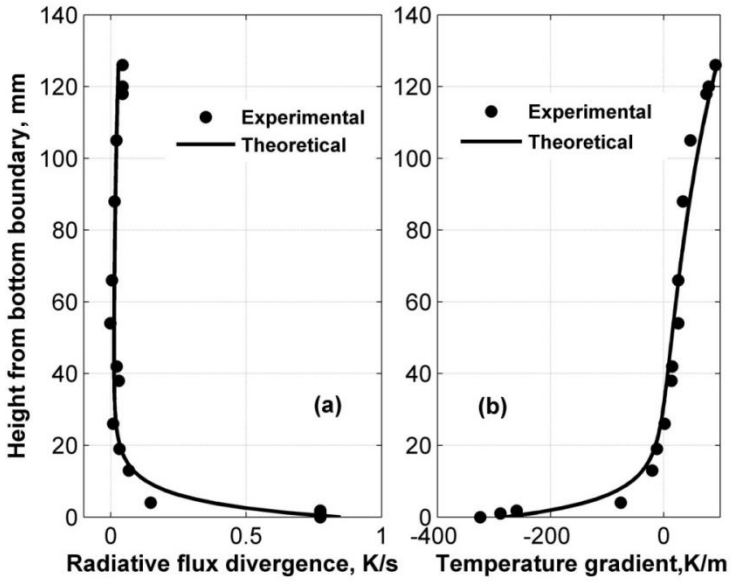

Figure 2.35 Radiative flux divergence (cooling rate) and temperature gradient for low emissivity bottom boundary plotted with respect to height in (a) and (b) respectively. Solid symbols correspond to experimental observations. Solid curve represent the result of theoretical calculation, where optical thickness distribution is $\hat{\alpha}$(z) =1.4 exp(-z/0.05)+0.03.

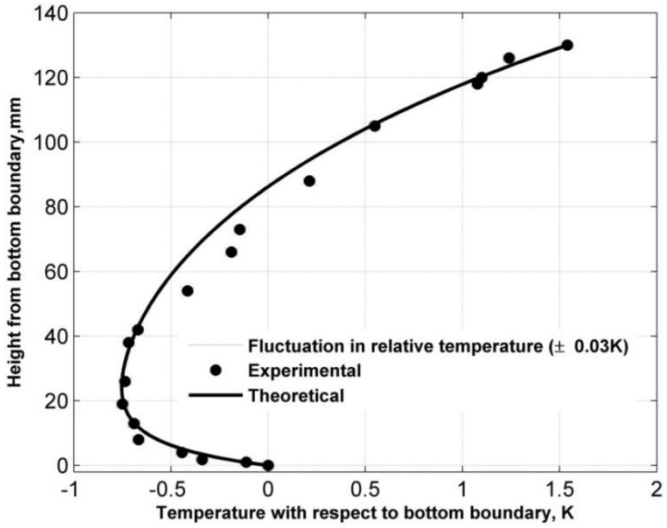

Figure 2.36 Temperature profiles in the test section for black ($\varepsilon_g \approx 0.9$) bottom boundary. T_{sky} is held 280 K, while T_g is at 300 K. solid symbols correspond to experimental observation. Solid curve represents the result of theoretical calculations, where optical thickness distribution is $\hat{\alpha}$(z) =1.4 exp(-z/0.05)+0.03.

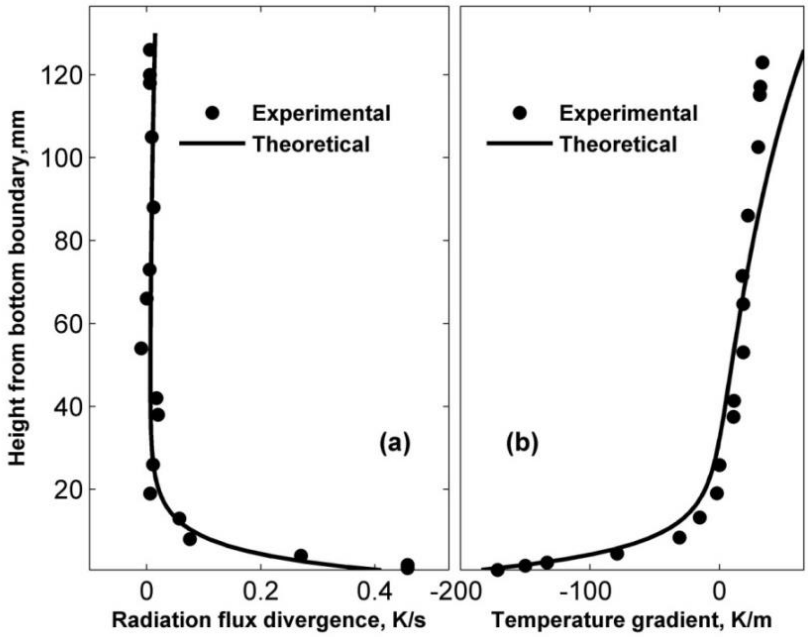

Figure 2.37 Radiative flux divergence (cooling rate) and temperature gradient for high emissivity bottom boundary plotted with respect to height in (a) and (b) respectively. Solid symbols correspond to experimental observations. Solid curve represents the result of theoretical calculation, where optical thickness distribution is $\hat{\alpha}(z) = 1.4 \exp(-z/0.05) + 0.03$.

The black bottom boundary (high emissivity ~0.9) is shown in Fig. 2.36, intensity of minima is 0.75 ± 0.03 K and height of minima is 26 ± 1 mm. The temperature gradient and radiative flux divergence are in shown in Fig. 2.37. Fig. 2.37a shows a large temperature gradient O(200 K/m) near the bottom boundary and the radiative flux divergence profile shows a region of intense radiative cooling near the bottom boundary, which is 0.4 K/s and decays over a length scale of the order of 26 mm. The temperature gradient near the bottom boundary and the radiative flux divergence profile are lower in magnitude than that observed in the previous case of reflective surface.

2.7. Conclusion

The formation of an LTM-type profile must be regarded as the norm under calm and clear-sky conditions. The occurrence of such a profile implies that the near-surface air layers (rather than ground) cool faster after sunset, and thereby, drive the cooling process after sunset. Since the inversion and LTM-type profiles exhibit temperature gradients of opposing signs, a transition from one to the other implies a change in the surface boundary condition which evidently has implications for NBL modeling. LTM-type profiles have been reproduced for various bottom boundaries in the laboratory and an intensity of minimum, in case of low emissivity is approximately double than high emissivity bottom boundary, which is similar obtained in the field. The temperature gradient and cooling rate, near the bottom boundary, in the case of low emissivity bottom boundary is higher than high emissivity bottom boundary. A near-surface concentration gradient of suspended aerosols is proposed as the cause for the preferential hyper-cooling and confirmed from laboratory experiments. The presence of aerosols, which is not normally accounted for in radiation models, resolves the apparent contradiction between observations of radiative cooling presented here, and theoretical predictions reported earlier of near-surface warming in a homogeneous atmosphere. In contrast to the *ad-hoc* nature of the temperature slip at the ground, which is often assumed in atmospheric simulations, the existence of the near-surface heterogeneity (leading to the LTM) provides a natural explanation for the observed hyper-cooling.

The distributions of aerosols have been estimated in the test section and it is heterogeneous via the image analysis method. An intensity of minimum of LTM-type is found to depend on seasonal aerosols. The intensity of minimum in pre-monsoon case (Feb-May) is

approximately double than in the monsoon case (July-Sept) with a similar condition of Sky temperature, temperature difference between top and bottom boundary, and emissivity of bottom boundary. Further, the time constant for various bottom boundaries and various Sky temperatures (radiation boundary) has been estimated, and it is found to depend on the emissivity of the bottom boundary, temperature of radiation boundary, and aerosol distribution. Finally, radiation time constant is estimated in the case where temperatures of the boundaries were controlled and they are matching well, both experimentally and numerically.

CHAPTER 3

Experiments for coupled boundary condition for radiation and conduction

3.1 Introduction

Micro-meteorological processes in the nocturnal boundary layer like the formation of fog, the development of inversion layers, and air quality are controlled by heat transfer and vertical temperature distribution close to the ground. Our recent studies on the micro-meteorological phenomenon known as the Ramdas paradox or the lifted temperature minimum (LTM) emphasize the role of the medium heterogeneity (presence and vertical distribution of aerosols) in determining the thermal structure of the nocturnal boundary layer under calm cloudless conditions [Mukund et al. (2013)]. The phenomenon involves the preferential cooling of near-surface air layers, and leads to singular temperature profiles that exhibit elevated minima. The de-coupled radiation conduction and convection boundary conditions that led to this cooling were reproduced in a novel laboratory experimental setup and resulted in LTM-type profiles (the laboratory Ramdas layer).

Bhat [Bhat (2006)] showed that during the daytime preferential heating of air layers happens just above the sea surface due to suspended salt particles, resulting in a temperature profile that exhibits a lifted temperature maxima. On a larger scale, aerosols are also responsible for the radiative process in the atmosphere both in the short-wavelength and the long-wavelength (IR) bands. Excessive aerosols following a volcanic eruption can reduce visibility and atmospheric temperature by blocking solar radiation. In recent times, aerosols are also being considered for geo-engineering to mitigate greenhouse effects, for example by increasing

cloud brightness [Latham et al. (2008)]. The major concern in using aerosols for mitigating global warming is our limited knowledge on climate forcing by aerosols. Moreover, effects of aerosols have to be quantified in other applications like solving inverse radiation problems in an aerosol laden atmosphere and micro dynamics of clouds. Radiant energy transfer through participating media that can absorb, emit and scatter radiation is important in a wide range of fields such as furnaces, engine combustion chambers at high temperatures, rocket propulsion, glass manufacturing, nuclear explosions, hypersonic shock layers, plasma generators for nuclear fusion, and the earth's atmosphere [Siegel and Howell (2002)]. The findings reinforce the importance of participating medium heterogeneity even on laboratory length scales, and have motivated us to examine experimentally and theoretically, the role of a medium looked with aerosols in a simpler geometry originally used in the context of the classical Rayleigh-Benard problem – that is an aerosol laden participating medium sandwiched between infinite parallel plates maintained at different temperatures.

Aerosols, in general, are better emitters and absorbers than gases and play an important role in the cooling and heating of atmosphere. For modeling radiative heat transfer process involving aerosols, we have to know their life cycle, chemistry, number density, and size distribution profiles in the atmosphere apart from their radiative properties. Various groups have studied the vertical number-density profile of aerosols in the atmosphere. In a variety of situations, a layer of suspended particles exhibits a sharp decrease in particle concentration with layer height due to a balance between sedimentation and turbulent mass diffusion [Graf and Cellino (2002); Nielsen and Teakle (2004)]. Classically, the number density variation with height in suspension is described by the Rouse profile [Nielsen and Teakle (2004)]. In

the stable, nocturnal atmospheric boundary layer, aerosol concentration profiles measured by LIDAR [Devara and Raj (1993)] show an increase in concentration towards the surface and can be fitted by Rouse profile. Most of these measurements are done starting from few tens of meters above the ground level, and up to few kilometers. Another important factor governing radiative transfer in the atmosphere is the ground emissivity. There has been an increasing interest in accounting for the variation in the ground emissivity for remote sensing, numerical weather prediction, and climate modeling [Snyder et al. (1998)] applications. Thus, there is a need to study the role of radiation in a medium, with particle suspension, for developing atmospheric models according for radiative heat transfer in air layer laden with aerosols.

Earlier, experimental studies aimed to study the stabilization of radiation on traditional Rayleigh Benard configuration, wherein the radiatively participating medium is held between parallel plates at fixed temperatures. In a seminal paper, Goody [Goody (1956)] examined analytically the effect of radiation on the onset of convection in a (compositionally) homogeneous gray medium in the optically thick and thin regime. He showed that the inclusion of a radiative source term introduced two modifications (a) a non-linear base-state temperature profile with a reduced gradient in the bulk; (b) an additional (radiative) relaxation mechanism for the fluid parcel. Both effects are evidently stabilizing, and for typical parameter values, they showed a modest enhancement in the critical Rayleigh number. The first quantitative experiment to study this effect was by Gille and Goody (1964). They used pure ammonia gas and dry air as a radiatively participating medium between two parallel plates. The observed pre-convective temperature profile was shown to be different

from the linear, diffusive conduction profile. Further, the critical Rayleigh number (at which the convection starts) was found to be higher than the traditional Rayleigh number (1708). Further, the authors developed a non-gray model to study the base state. Their results matched well with the experiments.

Later analysis by Spiegel, 1960; Christophorides and Davis, 1970 were aimed at improving the theoretical analysis by Goody, 1956. Schimmel and Olsofka (1970) carried out experiments to study the effect of radiation on the base state. The experiments ware done for four gas mixtures; pure Carbon dioxide, pure nitrous oxide, a mixture of carbon dioxide and nitrous oxide and a mixture of carbon dioxide and methane. W.P. Schimmel (1970) presented nongray radiation-conduction interaction in a radiating gas bounded by two gray infinite parallel plates. He has also considered a special case of one black surface with diffusely emitting and specularly reflecting surfaces. Cess and Sotak (1964) have considered the case of reflection conditions with the pure radiating gray gas. Crosbie (1970) has presented the study of energy transfer due to combined effects of conduction and radiation in a medium with frequency dependent properties. He has compared the results with those for the gray case. Further, the validity of the gray model against the non-gray model was discussed by comparing the results with the experiments. Novotny and Olsofka (1970) extended the above work by examining the effect of mixing a non-participating gas with a participating gas. Audunson and Gebhart, 1972 further analyzed the effect of absorbing (ammonia gas) and non-absorbing gases on a natural convection boundary layer formed adjacent to a vertical flat surface with uniform heat flux input. The effect of surface emittance was also studied. The results show that the presence of radiation increases the convective heat transfer by as much

as 40%. Arpaci and Gozum, 1973, developed a semi-gray analysis to investigate the onset of convection. The non-grayness was characterized by Rossland and Planck mean absorption coefficient. Bdeoui and Soufiani, 1997 included the detailed spectral nature of the emitting gases to model radiation. The analysis was done for arbitrary surface emissivities. Their analysis predicted that the stability for the onset of convection increase with temperature and optical depth and decrease with boundary emissivities. Hutchison and Richards, 1999, conducted experiments to determine the onset of stability using pure Carbon dioxide and dry air. The measurements showed a 7-20% increase in critical Rayleigh number. The linear stability analysis has been extended to atmospheric context by Larson (2000 and 2001). The stability criteria were examined in terms of the radiative Rayleigh number. However, there are no experiments demonstrating natural aerosol as a radiative participating medium.

Aerosols and meteorological clouds represent major sources of uncertainty in understanding past and future climate variability. Each phenomenon influences the climate system via radiative forcing. Elevated absorbing aerosols play an important role in atmospheric heating by affecting the general circulation and altering the radiation and dynamical states of the entire monsoon system. Aerosols in the form of tiny suspended particles in the atmospheres intercept solar radiation reaching the Earth's surface and interact strongly with the processes of formation of clouds and rain. Thus, quantifying changes in aerosols and clouds, determining the underlying causes of such variability, and uncovering the manner by which aerosol and cloud radiative forcing alters the evolution of the climate-system are of utmost importance. The quantitative understanding and predictability of aerosols, clouds and precipitation properties, their interactions, and effects in the climate system are, however,

very limited. Much of aerosol–cloud precipitation interaction processes are still not well understood. The lack of simultaneous in-situ measurements of cloud microphysical properties, chemical tracer compounds and aerosol characteristics within lower clouds has been a serious obstacle to evaluate detailed cloud-resolving models that can be used for obtaining a more comprehensive understanding of aerosol-cloud interaction.

Earlier studies demonstrated the radiative effect of a homogeneous medium (the composition of the radiative participating medium is homogeneous). In this chapter, we investigate the radiative effect of radiatively participating medium with aerosols. The predicted theoretical results are then compared with the experiments. The theoretical model consists of an absorbing-emitting gas bounded by two gray infinite parallel plates. Specific results are presented for lower atmosphere's natural aerosols with fixed plate spacing and temperature difference between plates for different boundaries emissivities and for various aerosols concentrations (optical depth).

3.2 Coupled boundary condition experiments (Two plate experiments)

A schematic of the laboratory set up is shown in Fig. 3.1. The test section has a cross-sectional area of 1600 cm^2 (80 cm by 80 cm), and a height of 13 cm. The test section contains ambient air, which may be regarded as the representative of the air layers near the ground. The bottom and top of the test section are made with 5 mm thick anodized aluminum plates. The bottom of the plate is in contact with water in a tank and the tank is provided with pipes for circulating water at an appropriate temperature, thus fixing the bottom boundary temperature of the test section. Both sides of the test section's wall are made of 40 mm thick thermofoam to prevent near-wall convection due to the hot air at a different temperature

being circulated in the circulation region that enclosed the test section. Al foil (low emissivity) is covered on the inner side walls of the test section to reduce radiation interaction from the side walls. There is a secondary air circulation section overlying the top boundary of the test section. All five sides of this section are made of 40 mm thick thermofoam to help to maintain steady-state (i.e., to avoid heat loss to the surrounding). The region between this polythene enclosure and the test section is the circulation section. With the help of a heater-blower unit, air, at a specific temperature T_{circ} (measured at the outlet of the heater- blower unit), is circulated through this region.

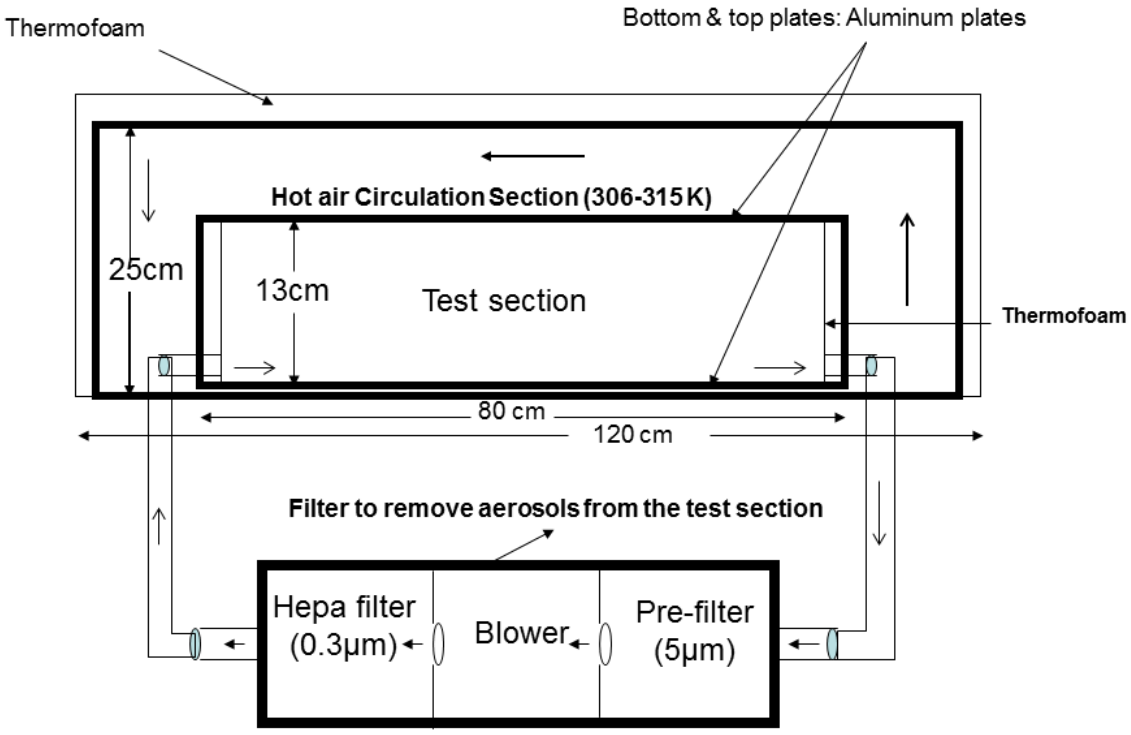

Figure 3.1 Schematic of the laboratory set up

This fixes the temperature T_{top} of the top boundary of the test section, and provides the conduction, convection and radiation boundary condition at the upper boundary of the test

section. Thus, by controlling the temperature of the bottom plate of the test section and that of the gas being circulated through the air circulation region, an appropriate temperature differential (stable or unstable) can be established across the test section. The temperature profiles inside the test section were measured using K-type (chromel-Alumel) thermocouples. Fig. 3.2 shows the front view of the actual laboratory set up.

Figure 3.2 Laboratory experimental set up.

The measurements were taken with different aerosol concentrations inside the test section. The concentration of aerosols in the atmosphere varies with season (low during monsoon and maximum during the pre-monsoon season). The test section was provided with inlet and outlet to filter aerosols using air filter (HEPA filter). The air in the test section is pumped out through a port, and after filtering, is re-admitted into the test section through another port; filtering is carried out for different durations to get various aerosol concentrations. Measurements were also done by varying the emissivity of the boundaries of the test section either by coating them with black paint (high- emissivity surface) or by covering them with a

highly polished aluminum sheet (low-emissivity surface). These experiments would be referred to as 'two-plate experiments' (radiative -conductive). For measurement of aerosols number density in the test section, a vertical laser sheet using a Nd-Yag pulsed green (532 um wavelength) laser and a Nikon-D90 digital camera were used. The thickness of the light sheet is about 2.5 mm. Images correspond to ~ 45 % of the test section, taken for the region from 2 cm to 8 cm above the bottom boundary.

3.3 Theoretical formulation*

The theoretical analysis involves several simplifying assumptions. We work within a plane parallel formulation where the radiatively participating heterogeneous medium is conformed between infinite parallel plates. The plates are isothermal, and are gray diffuse emitters and reflector. Since a stable temperature stratification is maintained in the experiments, the heat transfer is assumed to be due to conduction and radiation alone. With regard to radiation modeling, we assume the participating medium to be gray. The dominant radiative forcing in the experiments arises from suspended aerosol particles; the gray medium assumption is a reasonable one in this case, since the absorption coefficients of solid and liquid in general are far smoother functions of the wavelength (in the IR range) when compared to gases. Finally, the integration over zenith angles that account for the directional nature of radiative transfer is accounted for via a diffusivity factor.

The one dimensional energy balance to the gas layer is

$$\rho C_p \ \frac{dT}{dt} = k \frac{d^2 T}{dz^2} - \frac{dF_z}{dz} \qquad (3.1)$$

* Details of the theoretical calculation are given in Ponnulakshmi (2013)

where k is the thermal conductivity, ρCp the medium heat capacity, and F_z is the vertical component of the radiation flux. Since radiation is a non-local phenomenon, the governing equation for radiative transfer is an integro derential equation in the general case. However, with the use of the Milnc-Eddington differential approximation [Goody (1956), Larson (2011)], one may obtain a differential equation governing F_z:

$$\frac{d^2F_z}{dz^2} - \left(\frac{1}{\alpha}\right)\left(\frac{d\alpha}{dz}\right)\left(\frac{dF_z}{dz}\right) - 3\alpha^2 F_z = 4\alpha\sigma\frac{dT^4}{dz} \qquad (3.2)$$

Here, α is an effective absorption coefficient that includes contributions from both radiatively participating gases as well as suspended particulates. When radiative forcing due to aerosol particle is dominant, then it can be written as $\alpha = A\alpha_h n(z)$ where n(z) is the aerosol number density field, and $A\alpha_h$ is the absorption cross section of single aerosol particle. The above expression for α is valid in the dilute limit, when the aerosol contribution is linearly related to the number density. The number densities, inferred from a match with experimental observations, do fall in the dilute regime, and any form of radiative interactions between aerosol particles (absorption or multiple scattering) is therefore neglected.

Equation (3.2) may be linearized (since the temperature difference between the boundaries is small), and combined with the energy equation (3.1). At steady state, the resulting non-dimensional equation governing the temperature field is

$$\frac{d^3\theta}{dz^3} - \left(\frac{1}{\hat{\alpha}}\right)\left(\frac{d\hat{\alpha}}{dz}\right)\frac{d^2\theta}{dz^2} - 3\hat{\alpha}^2\left(\frac{d\theta}{dz}\right) - 3\hat{\alpha}\chi\left(\frac{d\theta}{dz}\right) = 3\hat{\alpha}^2\eta\psi \qquad (3.3)$$

Where, $\chi = \frac{16\sigma T_c^3 h}{3k}$, $\hat{\alpha} = \alpha h$ and $\eta = \frac{\sigma T_c^4 h}{k(T_1 - T_0)}$ .here $\theta = \frac{T - T_0}{T_{1-T_0}}$ is the normalized temperature,

T_c is the mean of bottom and top plate tempetature, h is the separation of the plate, T_0 and T_1 are the bottom and top plate temperature respectively, ψ is the (constant) total heat flux, $\hat{\alpha}$ is the dimensionless optical thickness in unit of medium depth. $\frac{\chi}{\hat{\alpha}}$ is the ratio of radiative to thermal conductivities , and η denotes ratio of radiative flux to conductive fluxes. Since there are four unknowns (3 integration constants and the unknown total heat flux), four boundary conditions are needed. The first two are no-slip conditions at the top and bottom boundaries: θ = 0 at z = 0,& θ = 1 at z=1.As mentioned earlier , fixing the plate temperature fixes both the conductive and radiative boundary conditions. Additional boundary conditions for the radiative fluxes, originally given by Goody (1956), are:

$$\left.\frac{d^2\theta}{dz^2}\right|_{z=0} = \left(2\upsilon_1\hat{\alpha}\eta\psi + 2\upsilon_1\hat{\alpha}\frac{d\theta}{dz}\right)_{z=0}$$

$$\left.\frac{d^2\theta}{dz^2}\right|_{z=1} = \left(-2\upsilon_2\hat{\alpha}\eta\psi - 2\upsilon_2\hat{\alpha}\frac{d\theta}{dz}\right)_{z=1}$$

in non-dimensional form, where $\boldsymbol{\varepsilon}_1$ and $\boldsymbol{\varepsilon}_2$ are the bottom and top plate emisivities, respectively, and

$\upsilon_1 = 2\left(\frac{1}{\varepsilon_1} - \frac{1}{2}\right)$ and $\upsilon_2 = 2\left(\frac{1}{\varepsilon_2} - \frac{1}{2}\right)$

Equation (3.3) can be solved numerically using a linear shooting method, Curtis Gerald and Patrick Wheatley (2003). The numerical code is validated using known analytical results for a gray homogeneous medium. For instance, the solution for the two-plate problem, in the linearized approximation, is given by Goody (1956)

$$\theta(z)=\frac{Le^{pz}}{p}-\frac{Le^{(1-z)p}}{p}-\frac{\eta\psi z}{1+\chi}-\frac{L(1-e^{p})}{p} \quad (3.4)$$

where $L= 2\hat{\alpha}\,\chi\left[p(e^{p}-1)+2\hat{\alpha}(e^{p}+1)+\frac{4p\chi(e^{p}-1)}{3\hat{\alpha}(1+\chi)}\right]^{-1}$

where $p=\sqrt{3\hat{\alpha}^{2}(1+\chi)}$ is the inverse of the conductive boundary layer thickness.

3.4. Results and discussion

Temperature profiles in the test section are initially isothermal. Once the hot-air circulation at the top and water circulation below the bottom boundary begins, steady state (equilibrium) is achieved after 2-3 hours, as shown in Fig. 3.3. At equilibrium, the standard deviation in temperature at various heights inside the test section and the average fluctuation in the temperature profiles at equilibrium are shown in Fig. 3.4.

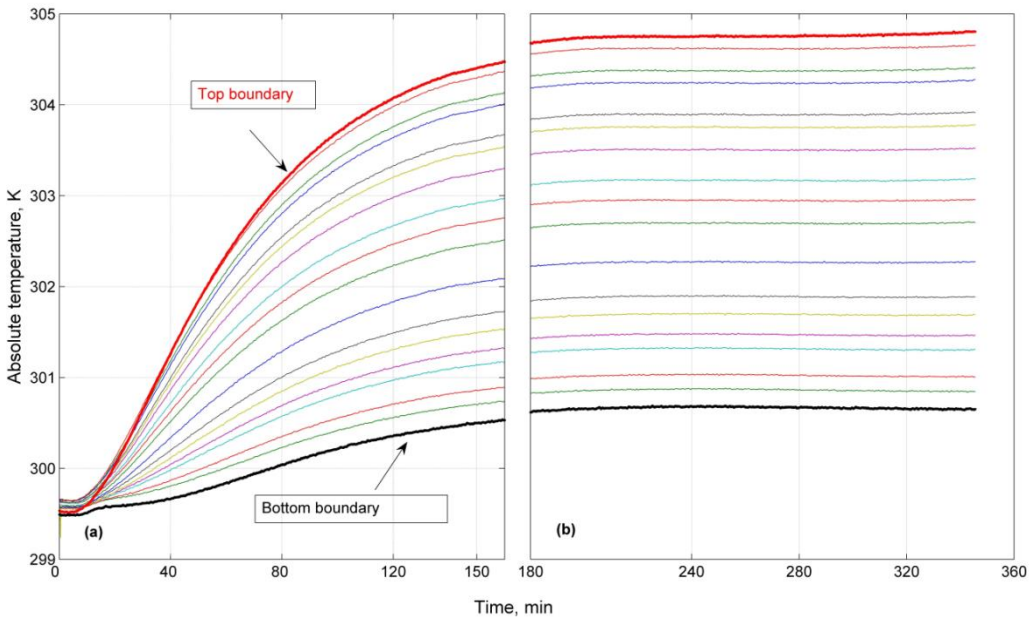

Figure 3.3 Temperature traces with top and bottom boundary at (a) transient state and (b) steady state.

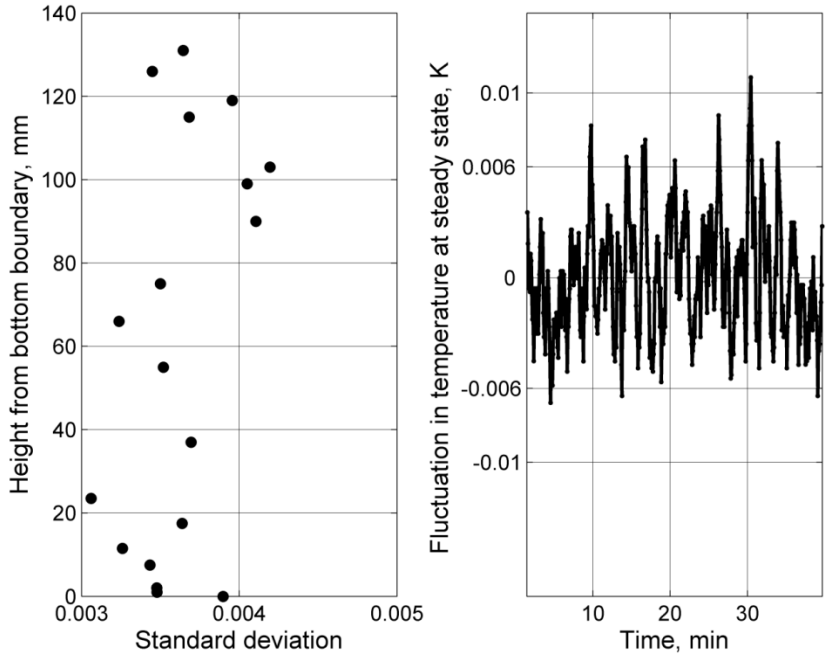

Figure 3.4 (a) The standard deviation in temperature at various heights inside the test section and (b) The average fluctuation in the temperature profiles at equilibrium.

3.4.1. Varying aerosols concentration field

Keeping the bottom and top boundaries similar, and with a high emissivity (0.9), the aerosol concentration inside the test section is varied. The height of the test section is 13 cm. The estimated average number density of aerosols in the test section are about 10^{10} /m^3, 10^8/ m^3 and few, less than 0.3 μm particles size ("present in atmosphere") during pre-monsoon, monsoon, and after long duration filtration respectively. The deviation from the conduction profile for these cases are shown in Fig. 3.5 and a snapshot of the aerosols inside the test section during pre-monsoon conditions, during the monsoon and after air-filtration is shown in Fig. 3.6. In the first case, the air inside the test section is drawn from the field during the pre-monsoon season. In this case, the aerosol concentration is expected to be high due to the prevailing dry conditions. It is observed that the deviation is one-sided (positive), i.e., there is

only heating with respect to the pure conduction profile. The maximum deviation occurs around 2.4 cm from the bottom boundary and is 0.57 K. The radiative flux-divergence near the bottom boundary corresponds to a heating rate of 0.25 K/s and the vertical temperature gradient near the bottom boundary is 120 K/m. The experimental results agree well with the theoretical calculations for an assumed exponential distribution of aerosol particles; the resulting optical thickness distribution is $\hat{\alpha}(z) = 1.6 \exp(-z/0.01)+0.02$. In the second case, the air inside the test section is taken from the field during the monsoon season. In this case, the aerosol concentration is expected to be low. Fig. 3.5 shows that although the deviation is again nearly one-sided, it is only 0.21 K. The radiative-flux divergence near the bottom boundary is lower, about 0.07 K/s, with a weaker temperature gradient (60 K/m). The experimental results agree well with the theoretical calculations for an assumed exponential distribution of aerosol particles; the resulting optical thickness distribution is $\hat{\alpha}(z) = 0.5 \exp(-z/0.01)+0.02$. Finally, in the third case, the air inside the test section is filtered to remove all aerosols with the size larger than and equal to 0.3 μm. With only finer aerosols, one expects a uniform distribution of aerosols in the test section. In this case, the deviation from the conduction profile is S-shaped (symmetrical) with a maximum deviation of about ± 0.13 K. For a particular case (filtered), theoretical result has been plotted for an assumed homogeneous distribution of aerosol particle; the resulting optical thickness distribution is $\hat{\alpha}(z) = 0.02$. A similar non-linear profile has also been observed by Hutchison et.al.' 1999, where experiments were done using purified CO_2 inside the test section. However, the deviation from the conduction profile in Hutchison's experiments is much smaller (~ 0.1%).

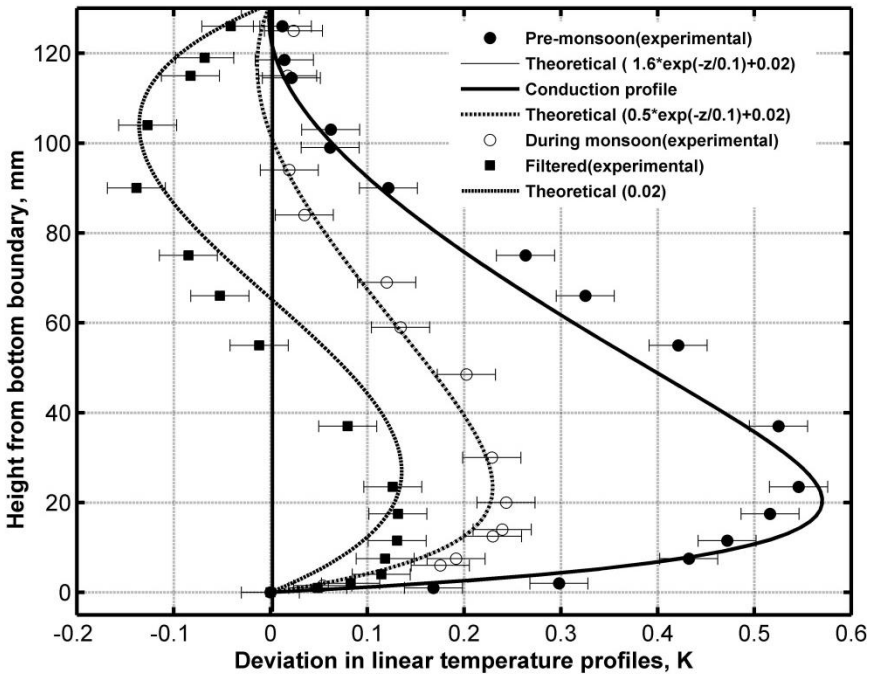

Figure 3.5 Deviation from the conduction profile with various aerosol concentrations. Solid circle, hollow circle, and solid square symbols represent pre-monsoon, during monsoon, and filtered aerosols, respectively. The lines represent theoretical results and the markers represent experiments.

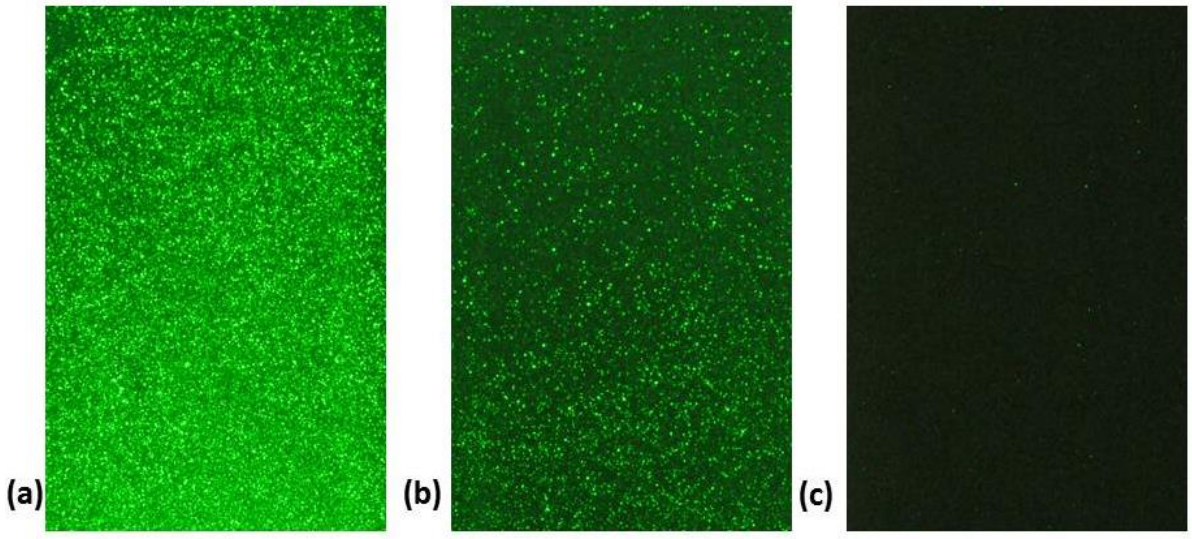

Figure 3.6 Images of lab aerosols inside the test section (a) During monsoon (b) pre-monsoon (c) after air filtration for 1 hour (particles of size < 0.3 um).

Thus, the radiative forcing in our experiments is dominated by suspended aerosols. Here the nature of the asymmetry depends the concentrated aerosol layer close to the bottom plate, as it interacts strongly with the downwelling flux from the warmer upper boundary, and hence, attains a higher temperature; this leads to a `bottom-heavy' equilibrium profile.

3.4.2 Effect of boundaries emissivity

The effect of boundary emissivity is shown in Fig. 3.7-3.10, at equilibrium. The theoretical and experimental results are compared with lines and markers respectively. In these experiments, the concentration and type of aerosols inside the test section is maintained the same as far as possible, and only the boundary emissivities are varied. The results of the experiments and theory are plotted in terms of the absolute temperature profile, deviation from the linear conduction profile, temperature gradient, and radiative flux divergence for the same aerosol distribution but with different top (ε_1) and bottom (ε_2) boundary emissivities. Experiments are done with four combinations of boundary emissivities –

(1) The bottom and top boundaries being reflective ($\varepsilon_1 = \varepsilon_2 = 0.05$), shown in Fig. 3.7;

(2) The bottom and top boundaries being black ($\varepsilon_1 = \varepsilon_2 = 0.9$), shown in Fig. 3.8;

(3) The bottom boundary being reflective ($\varepsilon_1 = 0.05$) and the top boundary being black ($\varepsilon_2 = 0.9$), shown in Fig. 3.9;

(4) The bottom boundary being black ($\varepsilon_1 = 0.9$) and the top boundary being reflective ($\varepsilon_2 = 0.05$), shown in Fig. 3.10.

The temperature of the top boundary is maintained at 4 K higher than that of the bottom boundary for all these configurations. The summary of results and the comparison between experimental and theoretical results are shown in Table 3.1. The exponential absorptivity stratification is taken as $\hat{\alpha}(z) = 1.4 \exp(-z/0.05)+0.03$. The particular functional form mimics a steeply varying concentration of large particles, combined with a uniform field of smaller particles.

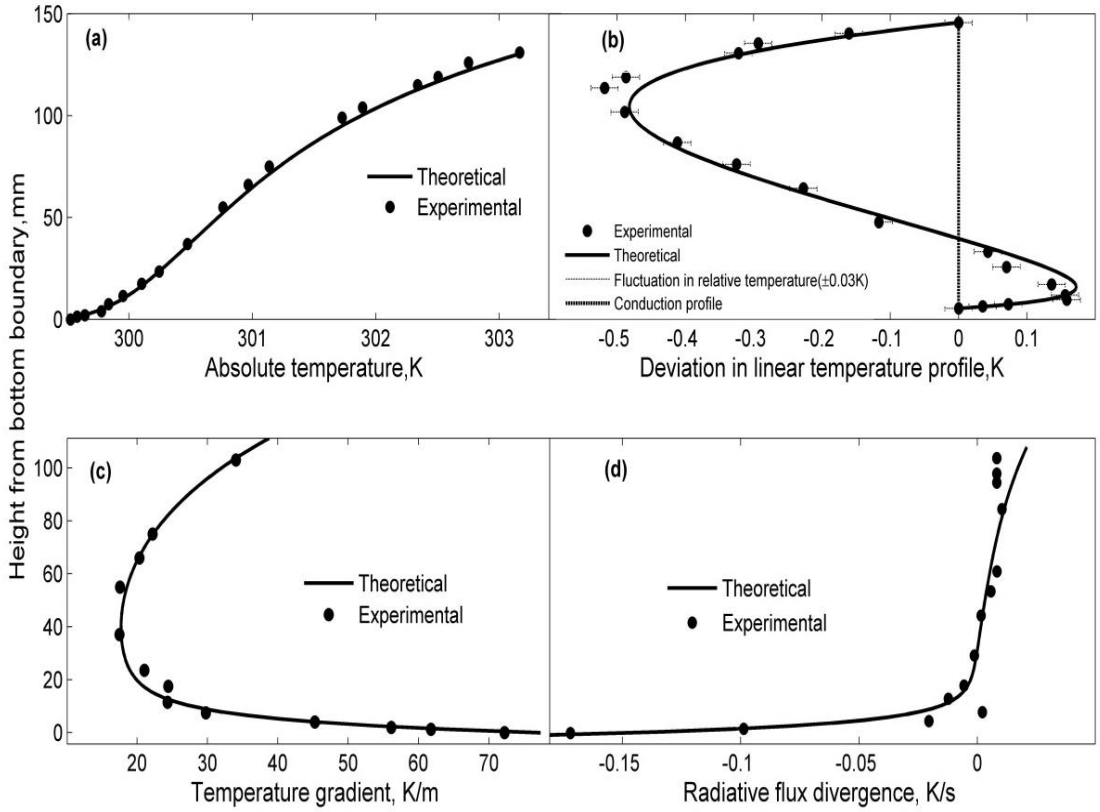

Figure 3.7 (a) Absolute temperature profile at equilibrium. (b) Deviation from the conduction profile at equilibrium. (c) Temperature gradient. (d) Radiative flux divergence with respect to height for the configuration where emissivities of both bottom and top boundaries are 0.05 (reflective). There is a good agreement between the experimental and theoretical results. The optical thickness distribution for the theoretical curves is taken as $\hat{\alpha}(z)=1.4\exp(-z/0.05)+0.03$.

In Fig. 3.7, the results are shown for the configuration where emissivities of both bottom and top boundaries being low (reflective), viz. $\boldsymbol{\varepsilon}_1 = \boldsymbol{\varepsilon}_2 = 0.05$. In such a configuration, where both the bounding surfaces have low emissivities, emission of aerosol-laden air layers dominates the boundary emission. The concentrated aerosol layer near the bottom boundary weighs the temperature profile towards lower value, leading to a top cooler profile.

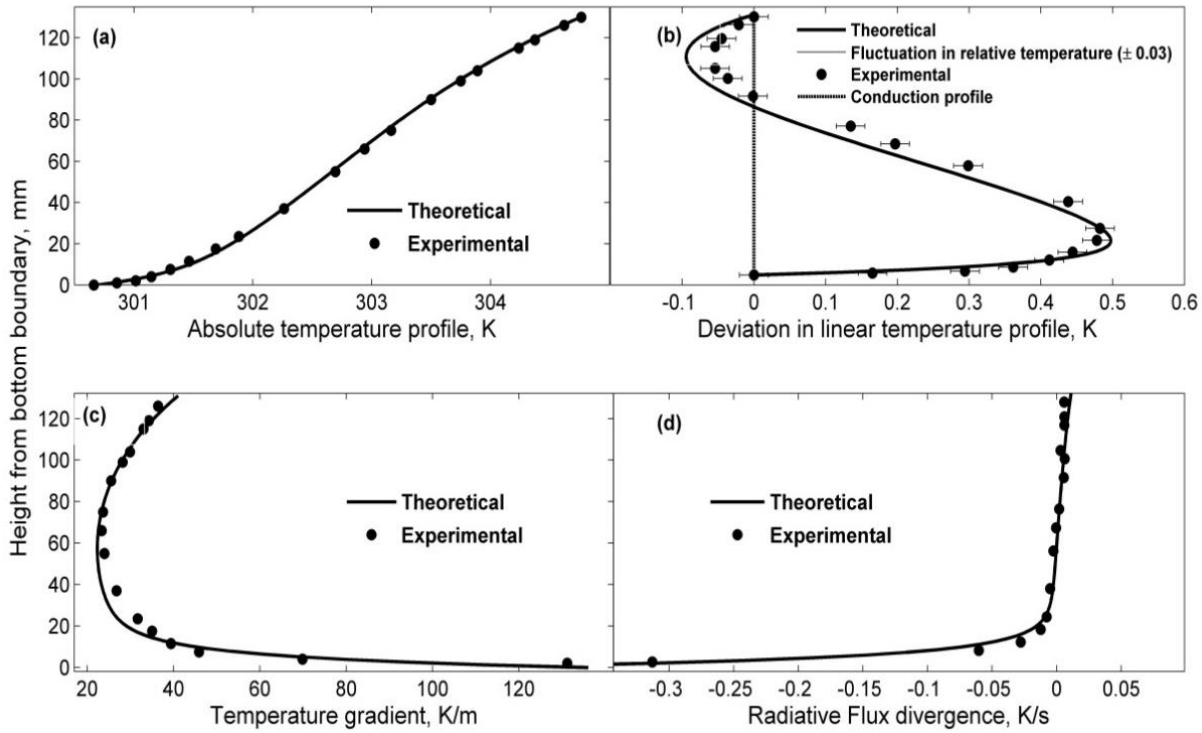

Figure 3.8 (a) Absolute temperature profile at equilibrium. (b) Deviation from the conduction profile at equilibrium. (c) Temperature gradient. (d) Radiative flux divergence with respect to height; for the configuration where emissivities of both bottom and top boundaries are 0.9 (black). There is a good agreement between the experimental and theoretical results. The optical thickness distribution for the theoretical curves is taken as $\hat{\alpha}(z) = 1.4 \exp(-z/0.05) + 0.03$.

Fig. 3.8 depicts the absolute temperature equilibrium profile, deviation from the linear conduction profile, temperature gradient, and radiative flux divergence for the configuration where emissivities of both bottom and top boundaries are high, viz. $\boldsymbol{\varepsilon}_1 = \boldsymbol{\varepsilon}_2 = 0.9$. In such a configuration, the concentrated aerosol layer close to the bottom plate interacts strongly with the downwelling flux from the warmer upper boundary and hence attains a higher temperature. This results in a 'bottom-heavy' equilibrium profile with a maximum deviation of 0.5 K with respect to the conduction profile at 20 mm.

The temperature profiles, besides deviating significantly from a linear conduction profile, also exhibit a pronounced asymmetry even when the two boundaries have identical emissivities. Any asymmetry in the corresponding homogeneous medium temperature profiles can arise only due to nonlinear effects; these are O $(\Delta T)/T_o$, and much smaller than those observed. Thus, the asymmetry predicted is solely due to the radiative effects of the inhomogeneous aerosol concentration field.

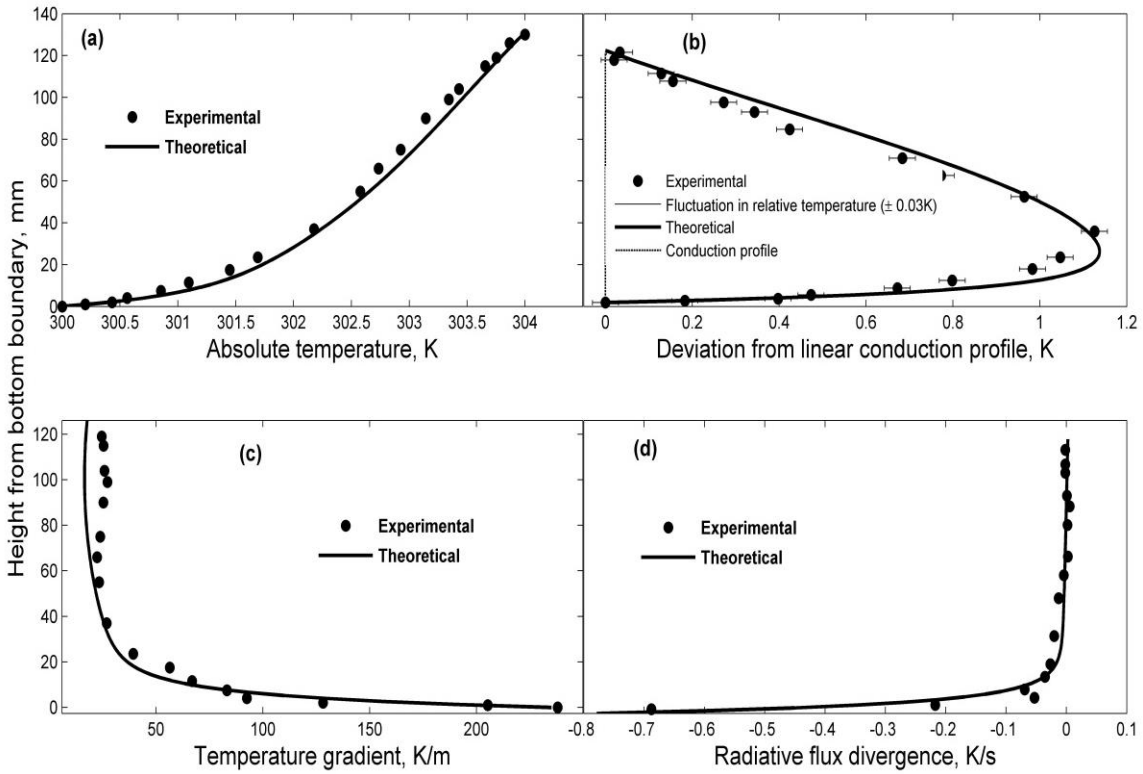

Figure 3.9 (a) Absolute temperature profile at equilibrium. (b) Deviation from the conduction profile at equilibrium. (c) Temperature gradient. (d) Radiative flux divergence with respect to height for the configuration where emissivities of bottom and top boundaries are 0.05 and 0.9, respectively. There is a good agreement between the experimental and theoretical results. The optical thickness distribution for the theoretical curves is taken as $\hat{\alpha}(z) = 1.4 \exp(-z/0.05)+0.03$.

Fig. 3.9 depicts the configuration where the bottom boundary is reflective (low emissivity ~0.05) and top boundary is black (high emissivity ~0.9), viz $\boldsymbol{\varepsilon}_1$=0.05, $\boldsymbol{\varepsilon}_2$=0.9. In such configuration, the bottom boundary has a low-emissivity; since the upwelling flux from the reflective bottom boundary is now dominated by the warmer emission originating from the upper boundary, the asymmetry for this configuration is strong enough that the deviation from the conduction profile remains positive and single-signed.

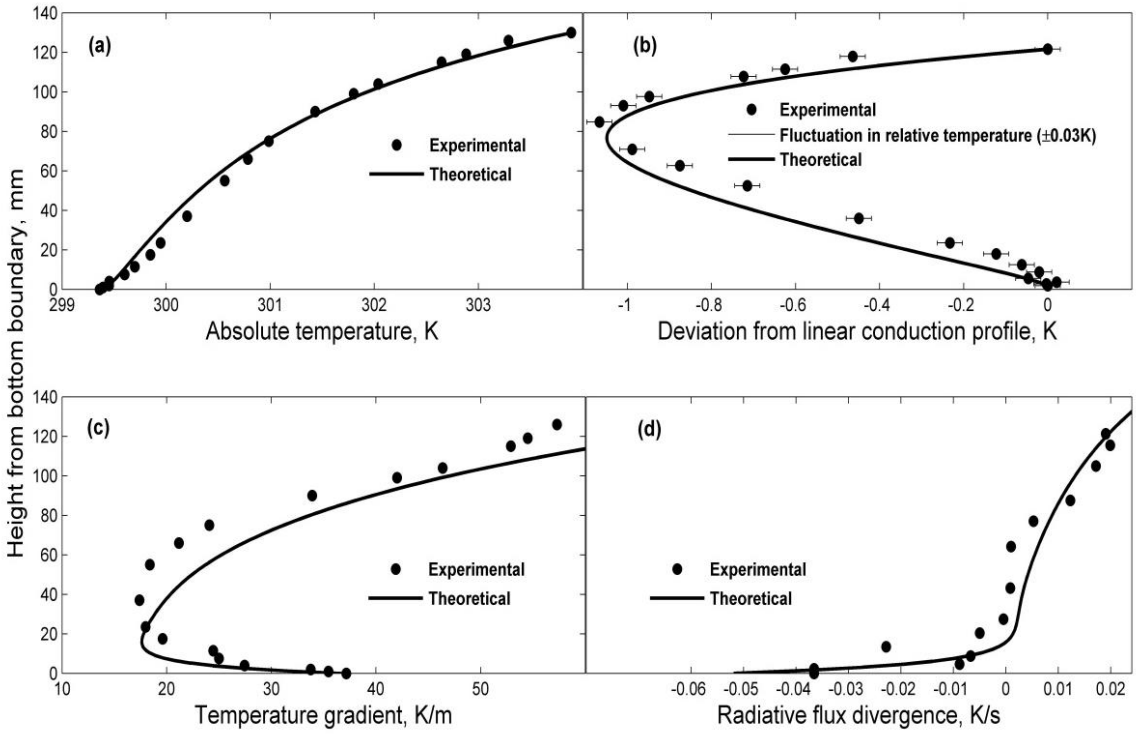

Figure 3.10 (a) Absolute temperature profile at equilibrium. (b) Deviation from the conduction profile at equilibrium. (c) Temperature gradient. (d) Radiative flux divergence with respect to height; for the configuration where emissivities of bottom and top boundaries are 0.9 and 0.05, respectively. There is a good agreement between the experimental and theoretical results. The optical thickness distribution for the theoretical curves is taken as $\hat{\alpha}(z) = 1.4 \exp(-z/0.05)+0.03$.

Fig. 3.10 depicts the results for the configuration where the bottom boundary is black (high emissivity ~ 0.9) and top boundary is reflective (low emissivity ~ 0.05), viz $\boldsymbol{\varepsilon}_1$=0.9, $\boldsymbol{\varepsilon}_2$=0.05. In such configuration, the bottom boundary has a high-emissivity; since the upwelling flux from the black bottom boundary dominates the emission originating from the upper boundary, it has a cooling effect with respect to linear conduction profile and results in single-sided deviation. The temperature gradient and radiative flux divergence are shown in Figs. 3.7-3.10. The results indicate a large temperature gradient and radiative flux divergence

near the bottom boundary and decay over the length scale O (20 mm). The largest interaction occurs for the limiting emittance condition of $\varepsilon_1 = 0.05$, $\varepsilon_2 = 0.9$ or $\varepsilon_1 = 0.9$, $\varepsilon_2 = 0.05$. These cases, of course, give the largest asymmetry in the temperature profile. Asymmetric emittance condition would be the best boundary condition for laboratory measurements from the stand-point of accentuating the interaction effects. This is the case where we set the maximum limits on the radiation interaction at the high temperature top plate and the minimum limits on the low temperature bottom plate. In this case, largest temperature gradient has been observed near the bottom boundary and it is 230 K/m. In the same case, radiation flux divergence is also largest and it is 0.7 K/s. The temperature gradient and radiative flux divergence decrease with the emissivity of the top plate, which is at higher temperature. Note that in this set of experiments, aerosol distribution for theoretical calculation is held same and only boundaries emisivities are varied to capture various observed temperature profiles.

3.4.3 Homogeneous distribution of particles: Smoke or Soot (Insence-stick)

We have further studied the case where the distribution of aerosol particles inside the test section is homogeneuos, which is achieved by filling the test section with soot particles from an incense stick. There is one orifice on the bottom plate from which soot particles enter the test section. The soot particles are lighter than aerosols. Hence, the soot particles first go upward filling the upper part of the test section and after some time the test section is completely filled with soot particles. The snapshot of the aerosol particles in the test section in this case is shown in Fig. 3.11. It can be clearly seen that the distribution of particles in this case is homogeneous.

difference between the plate is also maintained at 4 K as in the previous experiment. This experiment has been done with low emissivity bottom and top boundary ($\boldsymbol{\varepsilon}_1$=0.05, $\boldsymbol{\varepsilon}_2$=0.05). Fig. 3.12a shows the absolute temperature profile matching well with the theretical and Fig. 3.12b shows the deviation from the linear conduction profile. In this case, the deviation from linear conduction profile is symmetric (S-type) and it is ± 0.24 K. For theoretical calculations, the absorption coefficient value has been kept constant for entire test section and is $\hat{\alpha}$(z) = 0.7. Comparing these results with those above, where boundary conditions and temperature difference are exactly same with only difference in the aerosol distribution, it is clear that the profile is asymmetric (top heavy) in case of aerosols and symmetric (S-type) in case of soot. This result also supports the argument that the distribution of aerosols in the test section is heterogeneous and the distribution of soot in the test section is homogeneous.

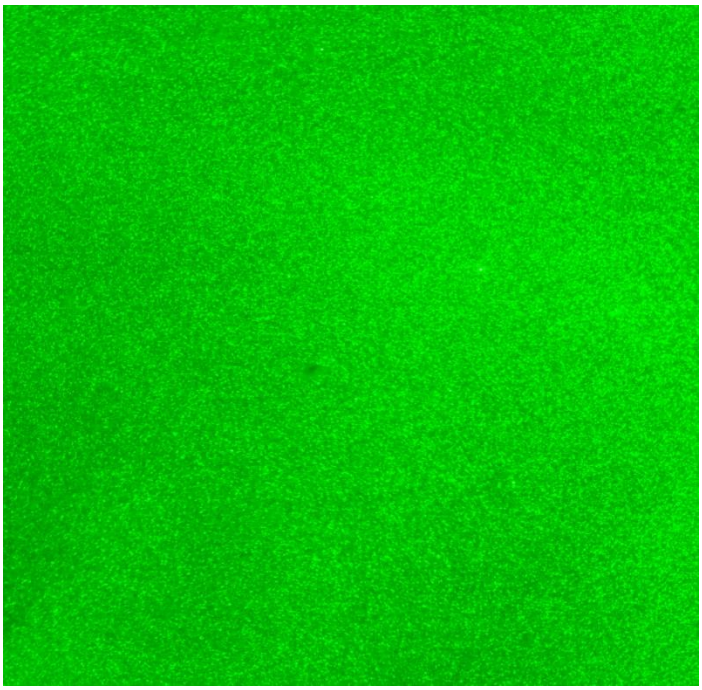

Figure 3.11 Image of soot particles inside the test section.

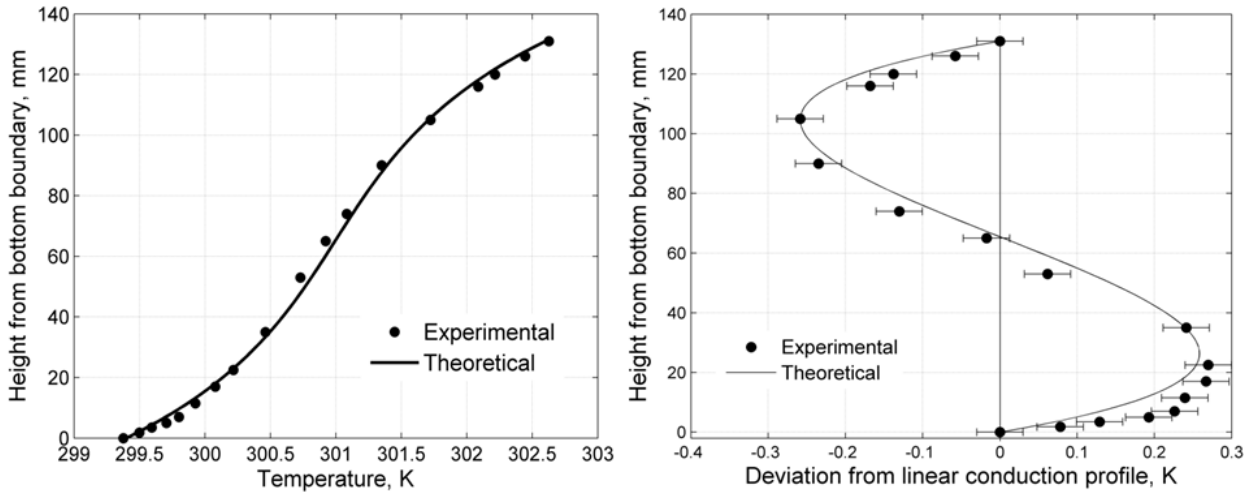

Figure 3.12 (a) Absolute temperature profile with respect to height in the test section (b) The deviation from linear conduction profile. Markers and solid lines correspond to experimental data and theoretical calculations respectively. Emissivity of bottom boundary is 0.9.

TABLE 3.1 Summary of the laboratory observations for various combinations of bottom and top boundaries in case of coupled radiation along with conduction boundary conditions (two-plate geometry).

TABLE 1: Two plate experiment						
Boundaries properties		Number of observations	Radiative flux divergence, near the bottom boundary (K/s)	Temperature gradient, near the bottom boundary (K/m)	Deviation from linear conduction profile	
Emissivity of Bottom boundary ≈	Emissivity of Top boundary ≈				Maximum Deviation in bottom side (K), height from bottom boundary (mm)	Maximum Deviation in top side (K), height from bottom boundary (mm)
0.05	0.05	5	0.17	70	0.15, 11	0.5, 90
0.9	0.9	7	0.35	135	0.5, 20	0.11, 105
0.05	0.9	3	0.7	230	1.1, 28	0
0.9	0.05	3	0.05	35	0	1.05, 90

3.5 Conclusion

Experimental observations and theoretical calculations show a significant deviation of the equilibrium profiles from the linear conduction profile due to suspended aerosols particles. In the two-plate geometry, maximum deviation from the conduction profile is observed at higher aerosol concentrations, corresponding to pre-monsoon air, and is 2.5 times greater than that for air during monsoon. A symmetric temperature profile is exhibited for air with a uniform distribution of aerosols and when top and bottom boundaries have same emissivity; while an asymmetric temperature profile is attained for the case of differing boundary emissivities and also for the case of identical boundary emissivities with an inhomogeneous aerosol distribution.

Theoretical predictions for the equilibrium temperature profiles arising in a radiatively participating heterogeneous medium sandwiched between two horizontal plates have been presented. The radiative forcing obtained here exceeds the one obtained in similar laboratory experiments, but with purified gases such as CO_2 and NH_3, by at least an order of magnitude.

The experimental observation and theoretical calculation, in case of homogeneous distribution of particle (soot particles) in the test section show symmetric temperature profile (S-type). The number density of aerosols has been estimated in the test section using laser-optics method. Our results emphasize the importance of aerosol-induced radiative forcing at laboratory length scales.

CHAPTER 4

Delay in the onset of convection in a participating medium due to radiative forcing of aerosols

4.1. Introduction

The Rayleigh-Benard instability problem for radiating fluids has gained significant attention amongst researchers due to its implications in astrophysics and geophysics and in other applications such as solar collectors. It has been previously shown that qualitatively, the onset of classical thermo convective instability is delayed by two processes (R. Goody 1956). The first stabilizing process is the decrease in the static temperature gradient in the core region of the fluid layer resulting from coupled radiation and conduction. The second process is the radiative damping of temperature perturbations. Goody considered gray media with black free boundaries and used the differential approximation for radiative transfer calculation. He solved the problem for optically thin and optically thick media using a variation principle to determine the onset of Rayleigh-Benard instability. He also applied linear stability theory to determine the critical value of the Rayleigh number in the limiting cases of transparent and opaque gray media when the horizontal boundaries were idealized as planar, stress-free surfaces. Goody noted two stabilizing effects of radiation on the onset of the Rayleigh-Benard convection. First, radiative damping tends to diminish temperature perturbations. Second, radiation causes the basic state temperature profile in the interior of the domain to have a more stable lapse rate. Later, Spiegel (1960) treated the more realistic laboratory case of rigid horizontal boundaries and arbitrary optical thickness using rigorous integral formulation of radiative transfer, but he neglected both thermal conduction and

radiation effect on the static temperature profile. Following Goody's approach, Khosla and Murgai (1963), and Murgai and Khosla (1962) included, respectively, the effects of magnetic field and the rotation which are of interest in astrophysical problems. Using a Galerkin method, Arpaci and Gozum (1973) were the first to introduce the effects of fluid non-grayness, optical thickness, the ratio of conduction to radiation and boundary emissivities. They observed the results for black-black, mirror-mirror and black-mirror boundaries. The conclusion from these previous works is that the gas radiation delays the onset of Rayleigh-Benard instability as well as of the transverse instability in differentially heated vertical cavities. Only Gille and Goody (1964) treated approximately the case of real gases using characteristic radiative times to evaluate the radiative damping effects on the instability onset. They also provided experimental critical Rayleigh number in the case of rigid boundaries, nonlinear initial temperature profiles, and non-gray radiation (where absorption depends on wavelength) by using Rayleigh-Ritz technique. These experiments also provided the maximum value of critical Rayleigh number for ammonia R_{ac} = 4870 (for air R_{ac} = 1786). Larson (1999) proposed buoyancy, velocity, and heat-flux scales for dry atmospheres in radiative-conductive equilibrium. The weakly nonlinear convective properties of their radiative-convective system differ markedly from those of weakly nonlinear Rayleigh-Benard convection. Specifically, the molecular viscosity and thermal diffusivity have little influence on the convective heat flux in the radiative-convective system, whereas they have a strong influence on weakly nonlinear Rayleigh-Benard convection. Rayleigh-Benard convection does not include thermal radiation transfer, whereas in a radiative-conductive atmosphere, radiation largely determines the basic state and also damps temperature perturbations. For the case of Rayleigh-Benard convection, many simple linear and nonlinear

stability results have been established [Drazin and Reid (1981); Joseph (1965)]. Larson (2001) derived equally simple linear and nonlinear stability properties for an idealized fluid system in which thermal radiation is added to Rayleigh-Benard convection. He obtained the non-linear stability properties of Goody's model when thermal diffusivity was set to zero and he proved that no subcritical instabilities can exist. When thermal diffusivity is non-zero, the subcritical instability cannot be ruled out, but a threshold can be found, below which the system is stable to any perturbations.

Recently, Bdeoui and Soufiani investigated, theoretically, the radiation effects on the Rayleigh-Benard instability for real gases such as NH_3, H_2O, and CO_2. They developed a procedure that enables quantitative predictions of critical Rayleigh numbers and that accounts for the complex structure of molecular absorption spectra. He showed that neither radiation effect on the static temperature profile nor the radiative damping of thermal disturbances can be neglected. Radiation effects on the delay of instability onset increase with temperature, later depth, and decrease with boundary emissivities. Gille and Goody (1964) were the first to experimentally analyze the effect of radiation on the onset of convection in a participating medium bounded by horizontal surfaces at different temperatures. Later, Novotny et al. (1970) analyzed radiative-conductive equilibria in horizontal gas layers. Novotny and Olsofka (1970) extended their efforts by examining the effect of an added non-participating gas. Neitzel (1974) showed that an energy stability theory could be applied to the Rayleigh-Benard problem in a radiative fluid. Hutchison and Richards (1999) determined the onset of thermal instability in a thin carbon dioxide layer. In all the above cases, the deviation of the base state profile from the original conduction profile

was modest. For instance, in the experiments by Gille and Goody (1964), the deviation was about 4% of the imposed temperature difference, while for Hutchison and Richards (1999), the normalised deviation was less than 0.1 %. The increase in the critical Rayleigh number found in the above studies was likewise modest; for instance, Hutchison and Richards (1999) found an enhancement of about 7-20 %.

Heat transfer processes in the nocturnal boundary layer (NBL) determine the vertical temperature profile, which in turn controls the formation of inversion layers, the occurrence of radiation fog [Mukund et al. (2010); Funk (1960)] and pollutant dispersal. It is generally argued that after sunset, the ground being a good emitter, cools radiatively to the upper atmosphere faster than the overlying air layers, leading to a stable inversion layer over the surface [Stull (1988)]. Nevertheless, Ramdas and Atmanathan (1932); Ramdas (1953) observed that the air layers just above the ground cool fastest after the sunset, resulting in an anomalous temperature-profile with the minimum temperature occurring a few decimetres above the ground. In honor of the original discoverer, the phenomenon is referred to as the Ramdas-paradox [Lettau (1979)]; the temperature profile itself has been referred to as the lifted temperature minimum (LTM). An LTM-type profile may be characterized by the height of the minimum (the LTM height) and the difference between the ground temperature and the minimum (the LTM intensity). Our recent studies on the micro-meteorological phenomenon of the Ramdas paradox or the LTM emphasize the role of the medium heterogeneity in determining the thermal structure of the nocturnal boundary layer under calm cloudless conditions [Mukund et al. (2010)]. The decoupling of radiation, convection, and conduction boundary conditions, which is essential for LTM formation is reproduced in a

laboratory set up. A near-surface concentration gradient of suspended aerosols is proposed as the cause for the preferential hyper-cooling and its existence confirmed via laboratory experiments [Mukund et al. (2013)]. The findings reinforce the importance of the participating medium's heterogeneity even on laboratory length scales, and have motivated us to examine experimentally, the role of medium heterogeneity in a simpler geometry originally used in the context of the classical Rayleigh-Benard problem - a heterogeneous participating medium sandwiched between infinite parallel plates maintained at different temperatures. For finding the critical Rayleigh number of the onset of the instability, a series of experiments across of aerosol laden near surface air layers are conducted. In these experiments, temperature profiles, temperature fluctuations, velocities, and particle flows have been measured in the quiescent air layer before and after the onset of the instability. It is found that the critical Rayleigh number for aerosol-laden near-surface air layers is significantly larger than those measured in a non-participating gas. Previously, only Gilly and Goody, and Hutchison and Richards have worked experimentally on coupled conduction-radiation problem. No experimental measurements relevant to decoupled conduction, convection, and radiation boundary condition in a radiatively participating medium have been reported. For this reason, the present work was undertaken to experimentally examine the thermal instability in a radiatively participating medium. In stable conditions, ($T_t > T_b$), the LTM-type profile [Mukund et al. (2013)] has been observed and Rayleigh numbers for various heights of the test section and boundary conditions have been considered.

In Section 4.4, the temperature profiles, velocity, temperature fluctuation, and Nusult number before and after the onset of instability in the LTM region have been discussed. In Section

4.5, the results between thermal diffusivity and radiation damping in decoupled conduction, convection, and radiation boundary conditions for same Rayleigh number and participating medium have been compared. In this section, the effect of boundary emissivity, optical depth and temperature of radiation boundary has also been studied. The effect of hotter sky on the onset of instability is discussed in section 4.6. In section 4.7, the radiation time constant of radiative participating medium (aerosols) has been estimated.

4.2 Experimental set up

The experimental apparatus used to make the temperature profile and flow visualization of aerosol laden near-surface air layers in the test section show in Fig. 4.1. A schematic of the laboratory set up and actual set up are shown in Fig. 2.3 and Fig. 2.4 respectively. Details of the experimental set up have been discussed in chapter 02.

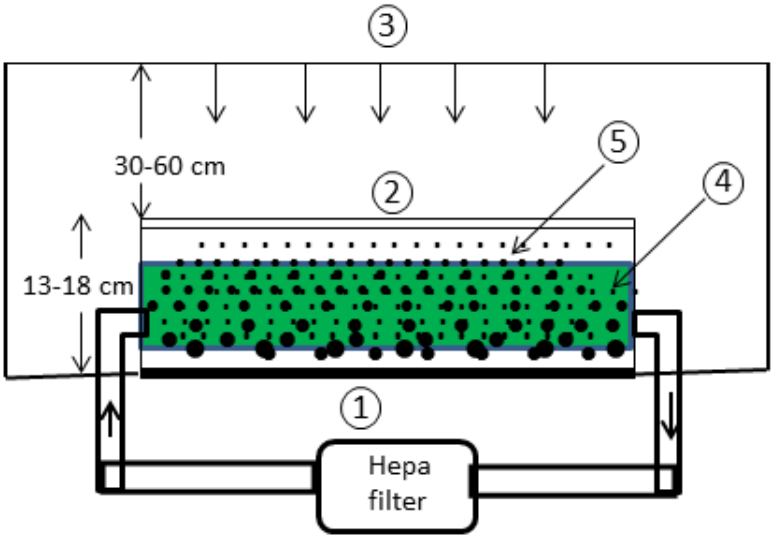

Figure 4.1 Laboratory experimental schematic in cross section showing 1, bottom aluminum plate; 2, top transparent (polythene) boundary; 3, radiation cooling boundary (Sky); 4, vertical laser-sheet in the test section; 5, aerosols hetrogeneous distribution.

Measurements were done by varying the emissivity of the boundaries of the test section either by coating them with black paint (high-emissivity surface) or by covering them with a highly polished aluminum sheet (low-emissivity surface). The experimental set up consists of a traverse arrangement on which a portable Mini-LDV system (Measurement science Enterprises, Pasadena, CA, USA) has been mounted for monitoring the aerosols' speed, a vertical laser sheet obtained by using a 500 mW continuous green laser and a Nikon-D90 digital camera for capturing aerosols. The thickness of the light sheet is about 2.5 mm; the Mini-LDV system records velocity at various heights in the test section and is capable of measuring velocity with naturally occurring aerosols in the air (of size 1 μm ≈ or larger). A schematic diagram depicting the imaging of aerosols is shown in Fig. 4.2.

4.3 Data processing

We have considered non-averaged temperature data for vertical temperature profile in the test section and averaged temperature data for temperature gradient and cooling rate. These details have been given in Chapter 02 in the data processing section. The error in measuring the velocity by using LDV is ± 1 mm/s.

4.4 Onset of instability in the LTM-type profiles

In the LTM region for radiative participating medium, the Rayleigh number (Ra), critical Rayleigh number (Ra_c), temperature fluctuation, and velocity are the parameters determining the heat transfer. The Rayleigh number (based on diffusivity) is defined by the following equation:

$$Ra = g \beta (\Delta T) d^3/\nu\alpha \qquad (4.1)$$

where, ΔT is intensity of minimum and d is height of the minimum, ν (kinematics viscosity) = 1.9 X 10^{-5} and α (thermal diffusivity) = 1.4 X 10^{-5}, β (thermal expansion coefficient) = 1/300 K at 1 atm. Following Goody [Goody (1964)], the effective critical Rayleigh number $Ra_{(eff)}$ is given by:

$$Rac_{(eff)} = Ra_{c(diff)} \text{ X } S_\beta \text{ X } S_H \qquad (4.2)$$

where $Ra_{c(diff)}$ is O(1000) for rigid- free boundaries, S_β = ratio of temperature gradient given by: $S_\beta = T_z/\overline{T_z}$, T_z= ΔT/d and $\overline{T_z} = \frac{dT}{dz}\Big| z = d/2$. A detail of gradient is shown in Fig. 4.2.

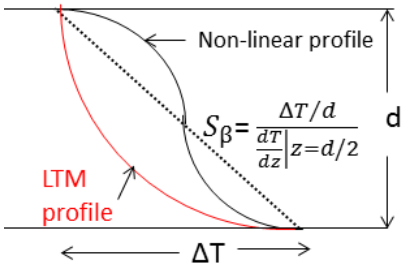

Figure 4.2 Schematic of non-linear temperature profile [Goody (1964)] and LTM profile.

In our case, the radiation and diffusion act together and then the time constant of the system is given by $t_{eff}^{-1} = t_{rad}^{-1} + t_{diff}^{-1}$ (4.3) [Gille and Goody (1964)]

$$\text{and therefore, } S_H = 1 + t_{diff}^{-1}/t_{rad}^{-1} \qquad (4.4)$$

where, t_{diff} = d^2/α, and t_{rad} = 25 s. t_{rad} (determine from experiments) is discussed in details in section 2.5.7 in chapter 02.

In section 2.5.1 in chapter 2, we show that now LTM profiles are reproduced in the laboratory and demonstrated that heterogeneous distribution of aerosols in the test section is essential for the formation of LTM-type profiles. In the laboratory, the intensity and height of minimum depend on height of the test section, emissivity of the bottom boundary, aerosols number density, and temperatures of top and radiation boundaries. Several experiments have been done with various heights of the test section and with low (0.05) and high (0.9) emissivities of bottom boundary. In this chapter, the results for the height 130 mm and 170 mm of the test section with low emissivity bottom boundary are presented. The values of Rayleigh number have been estimated for various heights of the test section and also by altering the boundary conditions. For calculation of Rayleigh number, the temperature difference corresponds to the intensity of minimum and the depth of layer corresponds to the height of minimum. Measurements of velocity and temperature fluctuation across the aerosol-laden air in the test section are presented and are used to identify the onset of instability and determine the critical Rayleigh number for radiative participating medium with atmospheric aerosols.

The temperature profile with respect to the height in the test section is shown in Fig. 4.3a, where height of the test section is 130 mm. Emissivity of the bottom boundary is 0.05±0.02. The intensity of the minimum is 0.91±0.03 K and height of minimum is 26±2 mm. The temperature gradient and cooling rate near the bottom boundary are 210 K/m and 0.6 K/s respectively. The calculated Rayleigh number (Ra) for this layer is 2000±525, which is greater than the classical Rayleigh number ($Rac_{(eff)}$). Despite the higher value of Rayleigh number for this layer, we did not observe the onset of convection.

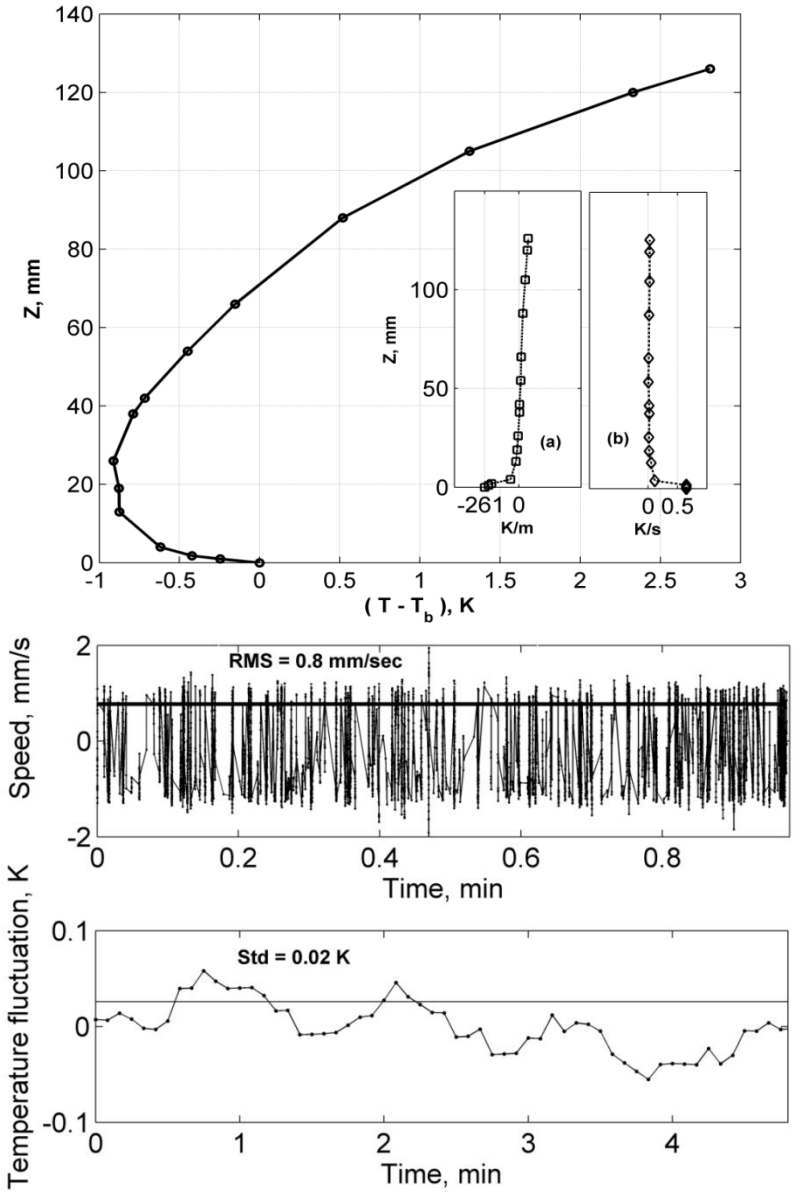

Figure 4.3 (a) Temperature profile with respect to height in the test section at steady state. The temperature of bottom and radiation boundary is 300 K and 280 K respectively. Emissivity of bottom boundary is 0.05. In the inset, the corresponding temperature gradient and cooling rate have been plotted (b) RMS vertical velocity and temperature fluctuation in the LTM-region.

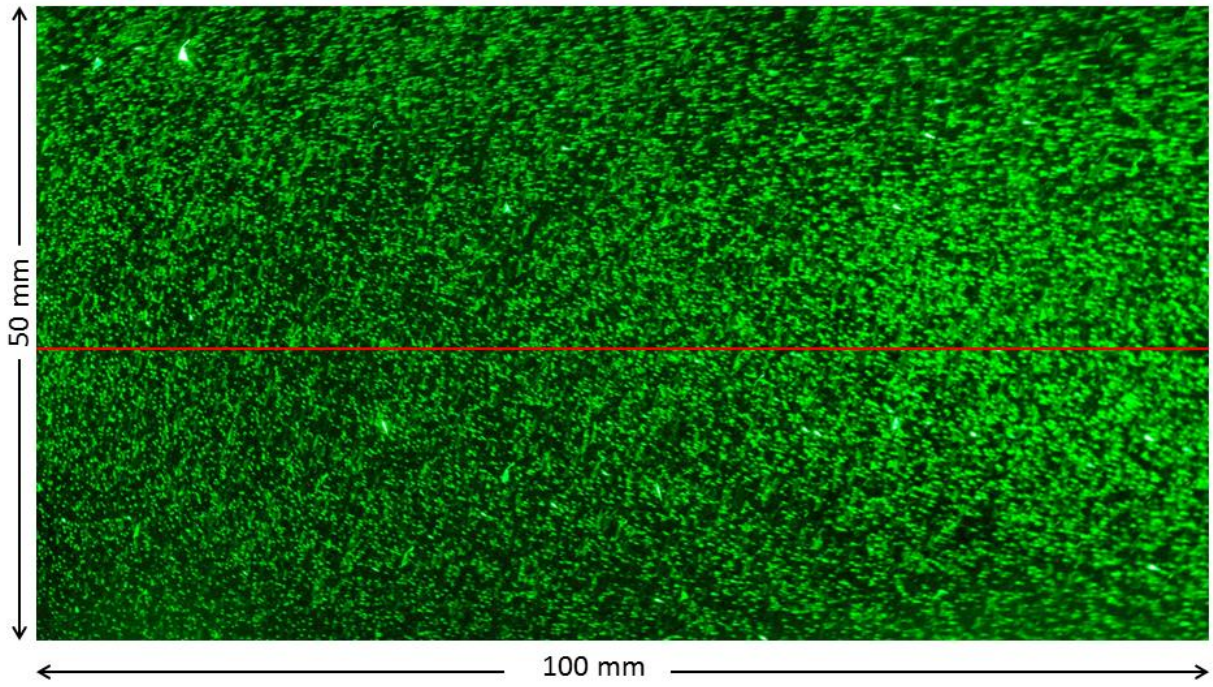

Figure 4.3 (c) Vertical cross section image of aerosol-laden air in the test section at 10 mm to 60 mm from the bottom boundary. Camera setting: t F/11 and exposure time is 1 s. Image area is 50 mm X 100 mm, the light sheet is 2.5 mm thick. The red line indicates height of minima.

In this case, average rms vertical velocity in the test section is found to be uniform with a value of 0.8 mm/s and the average temperature fluctuation is ± 0.02 K. The estimated critical Rayleigh number ($Rac_{(eff)}$) for this case, using Eq. (4.2) is 6784±1782; it is greater than the observed Rayleigh number, and supports the absence of convection in this case.

In figure (4.3b, 4.3c) aerosols images, measured vertical velocity of the particles, and temperature fluctuations in the test section during the experiment at steady state have been presented. The red solid line indicates the height of minimum (where minimum temperature occurred). The Rayleigh number estimated is 2000 for the region below the red line. In this region, no appropriate motion of particles was observed throughout the experiment. The vertical velocity of the particles is observed to be uniform throughout the section and is about

~ mm/s. In a variation of the same experiment where the height of the test section is 130 mm, the aerosols number density was maintained at the same level, but the temperature of the top boundary was reduced. In such a case, the intensity of minima is found to be 1.18±0.03 K, height of minima is 38±2 mm, and calculated Rayleigh number for this layer is 8000±1464. The estimated $Rac_{(eff)}$ for this case, using Eq. (4.2) is 11481±2102, is close to the observed Rayleigh number. The temperature profile for this case is shown in Fig. 4.4a and the corresponding aerosols image, measured velocity of the particles, and temperature fluctuation in the test section during the experiment at steady state are shown in fig. 4.4b, 4.4c. The velocity of particles below and above the red line was found to be different, the average rms velocity of particles below the red line was 11.2 mm/s, and that of above the line was around 1 mm/s. As can be seen in Fig. 4.4, a weak convection has been obtained in the LTM region (below red line) and the fluctuation in temperature is higher than the previous cases. In case 2, the height of the test section was increased to 170 mm. In such a case, the intensity of minimum and height of minimum are 0.91±0.03 K and 39±2 mm respectively. The calculated Rayleigh number for this layer is 6628±1193 and the estimated $Rac_{(eff)}$ for this case is 11513±2072, which is greater than the observed Rayleigh number. The temperature profile for this test section is shown in Fig. 4.5a, and the corresponding aerosols image, measured velocity of the particles, and temperature fluctuation in the test section during the experiment at steady state are shown in Fig. 4.5b,c. In this case again, no appropriate motion was observed and the velocity of the particles was observed to be approximately same (0.85 mm/s) throughout the test section. In a variation of the same experiment where the height of the test section is 170 mm, the temperature of the top boundary was reduced and the rest of the conditions were kept same.

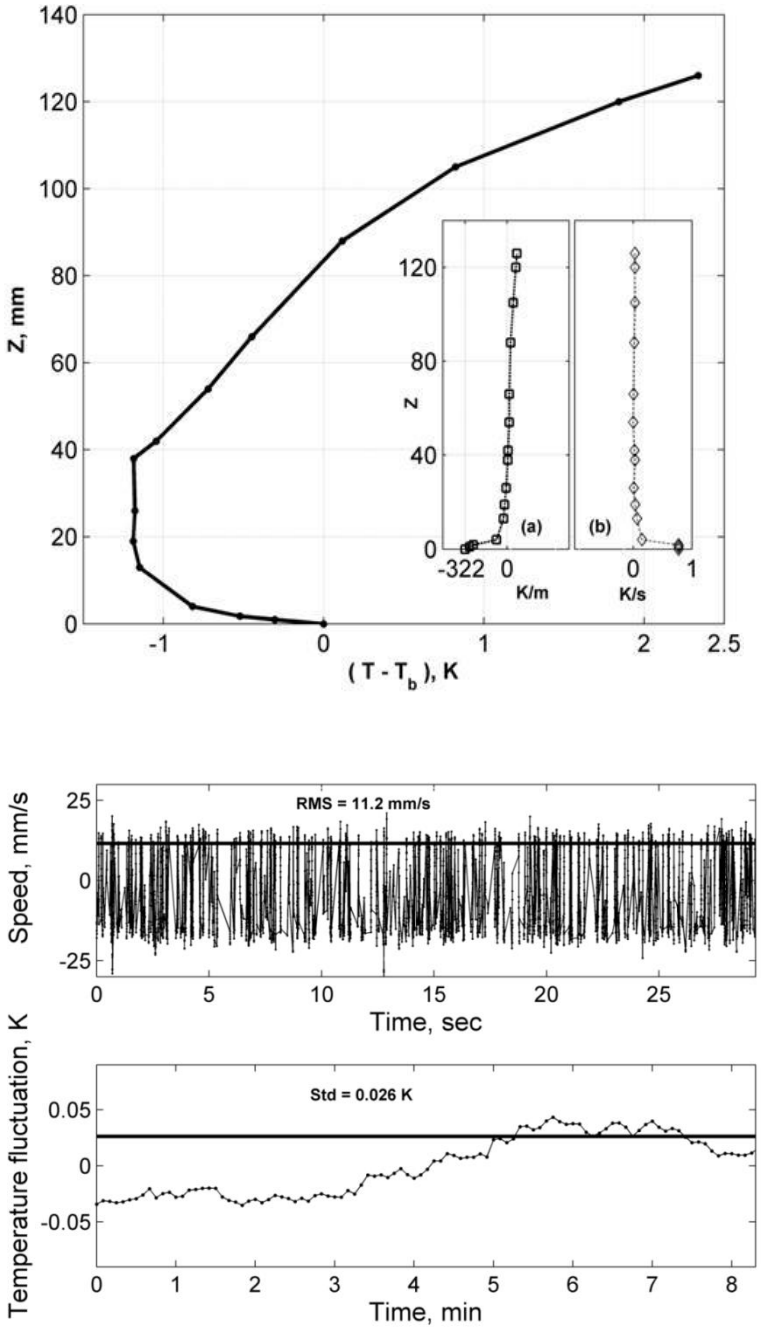

Figure 4.4. (a) Temperature profile with respect to height in the test section. Temperature of bottom and radiation boundary is 300 K and 280 K respectively. Emissivity of bottom boundary is 0.05. In the inset, the corresponding temperature gradient and cooling rate have been plotted (b) RMS vertical Velocity and temperature fluctuation in the LTM-region.

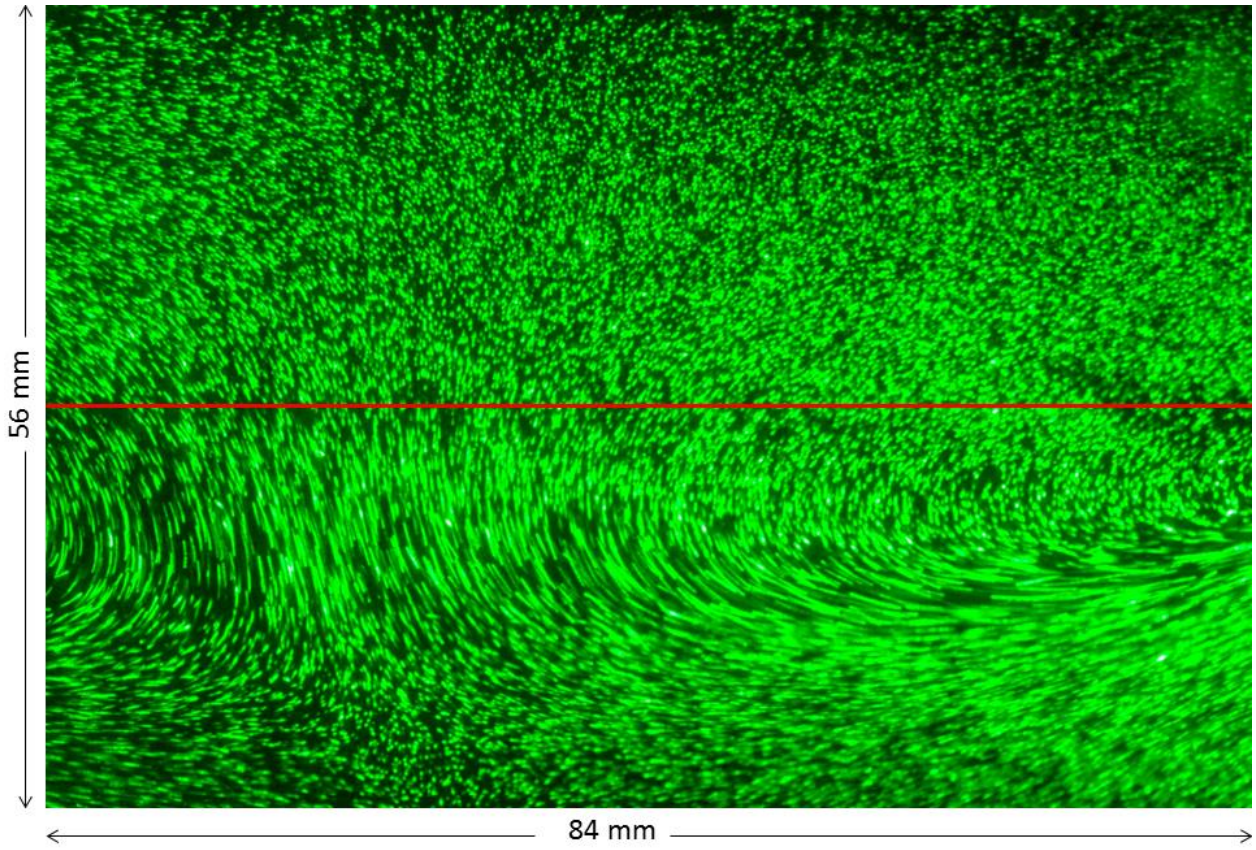

Figure 4.4 (c) Vertical cross section image of aerosol laden air in the test section at 10 mm to 66 mm from the bottom boundary. Camera setting: t F/11 and exposure time is 1 s. Image area is 56 mm X 84 mm, the light sheet is 2.5 mm thick. The red line indicates height of minima.

In such case, the intensity of minimum and height of minimum were 1.5±0.03 K and 43±2 mm respectively. Calculated Rayleigh number for this layer is 14645±2336 and the estimated $Rac_{(eff)}$ for this case is 12246±1959, which is less than the observed Rayleigh number. The temperature profile for this case is shown in Fig. 4.6a, and the corresponding aerosols image, measured velocity of the particles, and temperature fluctuation in the test section during the experiment at steady state are shown in Fig. 4.6b,c. The velocity of particles below and above the red line was found to be quite different in this case; the average velocity of particles was more than the previous case with the value below the red line is 17 mm/s and that for particles above the line was around 1.5 mm/s.

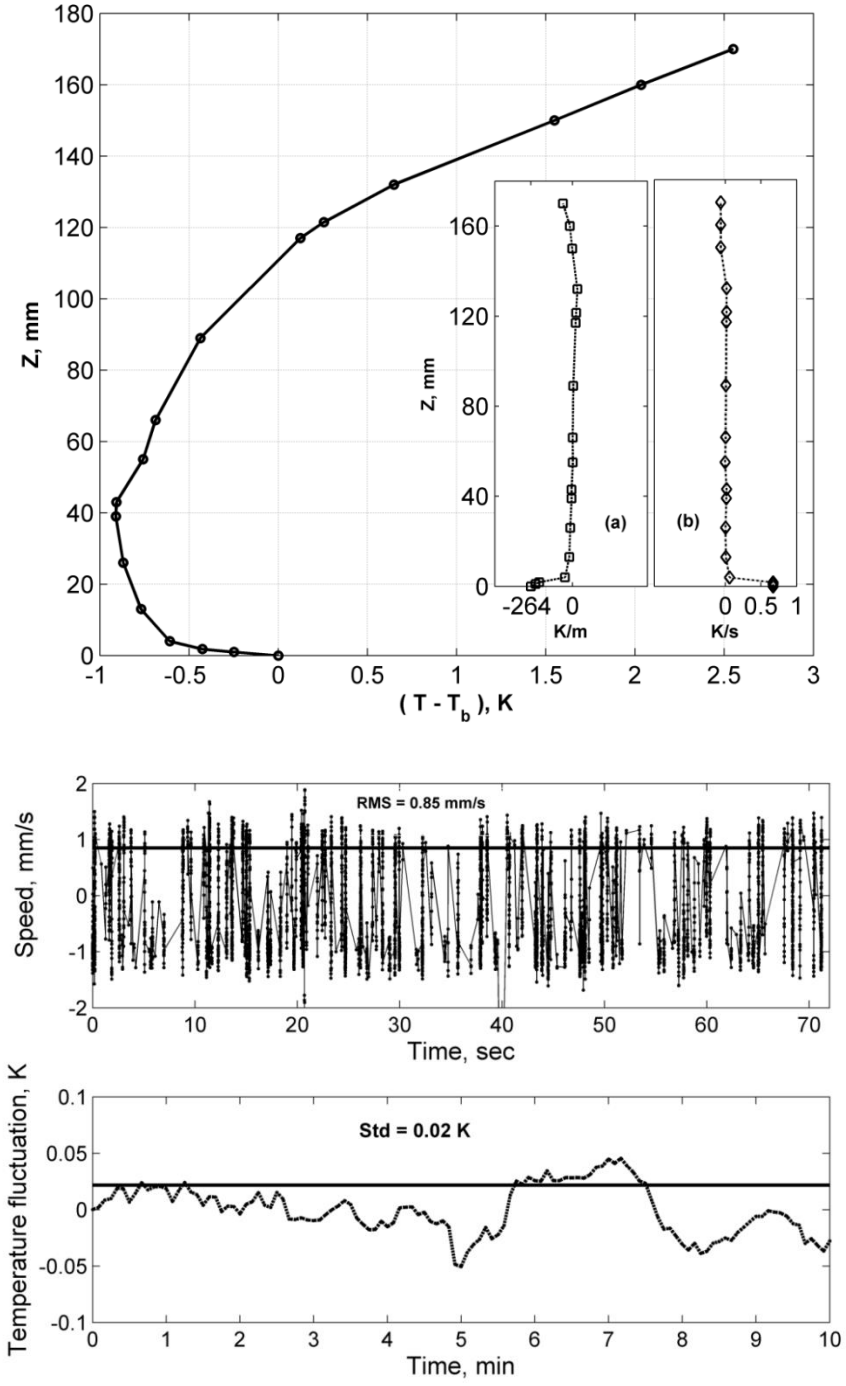

Figure 4.5. (a) Temperature profile with respect to height in the test section. Temperature of bottom and radiation boundary is 300 K and 280 K respectively. Emissivity of bottom boundary is 0.05. In the inset, the corresponding temperature gradient and cooling rate have been plotted (b) RMS vertical Velocity and temperature fluctuation in the LTM-region.

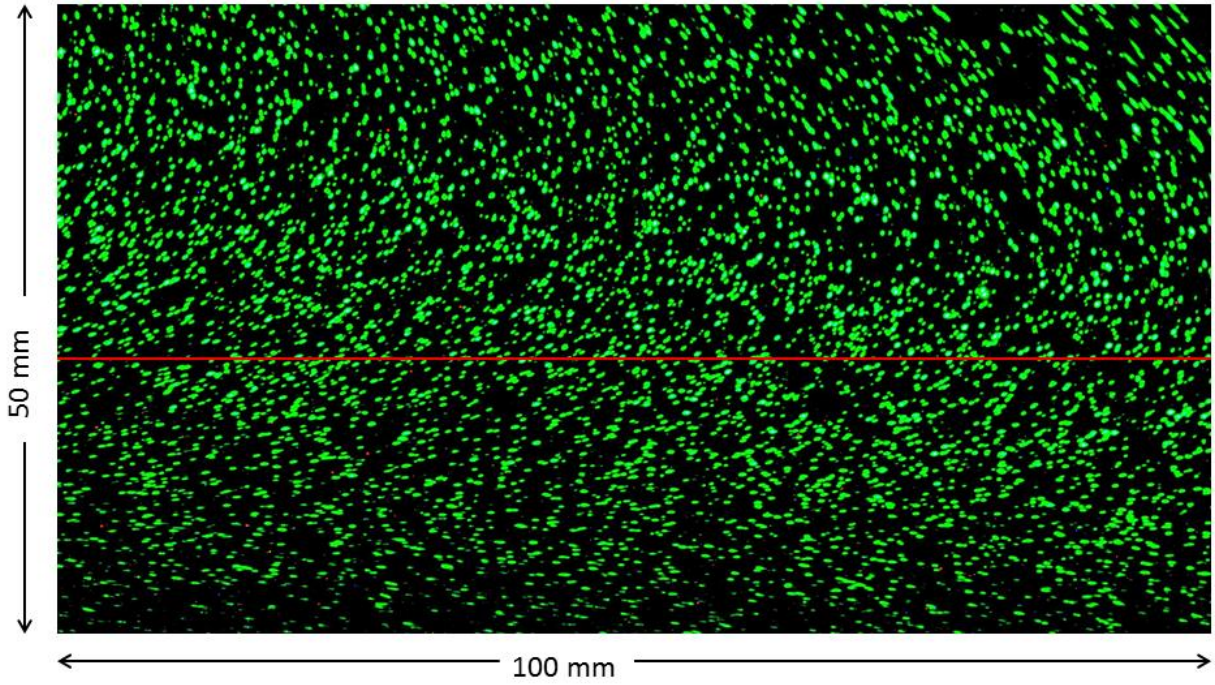

Figure 4.5 (c) Vertical cross section image of aerosol-laden air in the test section at 10 mm to 60 mm from bottom boundary. Camera setting: t F/9 and exposure time is 1 s. Image area is 50 mm X 100 mm, the light sheet is 2.5 mm thick. The red line indicates height of minima.

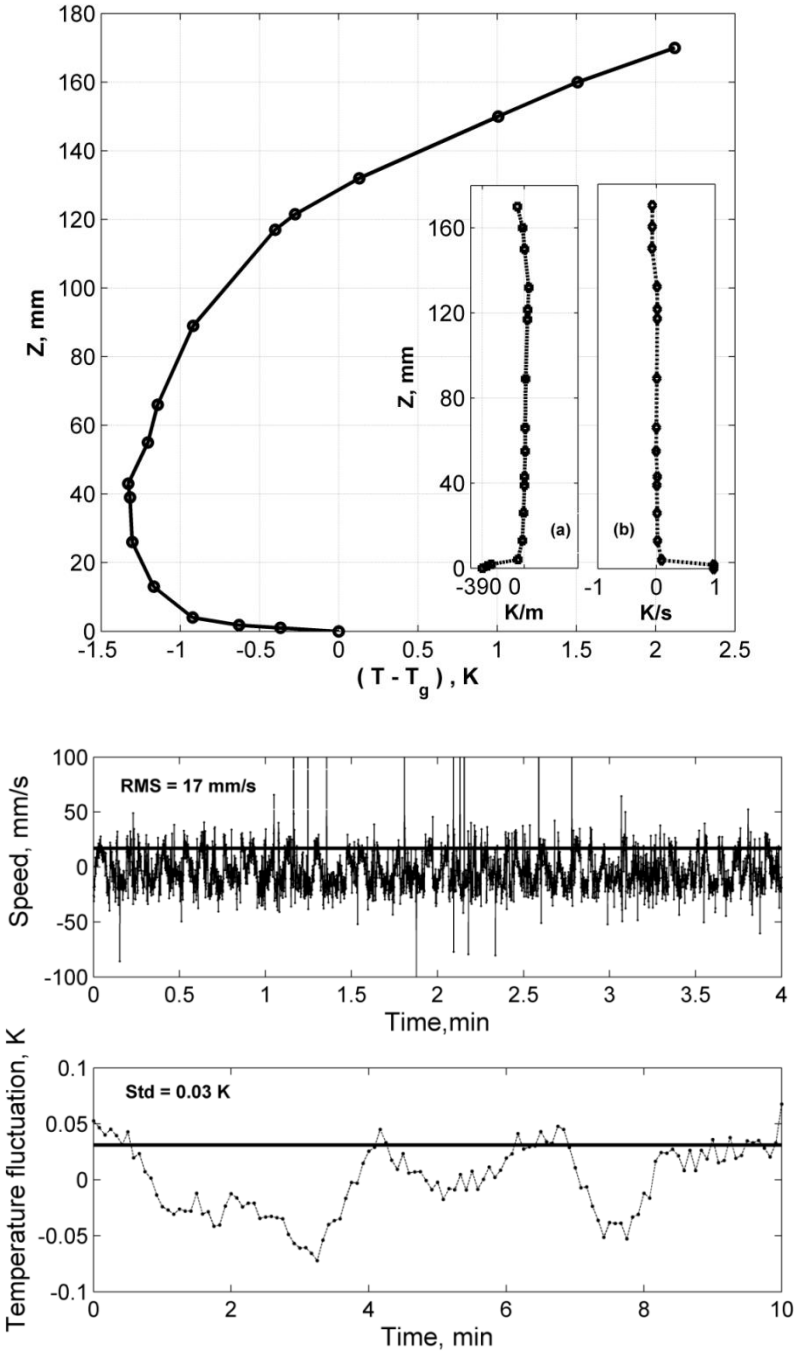

Figure 4.6. (a) Temperature profile with respect to height in the test section. Temperature of bottom and radiation boundary is 300 K and 280 K respectively. Emissivity of bottom boundary is 0.05. In the inset, the corresponding temperature gradient and cooling rate have been plotted (b) RMS vertical Velocity and temperature fluctuation in the LTM-region.

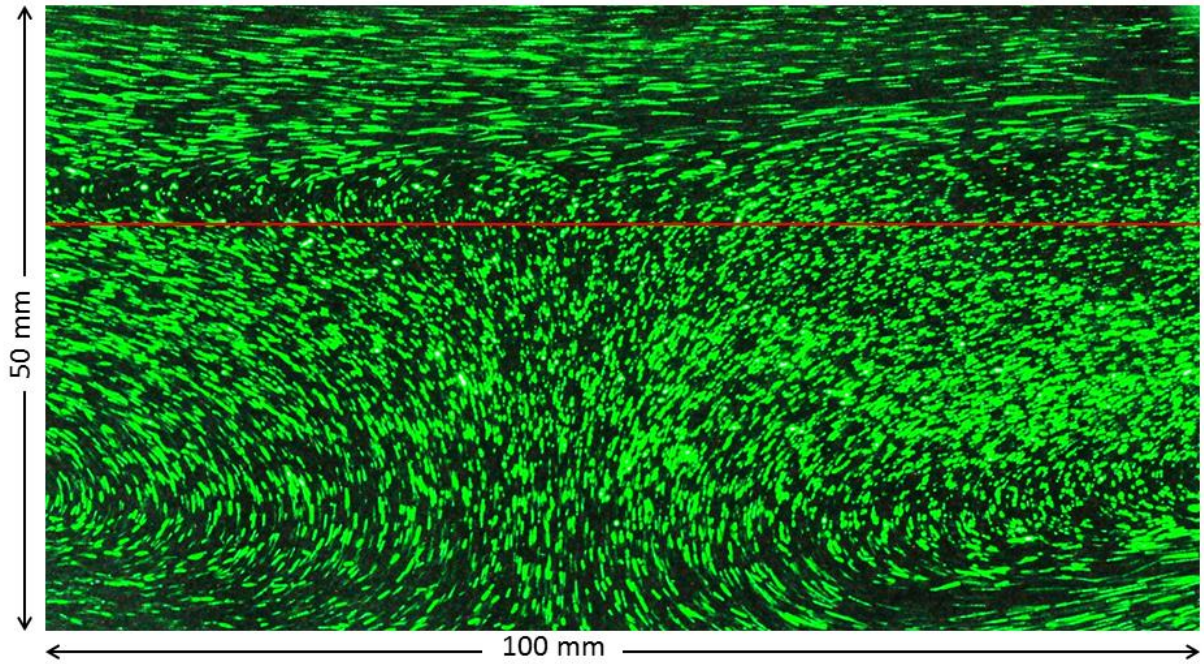

Figure 4.6 (c) Vertical cross section image of aerosol-laden air in the test section at 10 mm to 60 mm from bottom boundary. Camera setting: t F/11 and exposure time is 1 s. Image area is 50 mm X 100 mm, the light sheet is 2.5 mm thick. The red line indicates height of minima.

As can be seen, convection occurs only in the LTM-region and above LTM-region, horizontal motion with very low vertical velocity is observed. The fluctuation in temperature in the LTM region is much higher than the previous case.

For all the above cases, the maximum Rayleigh number observed is about 7000, below which convection is not observed throughout the test section. Also, it can be noticed that with increasing number of aerosols, critical Rayleigh number also increases. Similar effect has been previously shown (F. Bdeoui and A. Soufiani (1997)) that increasing the layer depth increases optical path and the radiative stabilization effect as well. Our results show that the temperature gradient and cooling rate near the bottom boundary depend on the intensity of

the minimum and the height of the minimum. The details of these experimental results are summarized in Table 4.1 and Table 4.2.

Table 4.1 Details of experimental results are summarized in this table. ε_b and ε_{Sky} are the emissivity of the bottom and the cooling source (Sky) respectively. dT/dz and dt/dt are the temperature gradient and cooling rate near the bottom boundary respectively. V_L and V_U are the rms vertical velocity below and above the LTM-region (red-line) respectively. T_{Sky} and H are the temperature of radiation boundary (Sky) and height of the test section respectively.

Case	ε_b	ε_{Sky}	-ΔT (K)	d (mm)	$dT/dz\|_{z\to 0}$ (K/m)	$dT/dt\|_{z\to 0}$ (K/s)	V_L (mm/s)	V_U (mm/s)	T_{Sky} (K)	H (mm)
1	0.05	0.9	0.91	26	-261	0.65	0.8	0.8	280	130
2	0.05	0.9	1.18	38	-322	0.77	11	1.0	280	130
3	0.05	0.9	0.91	39	-264	0.67	0.85	0.85	280	170
4	0.05	0.9	1.5	43	-390	1.0	17	1.5	280	170

Table 4.2. Details of experimental results are summarized in this table.

-ΔT (K)	d (mm)	Ra (observed)	$Rac_{(eff)}$	S_β	S_H	$S_\beta S_H$
0.91	26	2000 ± 525	6784 ± 1782	2.8	2.42	6.77
1.18	38	8000 ± 1464	11481 ± 2102	2.84	4.04	11.47
0.91	39	6628 ± 1193	11513 ± 2072	2.74	4.2	11.5
1.5	43	14645 ± 2336	12246 ± 1959	2.5	4.89	12.24

4.5 Effect of aerosol concentration on the onset of convection

The experimental measurements of radiation effects on two different aerosol concentration in the radiative participating medium, keeping the boundary conditions same in both cases, have been compared. The temperature difference between the bottom plate (T_b), polythene sheet (T_t) and T_{Sky} are maintained. In this case, air layers in the test section including boundaries can radiatively interact with the sky. At steady state, T_b =300 K, T_t = 296 K, T_{Sky} = 280 K, h (height of the test section) = 130 mm and ε_b = 0.05.

Calculated Rayleigh number for this layer is

$$Ra = (g\beta\,(\Delta T)h^3)/\nu\alpha$$

$$= 1.07 \text{ X } 10^6$$

Calculated optical thickness across aerosols air laden layers is 1.3 $X10^{-2}$ (τ_1) and thermal diffusivity coefficient is 1.9 X 10^{-5} m^2/s (k). An arrangement was made to remove the aerosol particles from the air in the test section by continuously sucking out the air from the test section and readmitting it after having passed through an HEPA-filter that removes particles with sizes greater than 0.3 μm. In addition, to capture images of the aerosol particles in the test section, a 2.5 mm thick light sheet from an Nd-Yag pulsed laser was used to illuminate a vertical plane close to the center of the test section. Images covering ~ 55 % of the height of the test section (from 1 cm to 8 cm above the bottom boundary) were captured using a Nikon D-90 digital camera. Initially, before any filtration, an experiment was performed to obtain vertical temperature profile, vertical velocity and image of aerosols (aerosol number density) in the test section. Next, the filtering was carried out for a fixed amount of time (20 minutes)

and the system was allowed to settle thereafter for about 2 hours so as to-establish a new 'quasi steady state' concentration profile. The temperature profile is then measured with the same T_{sky}, with T_b and T_t values as before. After 20 minutes of filtration, the estimated optical thickness across the test section is approximately 10^{-5} (τ_2). Figure 4.7a shows the vertical temperature profiles with temperature fluctuation in the test section before and after filtering. The temperature slip (discontinuities) near the bottom boundary (at 1 mm) before filtering is 2.5 times greater than that after filtering. The time evolution of the raw-temperature traces (without the window-averaging), at various heights, before and after removing the aerosols are shown in Fig. 4.8a.

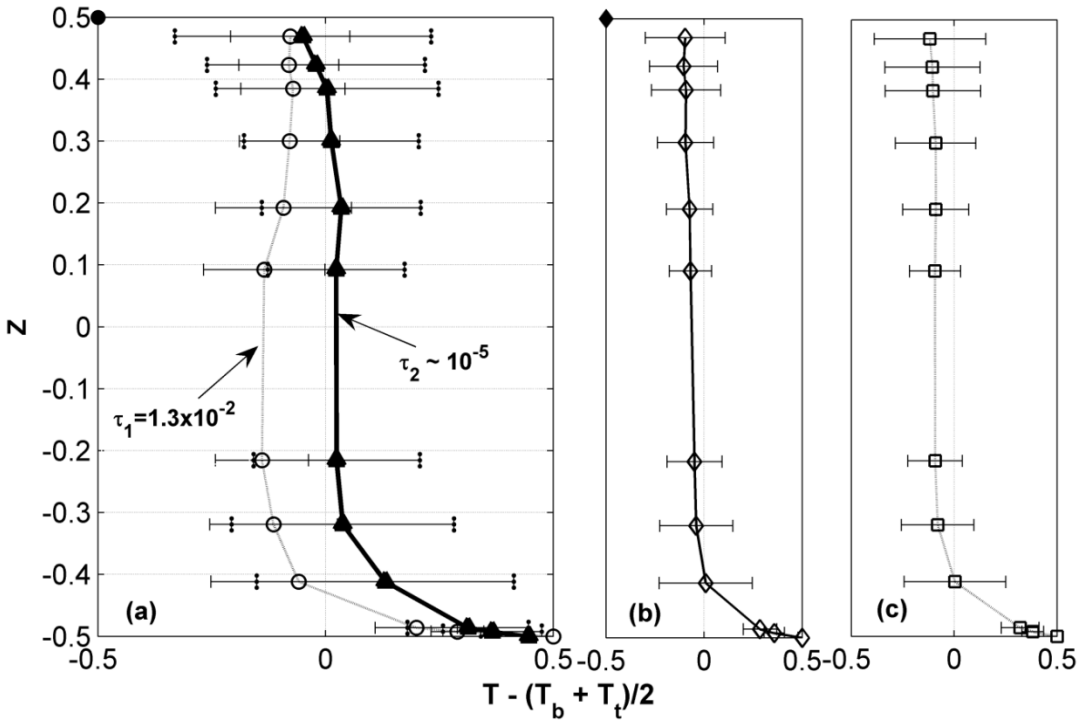

Figure 4.7 Shifted basic state temperature profiles T- (Tb + Tt)/2 vs z for various condition with same Rayleigh number (a) for τ_1=1.3 X 10^{-2} (hallow marker line), and $\tau_2 \sim 10^{-5}$ (solid marker line) (b) RBC profile in the test section where emissivity of bottom and top boundary

are 0.05 and 0.9 respectively. (c) RBC profile in the test section where emissivity of bottom and top boundaries are 0.05 and 0.05 respectively.

In previous theoretical studies (Larson (2001)), the parameters (k) and (τ) have been varied while keeping one constant at a time. In these studies, it has been shown that for the case where k → 0 (purely radiative damping), the temperature slip near the plate is maximum and decreases with increasing k. Similarly in our case, before filtering the aerosols, $k/\tau << 1$ and radiative damping dominates the thermal diffusivity, resulting in a maximum temperature slip near the bottom boundary. After filtering the aerosols, $k/\tau \sim 1$; in this case, thermal diffusivity dominates radiative damping.

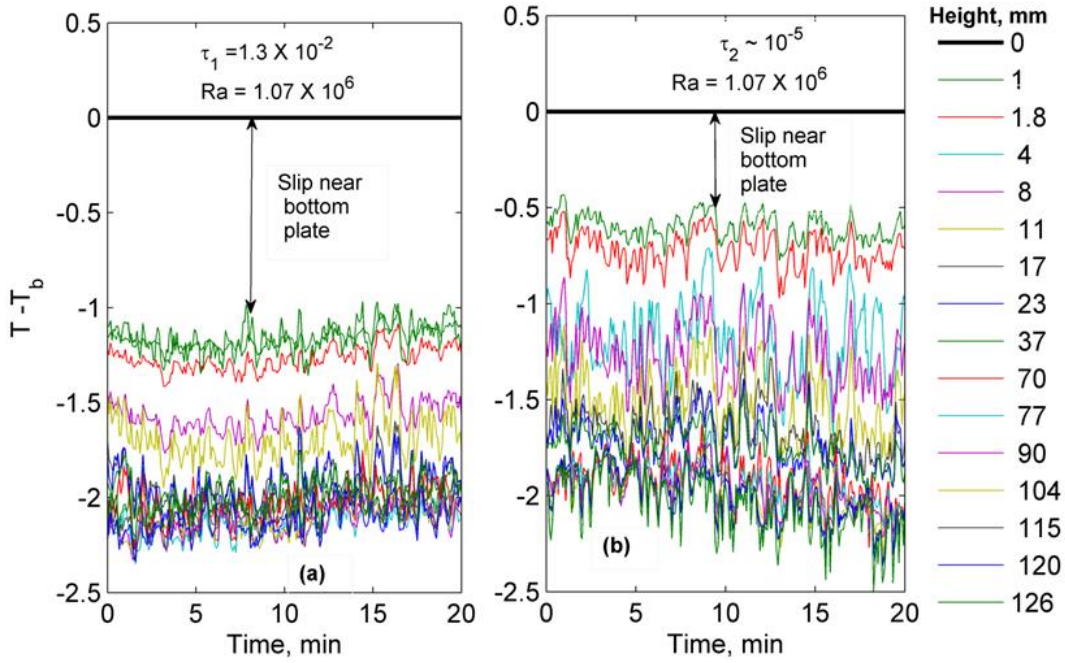

Figure 4.8 (a) Temperature traces in the test section plotted with respect to the bottom plate at various vertical locations in case of τ_1 and τ_2. The emissivity of boundaries is *0.05*. Calculated Rayleigh number is about 10^6 for both cases; slip near the bottom plate is 1 K and 0.4 K for the case τ_1 and τ_2 respectively.

Hence, the temperature slip near the plate is minimum and the temperature profile tends to the profile of RBC. Further, after filtering, temperature fluctuation and average particle velocity in the test section is 1.5 times greater than those before filtering. The average rms vertical velocities in the test section are 2.33 cm/s and 4.42 cm/s before and after the filtering of aerosols, respectively and are plotted in Fig. 4.11. As discussed in the last section, the critical Rayleigh number increases with increasing optical depth. After filtering the aerosols, the optical depth reduces and tends to become a non-radiative participating medium (air), therefore the critical Rayleigh number is decreased. The same Rayleigh number is maintained before and after filtration. The decrease in temperature gradient and cooling rate near the bottom boundary upon filtration is shown in Fig. 4.9 and Fig. 4.10. The velocity and temperature fluctuations are high after filtration, as shown in Fig. 4.11a and Fig. 4.11b, respectively. The temperature fluctuation is also measured at various locations in the test section for both the cases and as shown in Fig. 4.12. The corresponding typical aerosols image (convection rolls) before and after filtration are shown in Fig. 4.13.

To see the effect of emissivity of boundaries, a 5 mm thick anodized aluminum plate was inserted on the top of the test section. With this, the air layers in the test section cannot radiatively cool to the model sky and the system accordingly transitions to a Rayleigh-benard convection scenario. In this case, the temperature difference between boundaries has been maintained approximately at the same level. The emissivity of the top boundary is changed by putting Al-foil to make low emissivity surface and by putting black paint to make high emissivity surface. Vertical temperature profiles for the case ε_b = 0.05 and ε_t =0.9 and for the case ε_b = 0.05 and ε_t =0.05 are shown in Fig. 4.7b and 4.7c, respectively. The shape of

the vertical temperature profiles and the vertical velocity and temperature fluctuation in the test section depend on optical depth, the temperature of radiation boundary and emissivity of boundaries. The temperature gradient near the bottom boundary for these cases is -323 K/m and -510 K/m, respectively and is shown in Fig. 4.9b and Fig. 4.9c. The cooling rate near the bottom boundary for these cases is 0.35 K/s and 0.2 K/s respectively and is shown in Fig. 4.10b, and Fig. 4.10c.

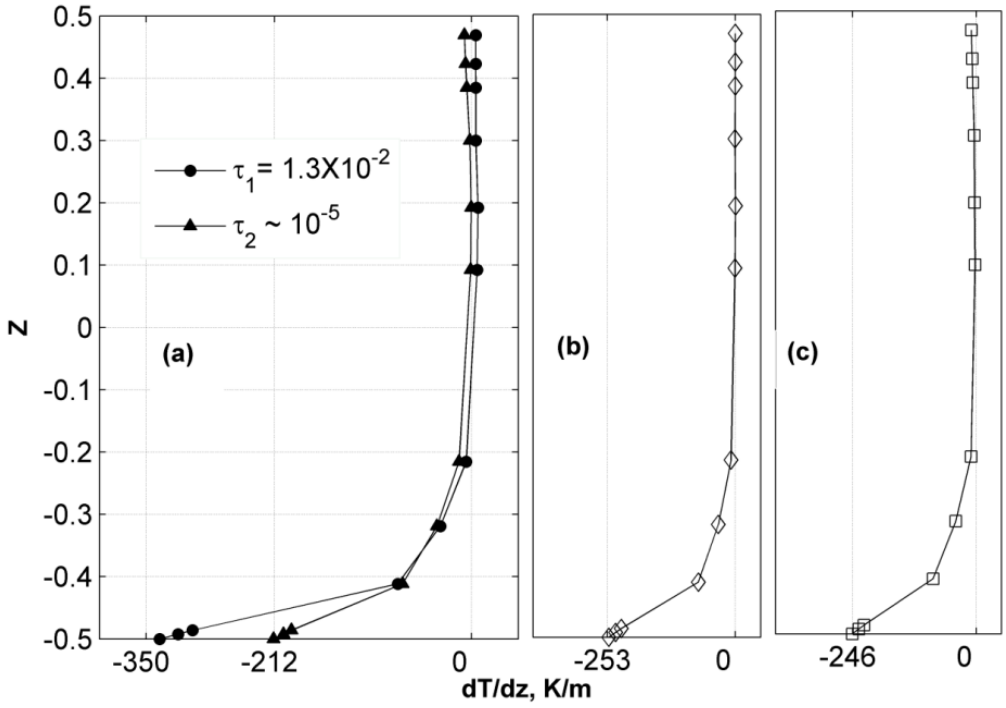

Figure 4.9 Temperature gradient with respect to height in the test section (a) before (τ_1) and after filtration (τ_2). (b) For RBC scenario with ε_b = 0.05 and ε_t =0.9. (c) For RBC scenario with ε_b = 0.05 and ε_t =0.05.

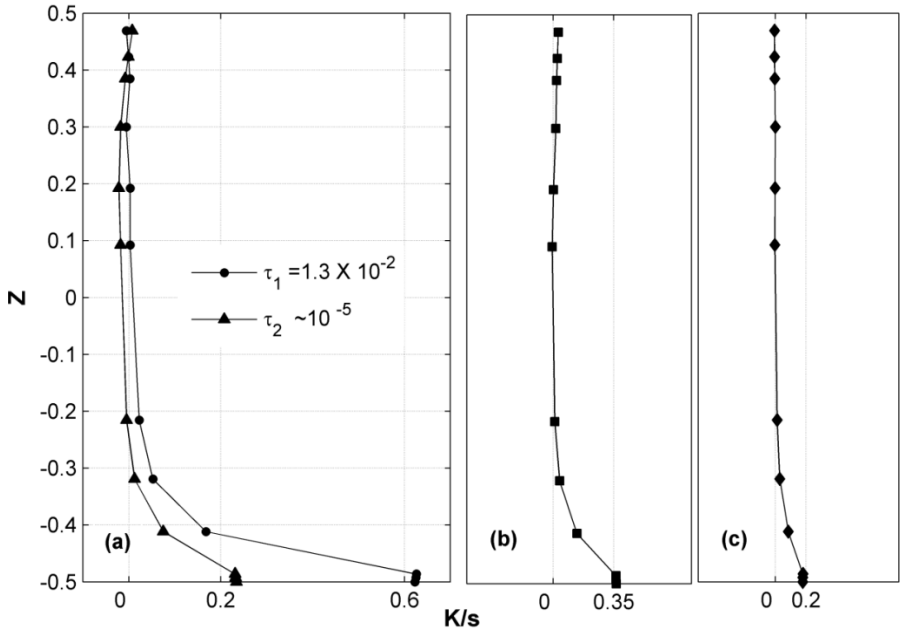

Figure 4.10 Cooling rate with respect to height in the test section (a) before (τ_1) and after filtration (τ_2). (b) For RBC scenario with ε_b = 0.05 and ε_t =0.9. (c) For RBC scenario with ε_b = 0.05 and ε_t =0.05.

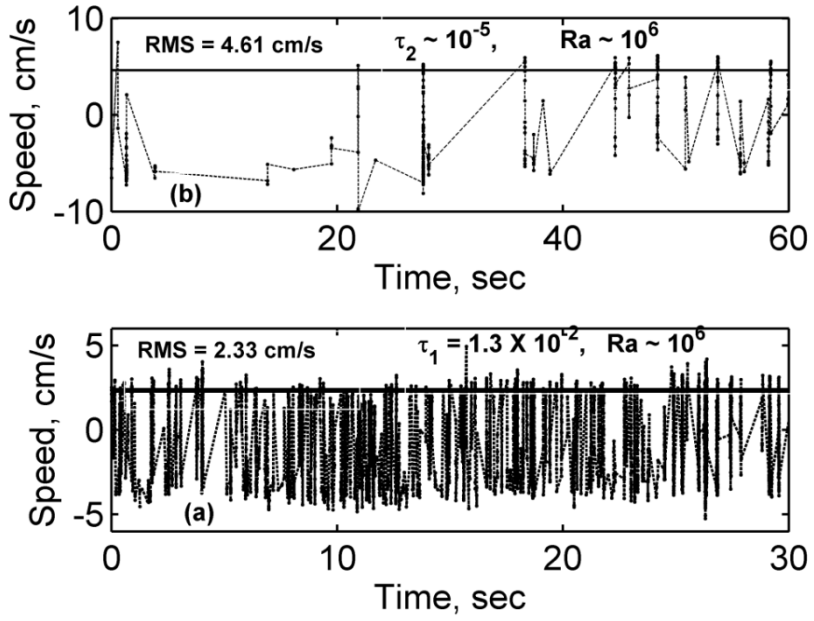

Figure 4.11 Vertical rms velocity in the test section at 20 mm from bottom plate: (a) before (τ_1) and (b) after filtration (τ_2).

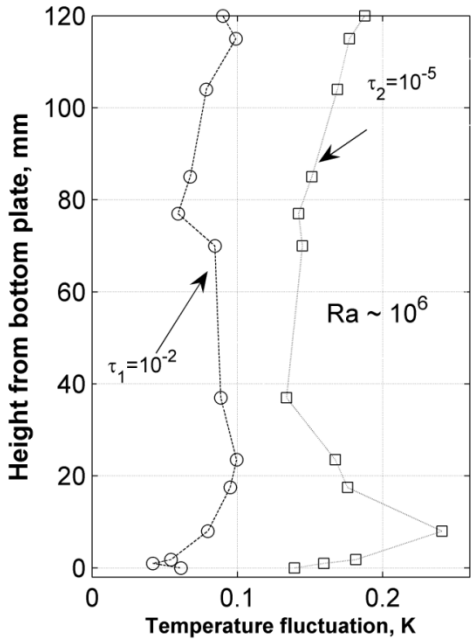

Figure 4.12 Temperature fluctuation at various height in the test section, before (τ_1) and after filtration (τ_2).

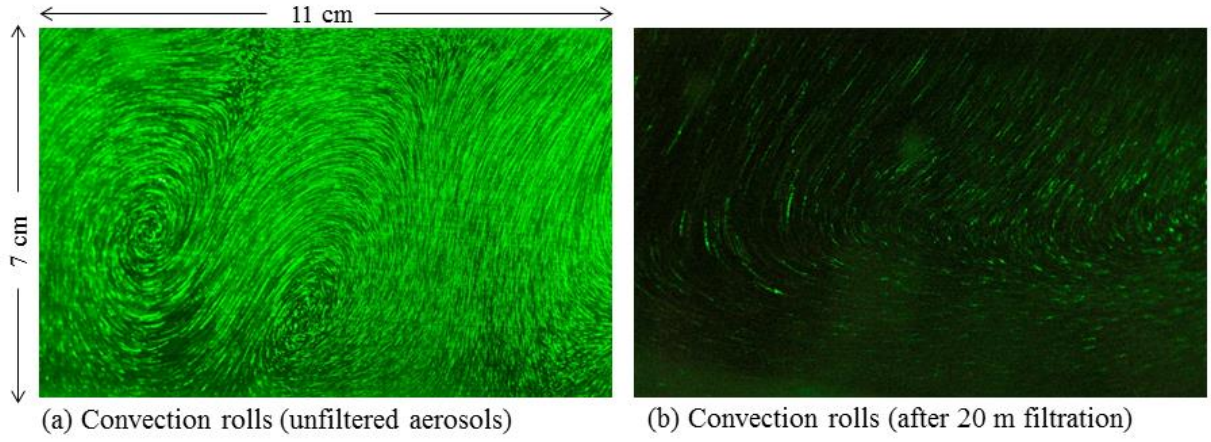

Figure 4.13 Vertical cross section image of convection rolls in the test section at 10 mm to 80 mm from the bottom boundary. Camera setting: t F/11 and exposure time is 1 s. Image area is 70 mm X 110 mm, the light sheet is 2.5 mm thick. (a) before (τ_1) and (b) after filtration(τ_2).

4.6. Effect of hot sky in the stable condition

In a recent study, Bhat (2006) showed that during the day, preferential heating of air layers just above the sea surface occurs due to suspended salt particles, resulting in a temperature profile exhibiting a lifted temperature maximum. The phenomenon has been reproduced in the laboratory and studied in a more controlled manner than what would be possible through field observations. Experiments have been carried out in the laboratory to analyze the effect of suspended aerosols on decouple conduction, convection and radiation boundary condition. In these experiments, the temperature of top boundary has been maintained just greater than the temperature of the bottom boundary to reduce conduction effect. To reproduce the LTMaximum-type profile in the laboratory, the radiation boundary is maintained at higher temperature, which is 323 K. In Fig. 4.14a, vertical temperature profile in the test section is plotted. Inversion temperature profile has been observed up to 23 mm, which then decreases with height. This region (23 mm to 126 mm) is expected to be unstable. Calculated Rayleigh number of this layer is 1.9×10^4, and convection occurs in this region. The observed velocities in the stable and unstable regions are 3 mm/s and 23.45 mm/s, respectively and corresponding aerosols image is shown in Fig. 4.15. As it can be seen in the image, Regions below and above the red line correspond to stable and unstable region respectively. Temperature gradient has been further estimated near the bottom boundary, which is 30 K/m, as shown in Fig. 4.14b.

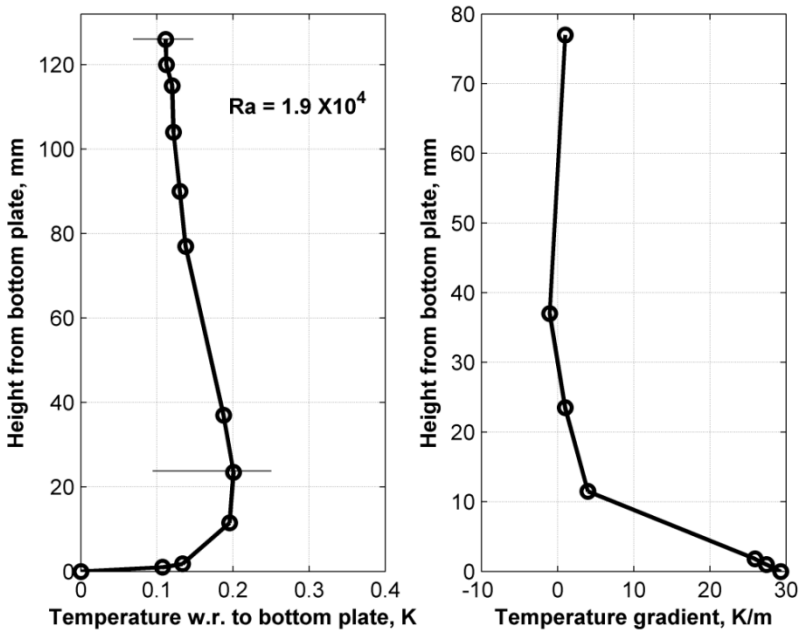

Figure 4.14 (a) Vertical temperature profile with respect to height in the test section in hot Sky condition, Region between the ground and the first line corresponds to stable region and that between the lines corresponds to unstable region. Calculated Rayleigh number for unstable region is 1.9 X 10^4. (b) Temperature gradient with respect to height in the test section.

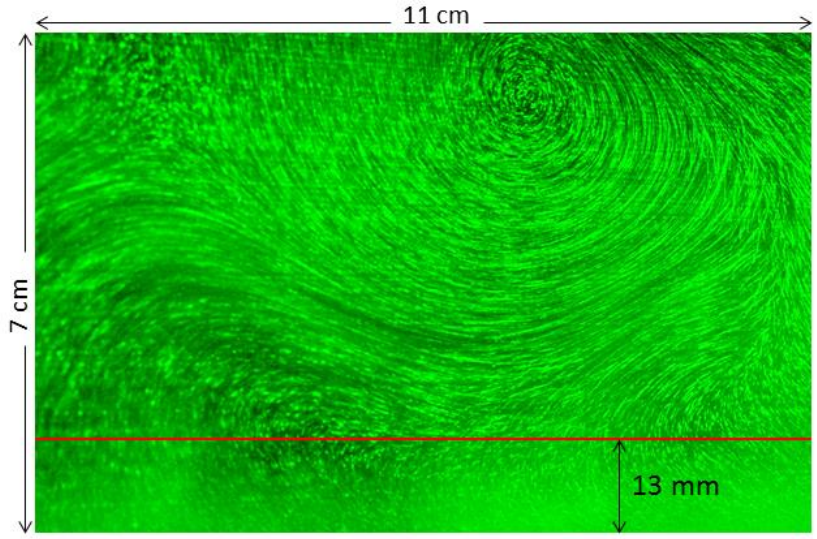

Figure 4.15 Vertical cross section image of convection rolls in the test section at 10 mm to 80 mm from the bottom boundary. Camera setting: t F/11 and exposure time is 1 s. Image area is 70 mm X 110 mm, and the light sheet is 2.5 mm thick. Below and above the red line correspond to stable and unstable region respectively.

4.7. Conclusion

The effects of radiative transfer on the onset of the instability in the LTM region have been presented. The presence of radiatively participating aerosols laden near the surface air layers serves to delay the onset of instability by a factor of 7. In the atmosphere, thermal diffusivity damping is much smaller than radiative damping, thereby, resulting in a decrease of the boundary layer thickness. In the case where the thermal radiation effect is added in RBC, velocity and temperature fluctuation is reduced. We have also observed convection in a stable condition ($T_t > T_b$), the role of destabilizing by hotter sky. Lifted Temperature Maxima profiles have been also reproduced in the laboratory.

CHAPTER 5

Field Experiments:

Convection in the LTM region and radiation fog

5.1. Introduction

The near earth surface vertical distribution of air temperature in the nocturnal boundary layer is important in understanding various micrometeorological processes, such as the growth of inversion layer and formation of radiation fog or frost. The air layers just above the ground cool fastest after the sunset, resulting in an anomalous temperature profile with the minimum temperature occurring a few decimeters above the ground and it is called Lifted Temperature Maximum (LTM), Ramdas layer. Details about Ramdas layer are written in Chapter 2.

An intriguing issue related to the LTM is its apparent stability. Close to the ground in an LTM-region, temperature decreases from the ground to minimum temperature; the Rayleigh number for this layer is O ($10^5 - 10^7$). As the critical Rayleigh number for the onset of convection is O (10^3), this layer should be unstable, but many researchers [Raschke (1957); Oke (1970); Mukund (2008)] have observed that this layer persists throughout the night. Stability is one of the related issues discussed in this chapter.

In this chapter, we will also discuss about radiation fog. Radiation fog, which is generated primarily by nocturnal radiational cooling. A radiation fog has initiation, growth, maintenance, and dissipation stages and it is most common during the early morning hours and during the cool season [Croft (1997)]. Radiation fog cannot form unless the necessary

conditions and key ingredients coincide. When they do, radiative cooling and formation of a stable layer precede fog formation. Surface heat exchange is an important factor influencing these processes. The key low-level ingredients required to generate a radiation fog are moisture, rapid cooling, and calm or light winds. Radiation fog is very unlikely to form unless there is sufficient moisture in the boundary layer. Such moisture may be advected into an area, or derived through daytime evaporation from surface sources such as wetlands or wet soil. As cooling continues, excess water vapor in the saturated layer just above the surface begins to condense into fog droplets. Taylor (1917) appears to have made the first serious study of fogs over sea and land surfaces. His land studies were made at Kew, where he noted that clear skies, light winds, and high relative humidities were conducive to fog formation, but that fog actually occurred on only about half the occasions when it might have been expected. He observed the cooling and drying out of the atmosphere near the ground on a clear night, and realized that the initial formation of fog appeared to depend upon a balance between radiative cooling and turbulence, but the nature of this interaction - and particularly of the role of turbulence - is not at all clear. Kraus (1958) made a series of measurements of wind, temperature and humidity profiles, and of radiation flux at one level on seven consecutive nights during an anticyclonic period in October 1956. He noted that fog began to form when the wind at 1 meter was less than 0.5 m/s. Both Kraus and Stewart attempted to estimate heat budgets, but their results were uncertain since some of the terms, particularly radiative flux divergence, were not measured directly. Monteith (1957) noted that the rate of dew deposition decreased abruptly when the wind speed at 2 m dropped below about 0.5 m/s. He suggested that this resulted in a virtual cessation of turbulent diffusion, thus removing the primary mechanism for dew deposition. Rider and Robinson (1951) noted that the change of

temperature in the lowest layers of air is normally the small resultant of much larger tendencies due to changes in radiative and convective fluxes acting in opposite directions. They also noted a quasi-periodic oscillation of about 10 minute periods in the lowest 0.5 m on one radiation night at about the time of fog formation. There is a general implication in this work that radiative cooling encourages radiation fog formation and turbulent diffusion inhibits it. Fog is the reduction in surface-based visibility to 1 km or less by atmospheric water droplets exhibiting diameters from a few to several tens of micrometers. Radiation fog is ground-based cloud caused by nocturnal infrared cooling at and near the ground surface, and which typically occurs under clear skies and moist low-level conditions-based cloud layer. The importance of dew and frost deposition has also been shown by Guedalia (1994). They observed that the dew deposition caused a delay in the appearance of the fog due to the loss of water vapor in the layers close to the surface. They also showed that the presence of cloud in night may delay the fog onset.

Emmons and Montgomery (1947) proposed that radiative cooling of the air itself as well as surface cooling is generally essential for radiation fog formation as, apart from second-order effects, turbulent loss of moisture at a given level will be too rapid in relation to that of heat from a nearly saturated atmosphere to a colder surface. From theoretical radiation considerations, Fleagle (1953) finds radiative warming immediately above the surface and concludes that fog formation should generally not occur in air layers directly in contact with a cold surface, but at heights near a maximum of radiation cooling rate. Funk (1959) observed vertical radiative cooling-rate distributions could explain the formation of both single and multiple fog layers above a cold surface. Davis (1957) found a dew point

maximum at about 1 m height on calm clear nights with or without subsequent development of fog and suggests this to be a definite contributing factor for fog formation. On his site, fog seems to have formed always in a layer separated from the ground. Stewart (1955) found temperature fluctuation during fog which was not connected with any changes in speed, turbulence of the air flow. He also observed it is apparent that thin fog does not change the structure of the inversion. Funk (1962) observed following phenomena; a) cooling rate fluctuation preceding fog b) reduced radiative cooling or even warming above and below fog layers c) the possibility of high radiative cooling rates just before fog formation. It appears that these phenomena are caused by changes in the emissive properties of the air layers affected, changes which are not necessarily associated with any distinct visual signs, the vertical distribution of haze being apparently just as important. Their observational results thus show quite conclusively that at least near the ground, radiation fog formation is directly caused by radiative heat loss by the air, and therefore earlier concepts in terms of the turbulent propagation of cooling upward from the ground surface are untenable. In earlier research, high cooling rate, low wind speed and high relative humidity are shown to be ideal conditions for formation of radiation fog. In Fig. 5.1, dew point and air temperature are plotted with respect to height and vertical temperature profile near the ground in calm and clear sky conditions. Before radiation fog formation, they have observed that the vertical temperature profile near the ground is inversion and after radiation fog formation temperature of the ground had increased (due to radiation shielding by fog) and there is convective region near the ground. But in reality, in calm and clear sky conditions, there is LTM-type profile near the ground instead of inversion profile. They missed out this phenomenon because this phenomenon only happens below two meters height.

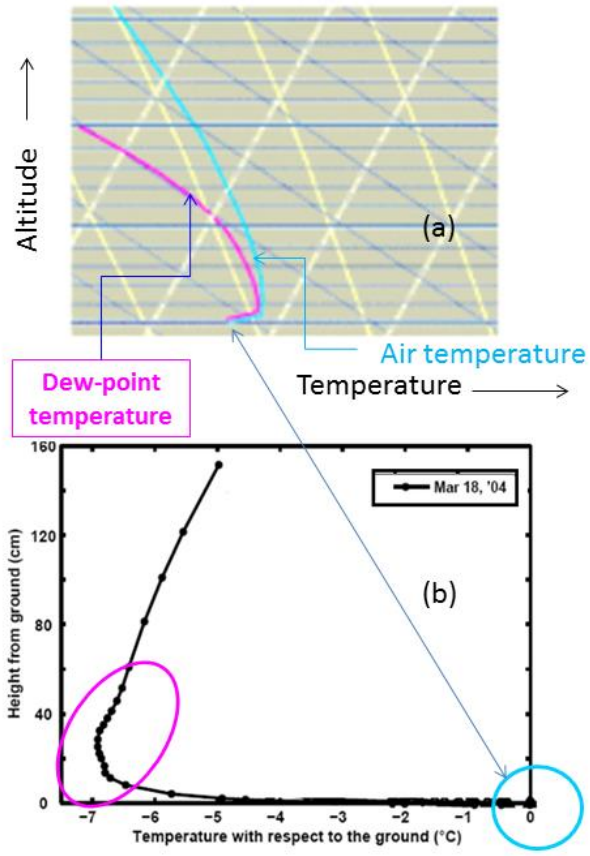

Figure 5.1. Schematic of favorable conditions for formation of radiation fog. [5](a) Dew point and air temperature (b) Typical vertical temperature profile near the ground in night time.

In this chapter, we will discuss about the effect of wind on the LTM-type profile and we will study stability analysis in the LTM region. We will also discuss about radiation fog and finally, we will present the effect of rain.

[5] This picture have taken from the COMET Program; http:www.meted.ucar.edu/

5.2. Observation site

The observations were carried out at the field in the campus of JNCASR, Bangalore, India. In order to make temperature measurements with a high vertical resolution close to the surface, a circular bare soil patch with approximately smooth surface finish was laid at a suitable location in the field, and served as the measurement site. The patch was 10 m in diameter and was surrounded by short dry grass. A view of the observation site is shown in Fig. 5.2 and a closer view of the observation site is shown in Fig. 5.3. Around the observation site, other than patches of dry grass, the ground was flat and bare, for a distance of 30 meters along the north and south, and for about 100 meters along the east and west directions respectively. The observations were made directly over the bare soil patch and it's referring as high emissivity and high thermal inertia. The experimental setup consists of a mast carrying thermocouples to record temperatures, a humidity sensor for measuring moisture level near the ground, and a portable Mini-LDV system (Measurement science Enterprises, Pasadena, CA, USA) for monitoring wind speed. The Mini-LDV system records velocity at a height of 20 cm from the ground and is capable of measuring velocity with naturally occurring aerosols in the air (of size $\approx$ 1μm or larger). The schematic of this experimental set up is shown in Fig. 5.4 and a vertical laser sheet, obtained using a 500mW continuous green laser, and a Nikon-D90 digital camera for capturing aerosols. The thickness of the light sheet is about 2.5 mm and the position of camera is at about 40^0 from the laser sheet. The schematic of aerosols visualization is shown in Fig 5.5.

Figure 5.2. A view of the observation site at the field situated in the campus of JNCASR, Bangalore, India.

Figure 5.3. A photograph of a close view of the bare soil patch, which constitutes the observation site. The grass on the patch is also visible.

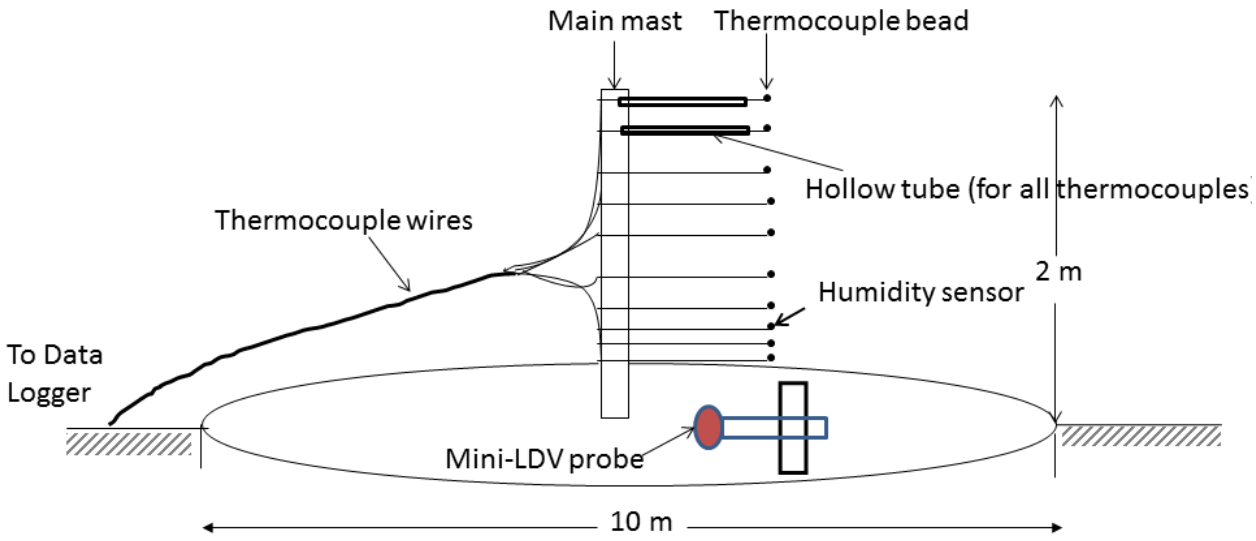

Figure 5.4. A schematic showing the manner in which the thermocouples were mounted on the main mast. The thermocouples were inserted into hallow aluminum tubes which were then inserted together into holes that had been bored into the mast for this purpose.

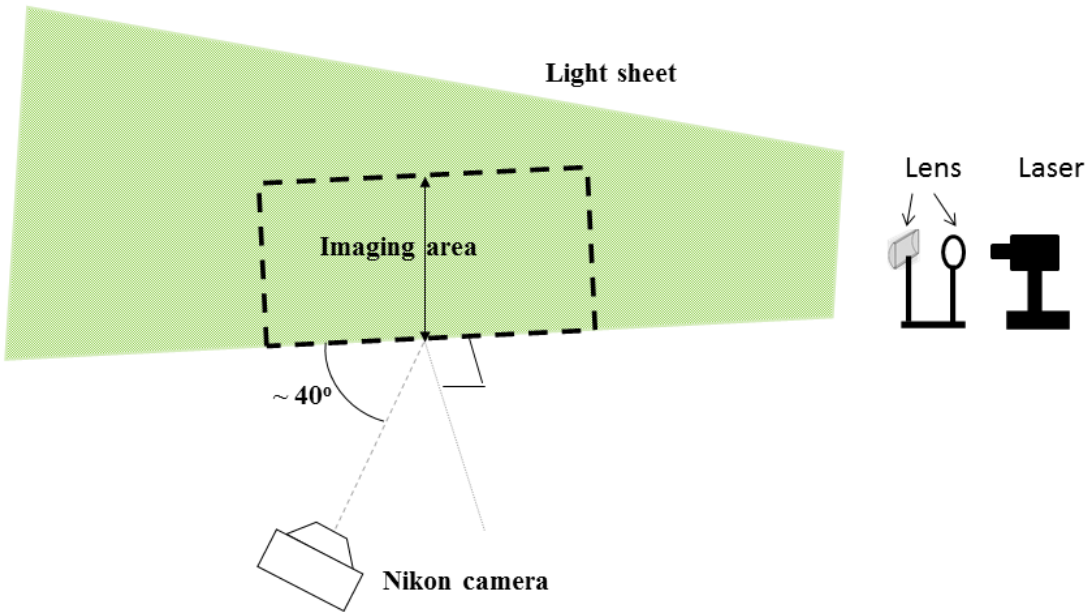

Figure 5.5. Schematic of the setup used in the outdoor experiments to record aerosols.

5.3. Instrumentation

In this section, the instrumentation used in the field observations is discussed. Following instruments are used in field observations. (a) Thermocouples to measure the vertical temperature profiles. For measuring the temperature of air, 25 thermocouples were used and three thermocouples were used for measurement of ground temperature. (b) Laser Doppler Velocitymetry (Mini LDV) to measure the vertical and horizontal wind speed. (c) Humidity sensor to measure moisture level. (d) Continuous green laser (500 mw and 300 mw, with 532 nm wavelength) and Nikon D-90 camera to visualize the aerosols.

5.3.1. Temperature sensors

The K-type thermocouple was chosen as the temperature sensor because it meets our requirements. Fast response times would be preferred due to short radiative time constants. Chromel (90% nickel and 10% chromium) - Alumel (95% nickel, 2% manganese, 2% aluminum and 1% silicon) (type k) thermocouple has a high sensitivity and stability in the temperature range of our interest. We have used 0.25 mm diameter thermocouple wires. All the thermocouple wires used in the measurements were cut from a single reel of thermocouple wire to ensure the same calibration constants for all the thermocouples. We have used 20 thermocouples for measuring the vertical temperature profiles. These were fused in the usual fashion, with the chrome and aluminum wires exposed a little at the end of the thermocouple wire, and then fused to form a small bead of diameter 0.5 mm. as shown in Fig. 5.6. These were mounted on the mast with the help of hollow stainless steel tubes and a schematic of this as shown in Fig. 5.4. The highest point of measurement was 2 m. For measuring the ground temperature, thermocouples fused in the usual fashion were used, but

with the difference that just after fusing, when the beads were still soft, they were beaten into thin discs with a thickness of 0.25 mm.

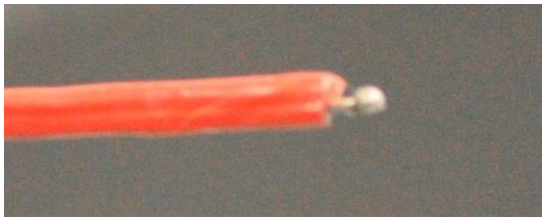

Figure.5.6. A photograph of the end of a single K-type (chromel-alumel) thermocouple sensor, showing the thermocouple wires fused in the usual fashion, with the copper and constantan wires exposed at the end of the covering sheath, and then fused to form a small bead of a diameter of around 0.5 mm.

For measuring the ground temperature, a small piece (5 cm X 5 cm X 2 mm) of metal was dug into the ground and on the metal piece these thermocouples were taped with a little conducting paste. The emissivity of the metal block is different from the ground, so we have put a sand of 1 mm thickness on the metal to maintain the level of the ground.

All the thermocouple sensors had a common reference junction. This reference junction was kept embedded in a metal block. This block was placed in an insulated box so that its temperature, and consequently that of the reference junction changed very slowly. The temperature of the reference junction was monitored with a thermometer embedded in the same metal block. The thermocouples were calibrated at the beginning of every month. The calibration was carried out in the lab in a hot water bath. All thermocouples were immersed in a beaker of well stirred water. All the thermocouples agreed to within ± 0.05 of each other. A note must be added on the radiation error. The radiation error of temperature sensors is an important aspect of field measurements. Sensors are usually shielded to minimize the

radiation error. In the present case, this was impractical due to number of sensors, the vertical distance between the near surface sensors, and the temporary nature of the set up. Also, shielding will tend to reduce response times whereas quick response times are desirable due to small radiative time constants. However at night times, for good quality of sensors like those used here, the radiation errors were quite small (for example Fritschen & Gay (1979) and Raschke (1954)). In our case, for example, the error was less than about ± 0.5^{o}C for the extreme case of zero wind.

5.3.2 Laser Doppler velocitymetry (Mini-LDV)

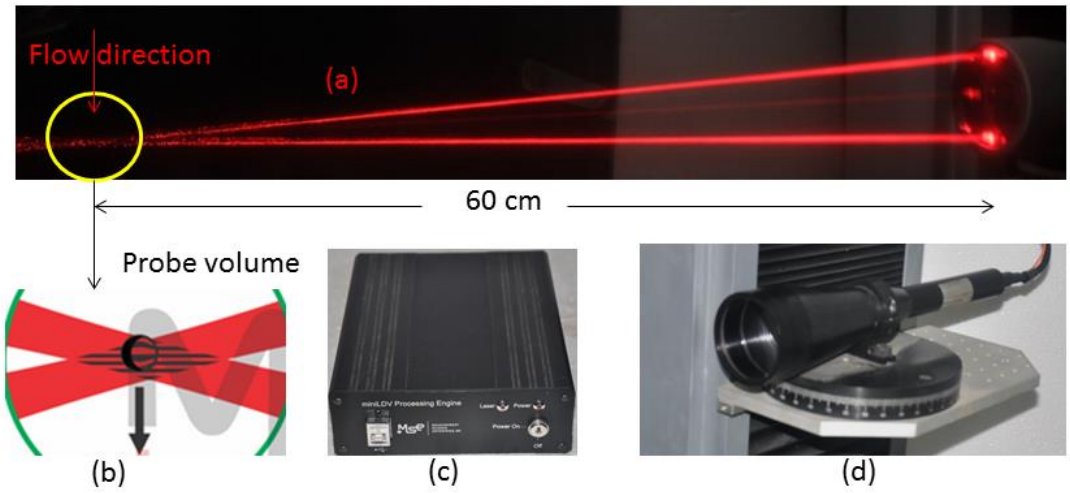

Figure 5.7. (a) Mini-LDV laser beam with interface (probe volume) (b) Magnified probe volume with fringes (c) Processor of Mini-LDV (d) Prove of Mini-LDV with traverse set up.

A Laser Doppler Velocimeter (LDV), also known as a Laser Doppler Anemometer (LDA), is a type of interferometer that measures the velocity of objects and number of particles crossing the probe volume per second using laser light ($\boldsymbol{\lambda}$ = 632 nm). The objects can be microscopic particles in a fluid or solid surfaces. The concept is even used in some high-end laser mice. The Mini-LDV probe contains a laser, miniature beam shaping optics, receiving

optics, and a detection system. The sensor is 32 mm in diameter and 165 mm long, and the fixed distance between the sensor and probe volume (600 mm). The size of the probe volume (measurement domain) is 0.15 mm X 0.3 mm X 3 mm and as shown in Fig. 5.7.

In a Laser Doppler velocimeter, two coherent laser beams are crossed (forming the probe volume) to generate interference fringes. When a particle or microscopically textured surface moves through this region, it reflects bursts of light corresponding to its passage through the regions of constructive interference. Since the spacing between the fringes is constant, the velocity of the particle or surface is proportional to the frequency of the reflected bursts. The Mini-LDV sensor has a measurement range from 1 mm/sec to 300 m/sec with a repeatability uncertainty of 0.1% and an accuracy of 99.7%.

A laser beam is split and the two "arms" are made to cross outside the sensor. This crossing region is called the probe volume. Because the two arms come from the same beam, when they cross, an interference pattern is generated, and light and dark stripes form inside the probe volume. These stripes are called "fringes". The physical distance between the fringes is known from the calibration. Hence, the frequency of the intensity signal is directly proportional to the velocity of the particle. Velocity = fringe spacing x intensity frequency.

When two beams are crossed in space as in a classical LDV, the interference pattern is steady with space. This means that a) it is impossible to know if the particle was traveling from left to right or right to left, and b) it is impossible to measure very low velocities, because it will take too long for the particle to travel through a bright and dark region (alternatively, the beat frequency is too low). The trick is to add a Doppler shift to the beams themselves. When an LDV has "frequency shifting", the beams already have a frequency difference when they are

in space, so if a particle has zero velocity, the recorded signal will have the same frequency as the difference in frequency between the two beams. The effective frequency of the signal is the sum of the frequency due to the particle motion and the shift frequency. Therefore, when a particle is going one way it will add to the shift frequency; going the other way it will subtract and if it has velocity zero it does not change the shift frequency. Viewed another way, the fringes are moving in space, so the actual measurement is the velocity of the particle relative to the velocity of the fringes.

5.3.3. Humidity sensor

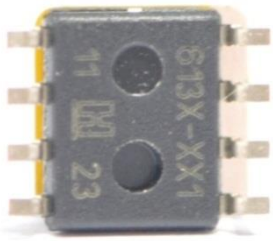

Figure 5.8. A photograph of the humidity sensor (Honeywell make) used in the observation.

The HIH-6131-021-001 series humidity sensor manufactured by Honeywell was used in our observations. The sensor uses a laser trimmed thermoset polymer capacitive sensing element with on-chip integrated signal conditioning. It is available in a molded plastic housing with a thermoplastic cover. The sensing element's multilayered construction provides excellent resistance to wetting, dust, dirt, oils, and common environmental chemicals. The sensor directly detects changes in relative saturation (which is a measure of the relative humidity) as a change in sensor capacitance, with fast response, high linearity, and excellent long-term stability. The sensor is small (about 5 mm by 5 mm) and light (0.09 grams), inexpensive, and

its power consumption is only 1 mW as shown in Fig. 5.8. The output of the sensor is converted into a relative humidity reading by means of a sensor-specific equation:

$$RH = (V_{hum} - 0.89)/0.0307$$

Where RH is the relative humidity and V_{hum} is the output (in volts) of the sensor. Though the temperature effect for the sensor is small, the relative humidity so obtained is then corrected for temperature effects using a sensor independent equation provided by the manufacturer:

$$True\text{RH} = \text{RH}/ (1.0546 - 0.00216\text{T})$$

Where T is the temperature in ^{o}C and *True*RH is the corrected relative humidity. The sensor provides a relative humidity accuracy of ± 4% over the maximum of relative humidity. The sensor was mounted on the main mast at the same height (25 cm from the ground) as one of the thermocouples. The temperature reading obtained from this thermocouple was then used to convert the relative humidity readings into absolute humidity. The sensor comes calibrated (in the form of a sensor-specific equation), and is very stable with the drift typically being less than 1% RH in five years.

5.4. Results

5.4.1. Convection in the LTM region

In this section, convection near the ground (LTM-region) is discussed. Images of aerosols have been taken in the LTM region (2-25 cm) to visualize convection. The temperature fluctuation was also monitored in the LTM region. Temperature fluctuation, however, also depends on wind speed and wind speed is not constant throughout the entire observation

period. In chapter 4, the effect of radiative transfer on the onset of instability in the laboratory LTM region was presented, where the presence of radiatively participating aerosols laden near surface air layers was shown to enhance the stability by a factor of up to seven. However, in the field experiments, parameters like intensity of minimum, height of minimum, Rayleigh number etc., cannot be controlled.

In Figure 5.9 a, b, c, and d, the vertical temperature profiles are plotted for the various days in our observation site, where intensity and height of minimum are 3.7 K, 4.1 K, 4.5 K, 4.7 K and 19.5 cm, 24.5 cm, 14 cm, 24.5 cm respectively. The calculated Rayleigh number for this layer based on corresponding intensity and height of minimum are 9×10^5, 5×10^6, 7×10^4 and 6×10^6 respectively. The corresponding images have been taken during the experiment near the ground, around the LTM-region. The typical vertical images have been taken at 2 cm to 26 cm from the ground. Images have been taken every second, and the corresponding image is shown in Fig. 5.10. As it can be seen in this image, convection rolls are obtained up to height of the LTM. It should be noted that the height of the convection roll is approximately the same as that of the LTM.

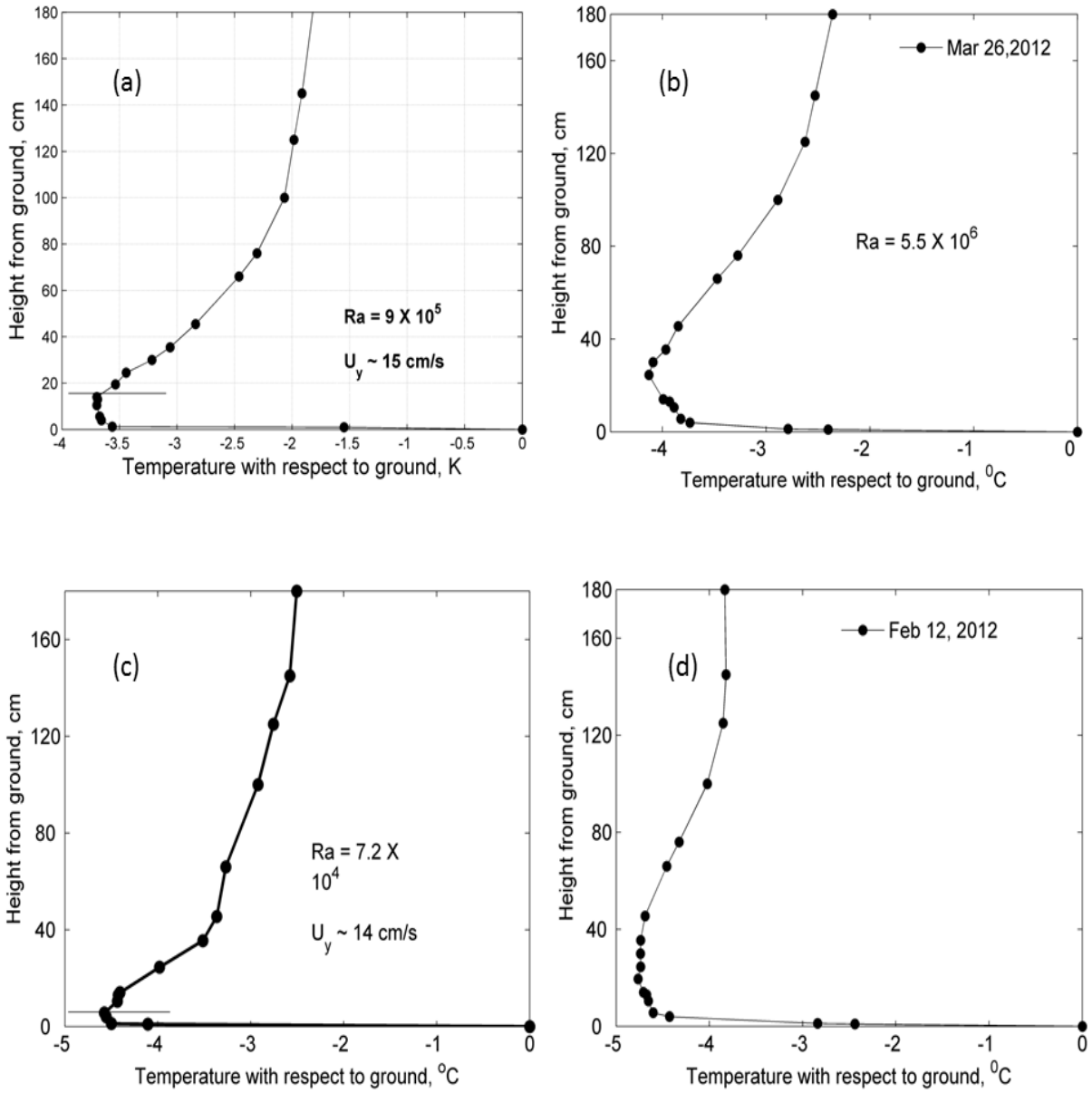

Figure 5.9 The vertical temperature profiles near the ground at low wind conditions.

.

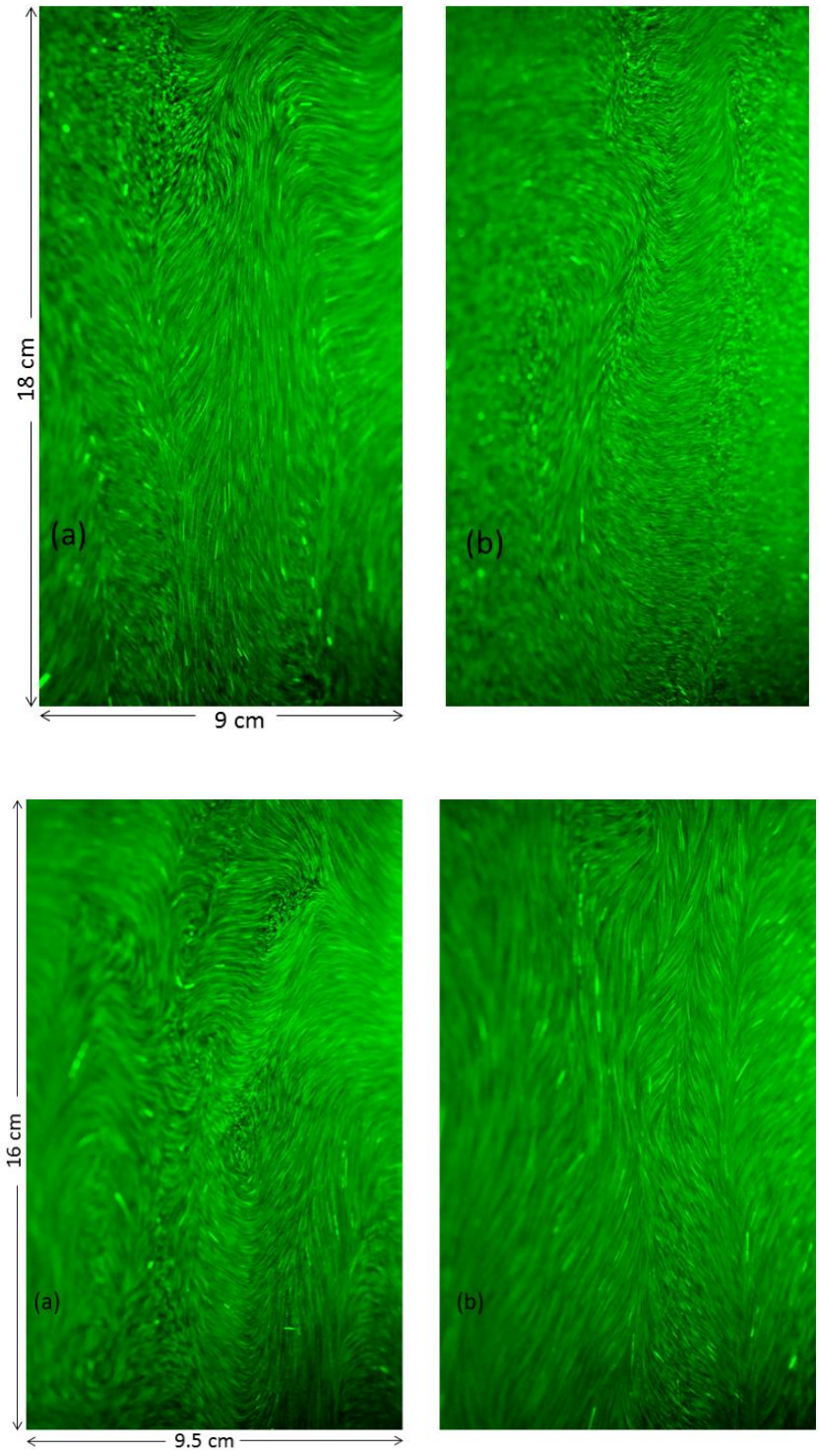

Figure 5.10. Corresponding aerosols images near the ground, showing convection in the LTMregion.

Convection rolls cannot be seen at all times near the ground, since two types of motions are present there – the ambient flow of air in the horizontal direction and the flow of air upwards due to convection. It was observed that convection rolls were absent when the horizontal wind speed exceeded around 1 m/s. Convection rolls are difficult to obtain at all times in the field experiments due to certain limitations of our experiment. For instance, if the direction of ambient airflow is not exactly in the same direction as that of the laser sheet, which is 2.5 mm thick, the convection rolls cannot be recorded.

In previous results, we have observed convection in the LTM-region and the length scale of the convection roll is a function of height of the minimum, convective velocity, temperature gradient, and ambient flow (in horizontal direction). In a low wind condition, the height of convection rolls is equal to or more than height of minimium. The convective velocity at height of minimum is non-zero. Therefore, the length scales of convection rolls may penterate beyond the height of minimum to some extent.

Previous literature reports have shown that the interfacial layer (IL) between the convectively driven atmospheric boundary layer and the stably stratified free atmosphere above is subjected to intense turbulent mixing due to entrainment of air by convective motions. As a result, the IL rises or, equivalently, the boundary layer deepens. Otte &Wyngaard (2001) have performed the modeling of the entrainment processes. Several entrainment law formulations have been derived to date, which relate the entrainment velocity, namely the velocity at which the interface rises to measurable parameters of the mixed and interfacial layers. From an experimental point of view, the entrainment processes across a density interface have been studied extensively in liquid media [Hopfinger (1987); Fernando (1999)].

When entrainment results from grid-generated turbulence were studied, the dimensionless entrainment velocity was found to vary as R_i^{-n} where n is in the range 1−2 depending upon the values of the Prandtl and Richardson numbers. For strong enough stratification of the interface, Turner (1968) found that for density differences produced by heat alone, n is close to 1, and in the presence of salinity, the difference across the interface n is close to 3/2. In the convection tank experiment by Deardorff, Willis & Stockton (1980), the dimensionless entrainment velocity was found to vary as -1.

When mixing occurs in a stably stratified fluid, the center of mass of the fluid system rises. Hence, the potential energy of the fluid system increases through mixing. The potential energy associated with reversible processes is the available potential energy [Lorenz (1955)] and vanishes when the flow returns to its rest state. The potential energy associated with irreversible processes like mixing is the minimum potential energy of the fluid system and always increases through mixing.

Deardorff et al (1970) have used the temperature difference over the penetration length scale for the definition of Richardson number. The penetration height Z_p is estimated by equating the kinetic energy per unit volume of the fluid in the mixed layer (below LTM height) to the potential energy gain (above LTM height). In lifting a unit volume of fluid from below the LTM height into the inversion zone (above LTM) to a height of Z_p above the height of minimum, K.E. $\approx \rho \frac{U_c^2}{2}$, where U_c is convective velocity given by $U_c = \sqrt[3]{\frac{g\beta Q_b h}{\rho C_p}}$ ..(5.1)

[Deardorff (1980)] .Here, Q_b = heat flux on the ground, given by $Q_b = K_a \frac{\partial T}{\partial z}\Big|_{z=0}$

From Sreenivas 1995,

$$Z_p = \frac{-A_2 + \sqrt{A_2^2 - 4A_1 A_3}}{2A_1} \quad (5.2)$$

where, $A_1 = \frac{g}{T}\frac{\partial T}{\partial z}\Big|_{z=interface}$, A_2=0, since there is no density jump across the interface; A_3= -$\frac{U_c^2}{2}$ and Richardson Number (Ri) $= \frac{g\,(\Delta T)h}{\bar{T}\,U_c^2}$ (5.3)

Data from nine nights have been taken to estimate the shape of convection rolls. Details of experimental data have been given in Table 5.1.

Table 5.1. Details of field experiments are summerized. ΔT is the intensity of minimum, h is height of minimum, R_a is Rayleigh number for Randas layer and U_h is ambient flow at around 20 cm from the ground.

case	Date (2012)	ΔT(K)	h(cm)	Ra	$U_h(cm/s)$
1	15-Feb	4.7 ± 0.03	19.5	3.1 X 10^6	11
2	03-March	3.9 ± 0.03	14	9.8 X 10^5	12
3	11-Feb	4 ± 0.03	15	9 X 10^5	10
4	19-May	3.6 ± 0.03	24.5	8 X 10^6	13
5	28-Feb	4.5 ± 0.03	24.5	6 X 10^6	10
6	02-March	2 ± 0.03	13	3 X 10^4	80
7	08-Feb	1.1 ± 0.03	19.5	7.4 X 10^5	90
8	09-April	0.6 ± 0.03	5.6	9.6 X 10^3	120
9	23- April	0.4 ± 0.03	1.2	6.4 X 10^1	160

When the turbulence level is low near the ground, convection rolls are obsorved in the LTM region. Therefore, we have considered five sets of data, where wind speed is low and it is O (10 cm/s). For experiments 1-5, the convective velocity (U_c) has been estimated by using equation (5.1) and penetration heigh, Z_p by using equation (5.2).

Case 1 shows the experimental measurements of vertical temperature profiles and wind velocity near the surface, taken on 15th February, 2012, where ambient flow and convective flow are almost the same. The corresponding image is presented in Fig. 5.11. The red line indicates the height of minimum (interface). As shown in Fig. 5.11, the fluid parcel (water vapor and aerosol) rises above the red line and it returns from around 4 cm above the red line. The calculated Z_p by using equation (5.2) is around the same and it is 3.6 cm.

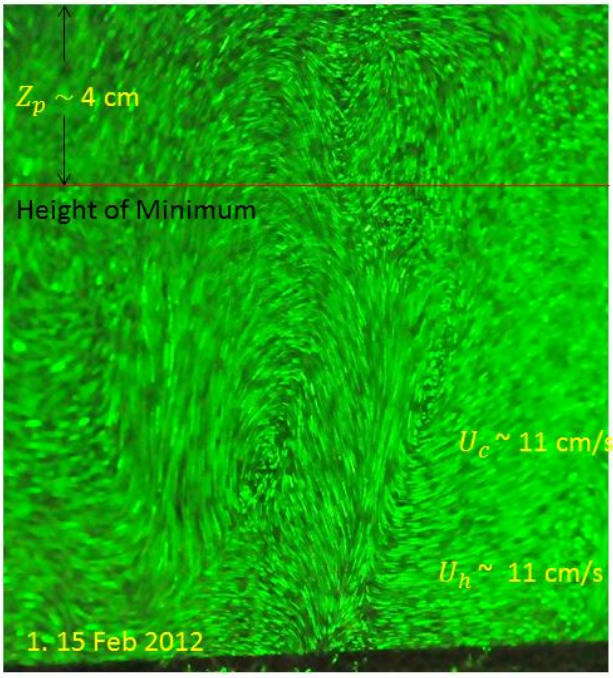

Figure 5.11. The aerosols image corresponding to case 1, showing convection in the LTM-region and fluid parcels are going above the LTM height.

In Fig. 5.12, we have considered case 2 and case 3 where convective velocity is approximately the same (~ 8 cm/s) and ambient flow is ~ 12 cm/s around LTM height. Images of the convective rolls corresponding to these cases have been shown in Fig. 5.12. In these cases, some fluid parcel turns into a spiral/curly/circular path due to shear stress; also sometimes the fluid parcel rises above the red line. The calculated Z_p in both the cases estimated from the images and by equation (5.2) are of the same order and are summarized in Table 5.2.

In Fig. 5.13, case 4 and case 5 have been considered where convective velocity is approximately the same (~ 10 cm/s) and ambient flow is ~ 11 cm/s around the LTM height. The images of the convective rolls corresponding to these cases have been shown in

Table 5.2. Convective velocity (W_c) in cm/s, penetrating length (Z_p) in cm, and Richardson number have been estimated and observed penetrating length for case1-5, in low wind condition.

Case	W_c	Z_p(estimated)	Z_p(observed)	Ri
1	11.46	3.7	4	2.29
2	8.96	3.6	3	2.17
3	8.7	3.7	4	2.19
4	10.8	7.5	6	2.6
5	11.6	7.4	5	2.6

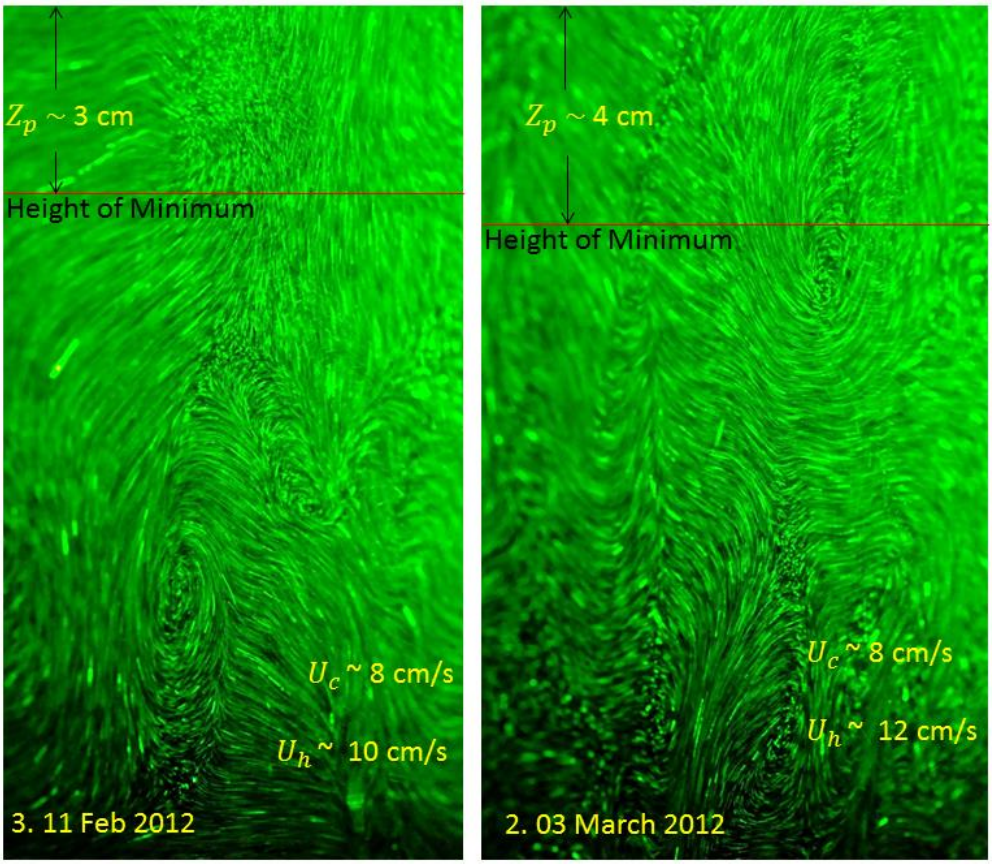

Figure 5.12 The aerosols image corresponding to case 2 and case 3, showing various shapes of convection in the LTM region and fluid parcels are going above the LTM height.

Fig. 5.13: In these cases, Z_p is more than the previous cases, which can be attributed to the height of minimum being more than the previous case (~ 24.5 cm from the ground). The features of the results presented for the above few cases with low turbulence level and convective LTM region were observed during many nights, and various shapes of convection rolls could be been obtained. The following paragraphs would summarize the cases where the turbulence level was higher than that the ones discussed till now.

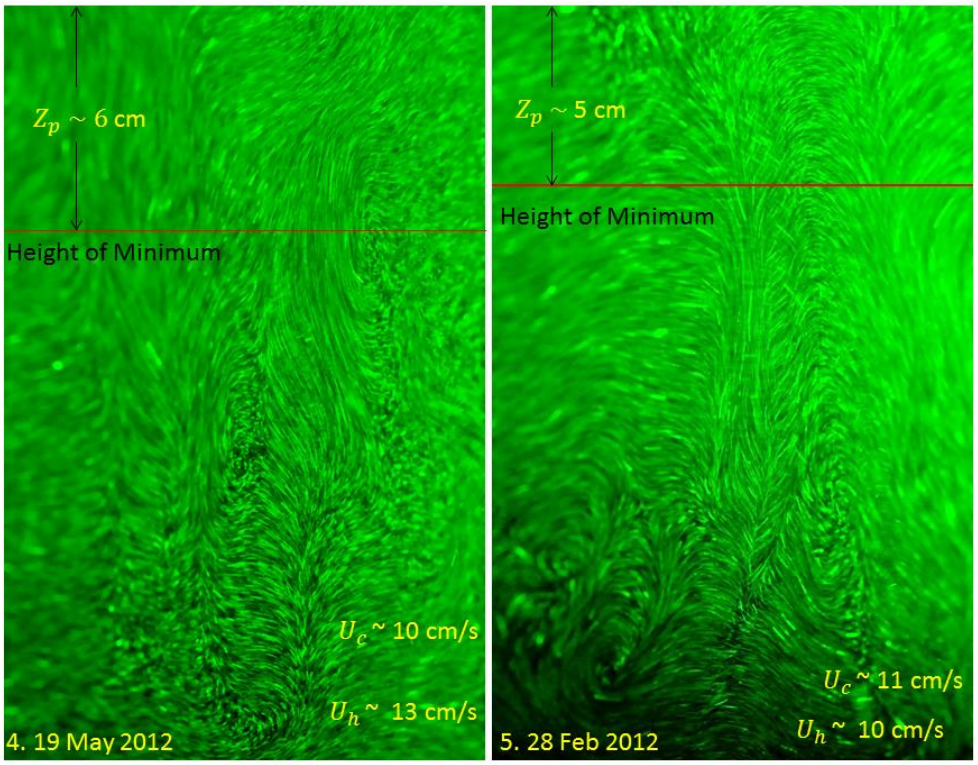

Figure 5.13. The aerosols' image corresponding to case 4 and case 5, showing various shapes of convection in the LTM region and fluid parcels are going above the LTM height.

Cases 6-9 represent the cases when the turbulence level is high and hence the intensity and height of minimum decreased. In case 6, the ambient flow is 80 cm/s and height of minimum is 19.6 cm from the ground. In this case, there is no difference of flow below and above the red- line (LTM height). Convection is not observed in this case and is shown in Fig. 5.14. However, at instants when the ambient flow was slightly higher (90 cm/s), it could be seen that some fluid parcel is raised with a certain convective velocity, but due to high ambient flow, it gets ultimately suppressed by shear forces (Fig. 5.14). Further increasing the turbulence level near the ground results in a sharp decrease in the height and intensity of minimum such that vertical LTM type profile gets almost shifted into an inversion profile. In such cases, a wavy path of flow has been observed near the ground and is shown in Fig. 5.15.

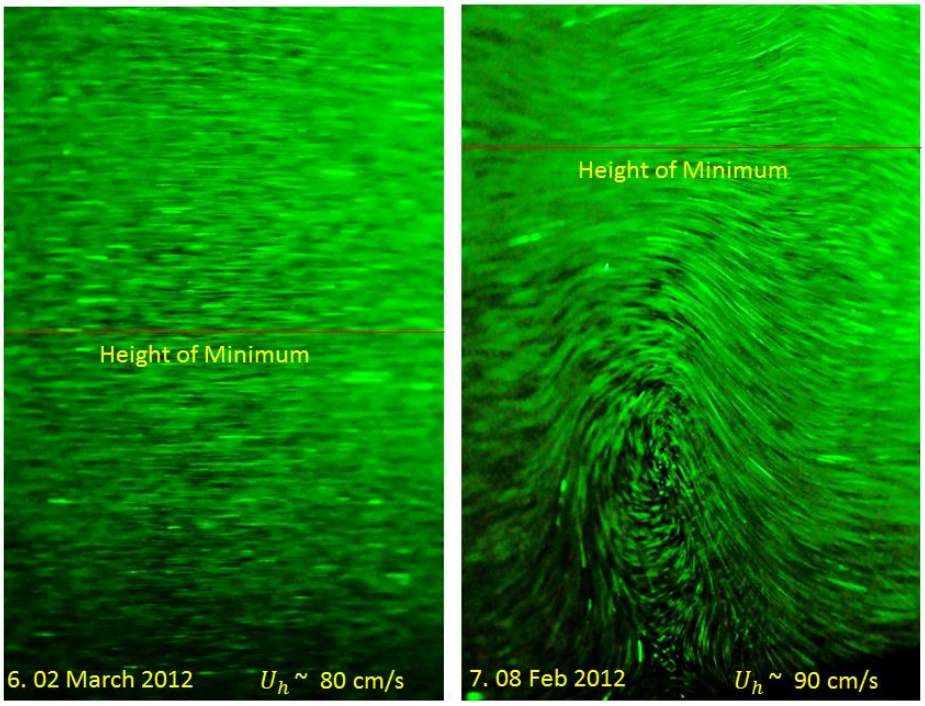

Figure 5.14. The aerosols image corresponding to case 6 and case 7, showing disappeared convection in the LTM region due to high wind condition.

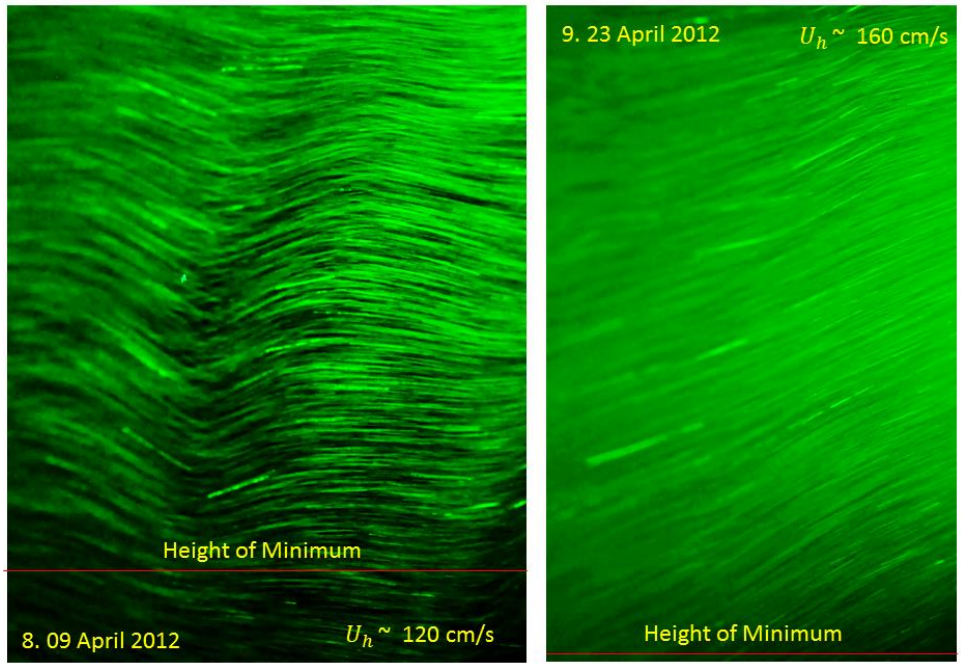

Figure 5.15. The aerosols' image corresponding to case 8 and case 9, showing motion of aerosols, when LTM-type profile shifted to an inversion profile.

5.4.2. Radiation fog

For formation of radiation fog, the dew point temperature has to saturate to a value same as that of the air or ground temperature. Near the ground, the temperature of air is around 5^{o}C less than the ground temperature in clear and calm sky conditions. The relative humidity is more or less constant with respect to the height near the ground. Hence, air layers around the LTM height are saturated with dew-point temperature and the expected height for fog formation is around the height of minimum rather than on the ground.

Radiation fog has been observed for nine nights during winter on our site (JNCASR,Bangalore). In general, the radiation fog is formed during the second half of the night. In Fig. 5.16, the top panel shows relative humidity (RH) with respect to time, the middle panel shows dew point temperature, air temperature, and ground temperature with respect to time and the bottom panel shows the vertical temperature profile before and during fog formation.

After sunset, RH increases and at around 0130 hours, RH becomes greater than 90%. After sunset, the dew point temperature has increased due to increased RH and temperature of air near the ground has decreased due to cooling by radiation. At around 0200 hours dew point temperature and air temperature are in saturation and then radiation fog is formed. However, at this point of time, the temperature of the ground is greater than the dew point temperature. Therefore, radiation fog is formed at around height of minimum rather than on the ground.

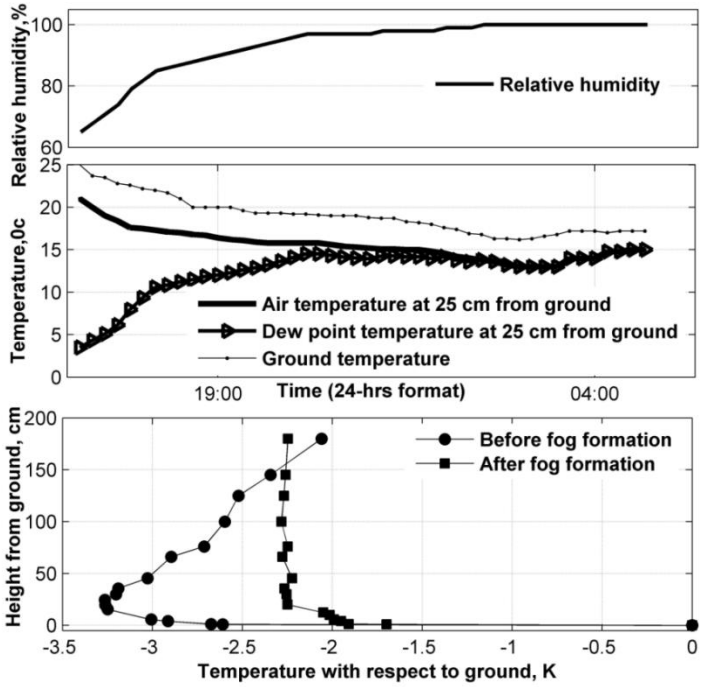

[6]Figure 5.16. Relative humidity at around LTM height in the top panel, air temperature, dew point temperature and the ground temperature in the middle panel and temperature profiles before and during fog in the bottom panel.

During the experiments, images of aerosols have been taken at every second. Radiation fog just after (during) formation is shown in Fig. 5.17. In the images, the red line indicates the interface of radiation fog and aerosols. Just before the fog formation, the height of minimum is around 25 cm from the ground. Height of red line is 16 cm + 2 cm (images have been taken at 2 cm from the ground) from the ground. Therefore, the vertical temperature profile is very important for the formation of radiation fog.

[6] SINGH, D. K., PONNULAKSHMI, V. K., MUKUND, V., SUBRAMANIAN, G. ,AND SREENIVAS, K. R.,(2013), Radiation forcing by the atmospheric aerosols in the nocturnal boundary layer. AIP Conf. Proc. 1531, 596 (2013); http://dx.doi.org/10.1063/1.4804840.

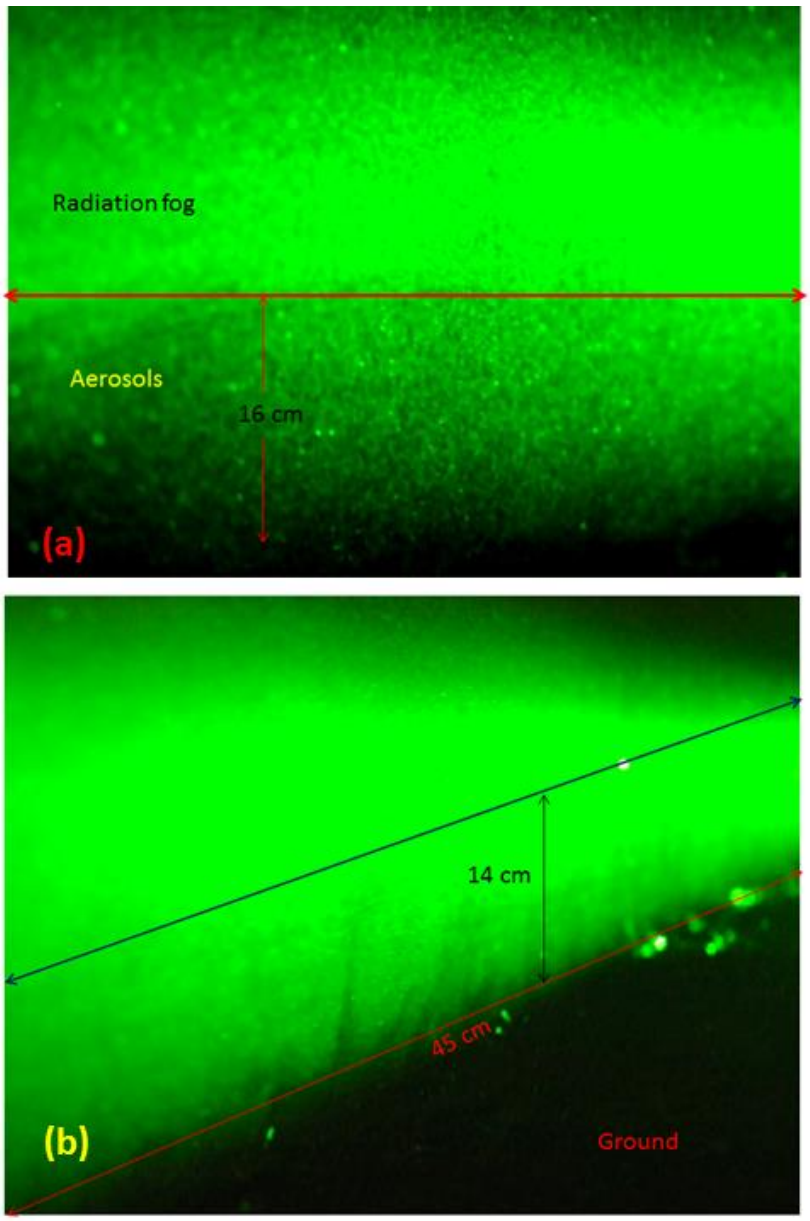

Figure 5.17. (a) The red line is the interface of aerosols and radiation fog, which is around height of LTM. (b) Layers of radiation fog around LTM height.

In the initial stage of formation of radiation fog, the temperature of air layers very close to the ground are approximately unaffected, but the temperature of air layers around the LTM height are changed and as shown in Fig. 5.18.

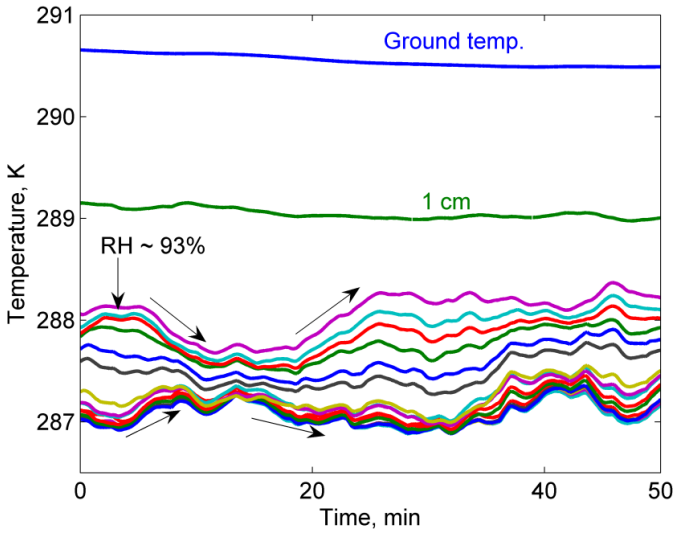

Figure 5.18. The temperature of air layers and the ground temperature are plotted with respect to time during radiation fog.

Many researchers have reported inversion temperature profile near the ground in night-time. They missed out the fact that in calm and cloudless sky conditions, the temperature profile near the ground is not an inversion profile, but an LTM type. In previous reports, before the formation of fog, the temperature profile near the ground is inversion and after fog formation, the ground is shielded by radiation and the ground temperature increases, thereby resulting in the development of convective region near the ground after fog formation. This convection helps to raise the fog upwards. It should be noted that before fog formation, the vertical temperature profile near the ground is LTM type not an inversion, but when fog is formed, the shape of vertical temperature profile is changed. The vertical temperature profiles before and during radiation fog have been plotted and shown in Fig. 5.19. After the formation of radiation fog, the intensity of minimum decreases and it depends upon intensity of fog. When dense fog formed, the ground temperature increased (Fig. 5.20) as well as the temperature of air at about 2 cm to 200 cm became isothermal and even after this the convective region was

present near the ground. This convection helps to raise the fog upwards. For around 15 nights, dense and partial fog was observed near the ground over the high emissivity and high thermal inertia surface.

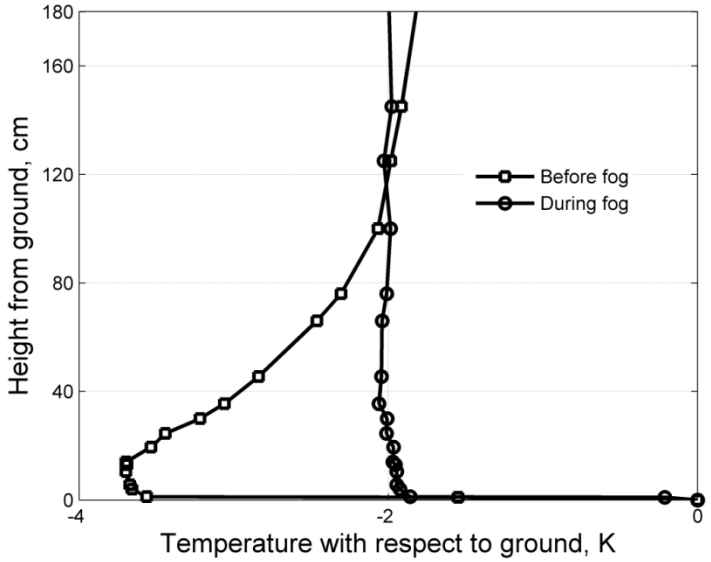

Figure 5.19 The vertical temperature profiles near the surface before and during the radiation fog.

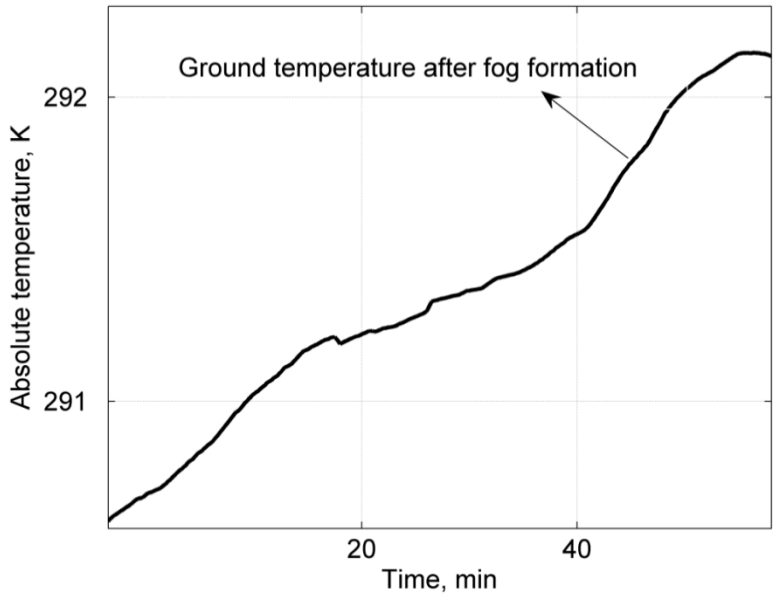

Figure 5.20. The temperature of ground has increased during radiation fog formation.

In Fig. 5.21, temperatures of air layers have been plotted with respect to time during the fog formation. The temperature of air layers below 50 cm change faster than the air layers above 50 cm and that of air layers above 50 cm is more or less constant or changing very less. The radiation fog experiments have also been simulated on grass surface, where intensity and height of minimum are very low. During the radiation fog the temperature of air layers starts increasing and the vertical temperature profile becomes isothermal and is shown in Fig. 5.22. We have reported convection in the LTM region in section 5.5.2. It can be seen that there is convection in the LTM region during the fog formation.

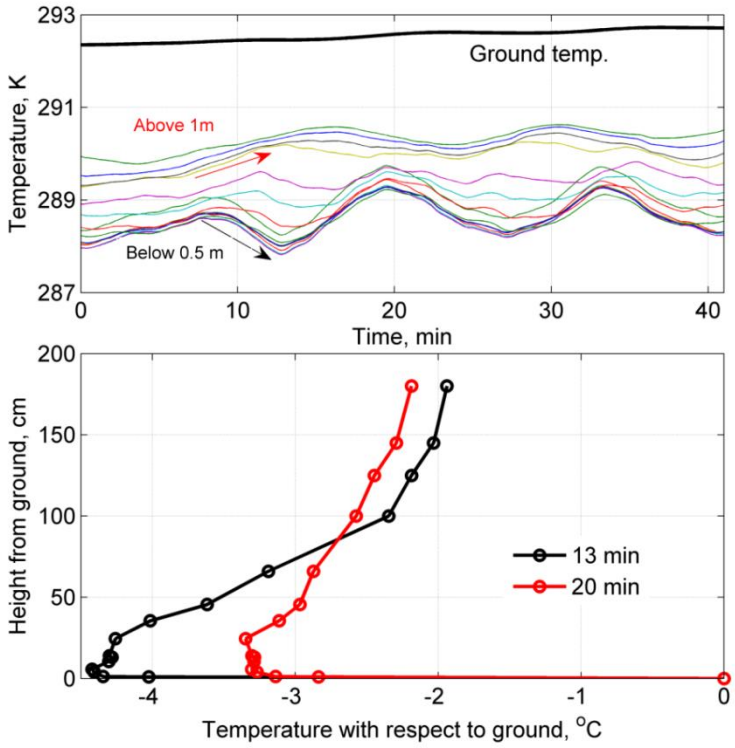

Figure 5.21. The temperature of air layers near the ground is plotted with respect to time during radiation fog and showing more and less temperature fluctuation below and above 50 cm respectively. In the bottom panel, the vertical temperature profiles are plotted before and during radiation fog.

After converting vapor-air into water droplets, these water droplets (fog) reflect more light (more intensity) towards the camera as compared to aerosols. Therefore, during radiation fog, the aerosols look black when compared to fog in the image. In beginning of radiation fog, convection near the ground (in the LTM region) is shown in Fig. 5.23. The developed radiation fog is depicted in Fig. 5.24, which shows that convection near the ground helps to raise the fog up.

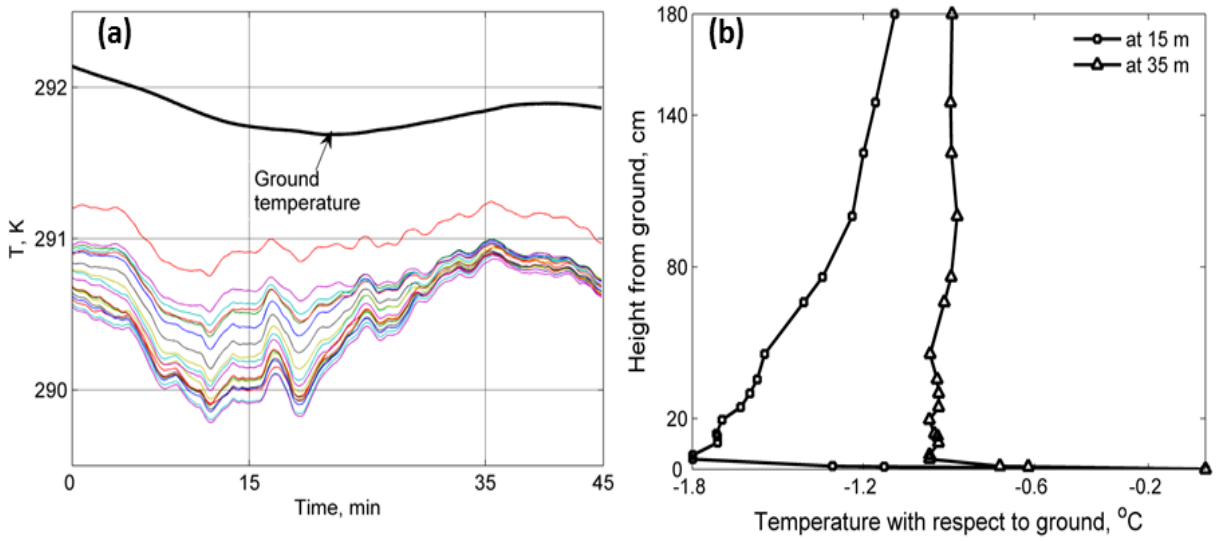

Figure 5.22. (a) The temperature of air layers and the ground temperature are plotted with respect to the time during radiation fog over the grass surface. (b) The vertical temperature profiles after and during radiation fog over grass surface.

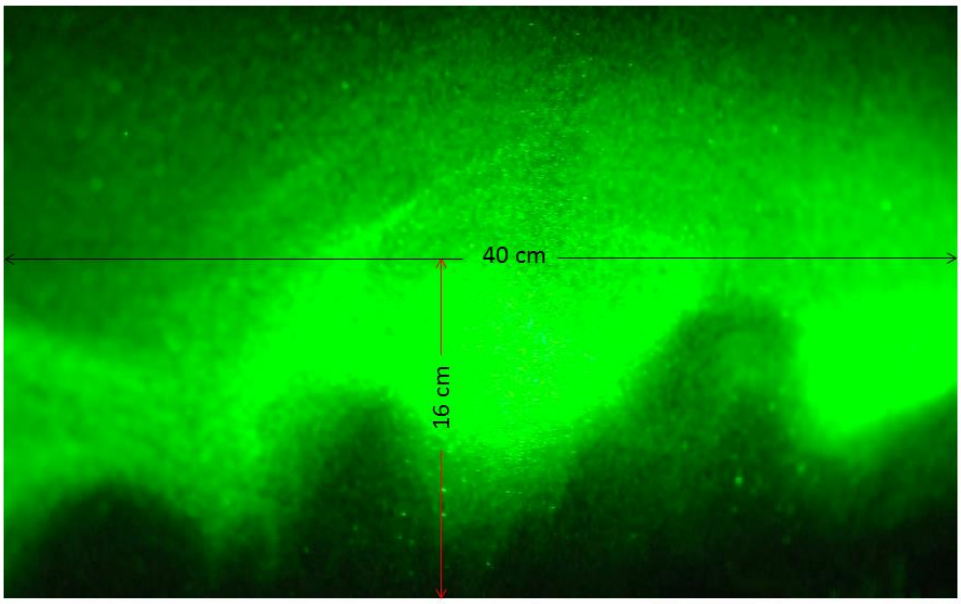

Figure 5.23. Convection rolls at the LTM region in the beginning of radiation fog.

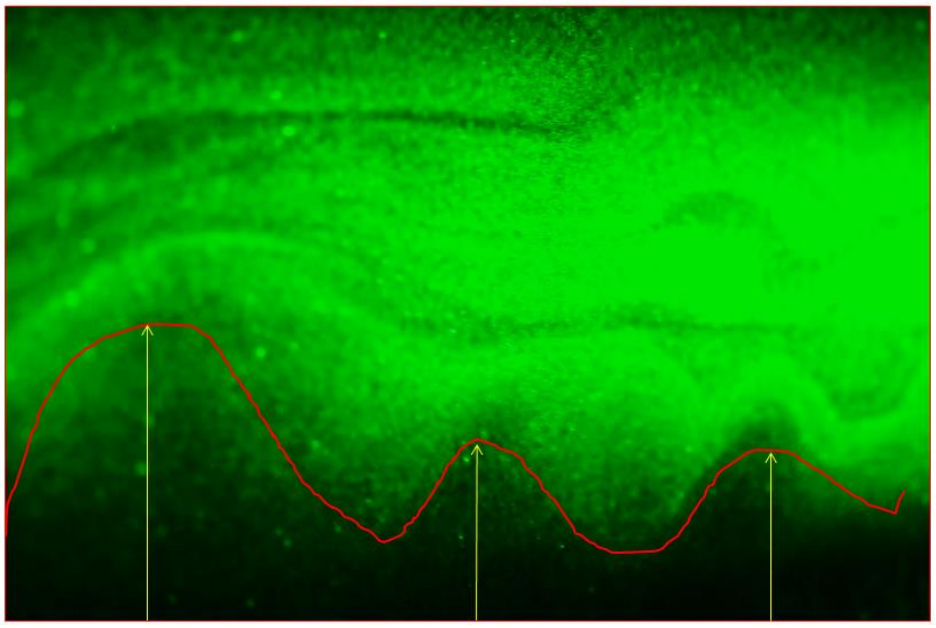

Figure 5.24. Developed radiation fog: layers of fog and convection near the ground.

After (during) formation of radiation fog, the height of convection rolls changes because the temperature profile near the ground becomes flat (isothermal).

From question 5.2, Z_p becomes $\sqrt{-A_3/A_2}$ where A_1 is $\frac{g}{T}\frac{\partial T}{\partial z}\Big|_{z=interface}$

The temperature profile near the ground becomes flat, so $A_1 \sim 0$, Z_p becomes infinite.

The images have been taken during radiation fog, but the maximum vertical height of the laser sheet is around 40 cm. Therefore, the convection length cannot be shown as infinite in the image. In Fig. 5.25, convection rolls go to up to 40 cm in low wind condition.

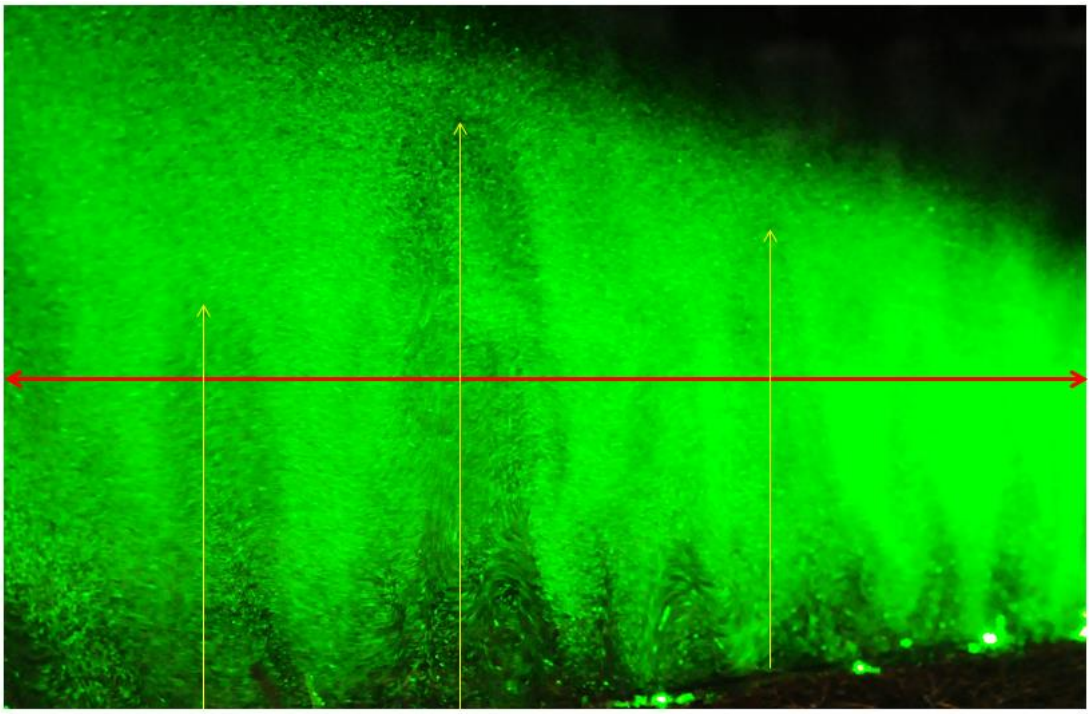

Figure 5.25. Aerosols and radiation fog images; showing convection roll near the ground and fluid parcels are going up to laser sheet.

5.4.3 Effect of rain

A near-surface concentration gradient of suspended aerosols is proposed as the cause for the preferential hyper-cooling and its existence was confirmed by laboratory experiments. This section discusses the similar effects in the field. In the field experiments, however, the aerosols cannot be removed by using an air filter. Performing the experiments under rainy conditions instead reduces the concentration of the aerosol. The effect of seasons on the intensity of minima has been observed and discussed previously in the thesis. We showed that the intensity of minimum depends on the aerosols' concentration, specifically being maximum during pre-monsoon and minimum during monsoon. During the rains, aerosols settle down to the ground and it is the best way to reduce the aerosol concentration in the field experiments.

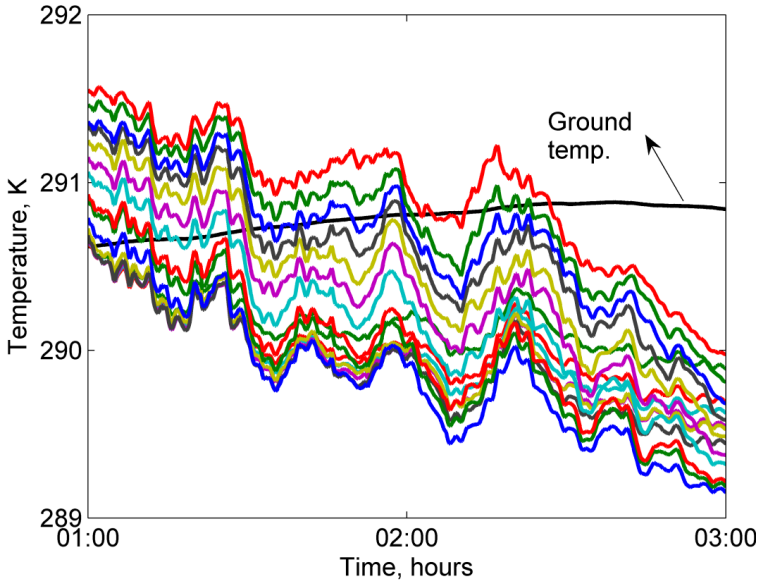

Figure 5.26. The temperature of air layers and the ground temperature after rain for aduration of half an hours.

In order to have conditions similar to those in the laboratory (variation of aerosol concentration), another set of parameters need to be considered along with rain in field experiments. In particular, the sky should be clear and the wind speed should be below threshold. Such ideal conditions were obtained on two nights and the results are shown in the following sections.

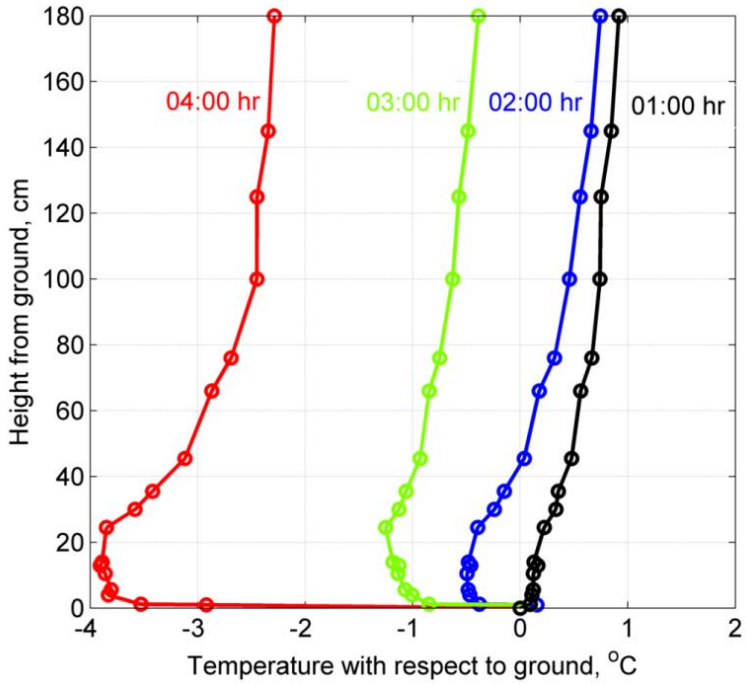

Figure 5.27. The vertical temperature profiles at various durations after rain.

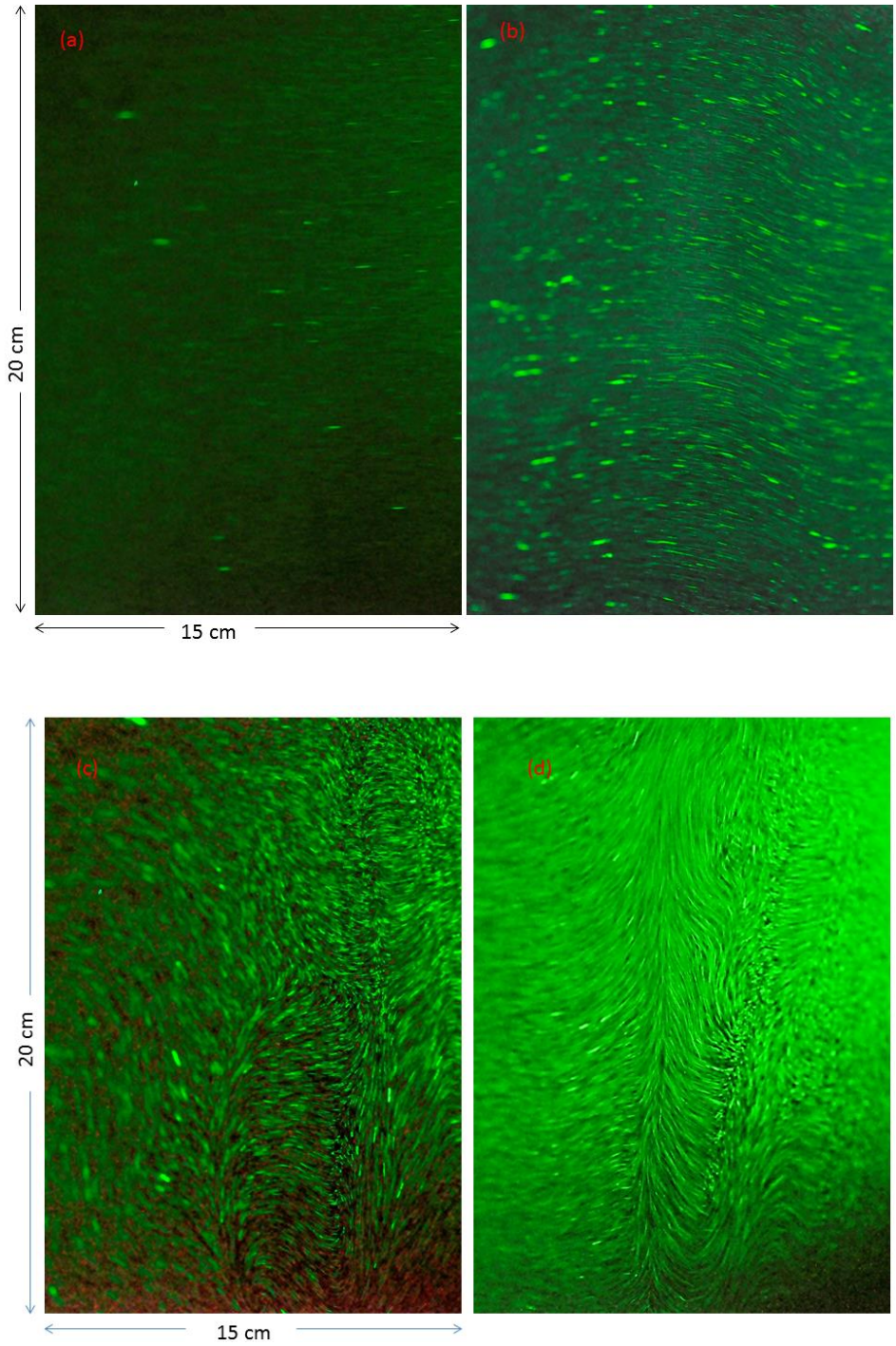

Figure 5.28. The aerosols' images after rain (a) At 01:00 hr. (b) At 02:00 hr. (c) At 03:00 hr., and (d) At 04:00 hr.

On 15th January 2012, at around 2100 hours, it rained for 30 minutes and the sky was clear at 0100 and the experiment was begun. In Fig. 5.26, the temperature of the air layer and ground are plotted with respect to time. The vertical temperature profile near the ground at 0100 is almost isothermal (no LTM). After sometime, the vertical profile near the ground was observed to have shifted from isothermal to an LTM type. The intensity of minimum increased with time as shown in Fig. 5.27. The corresponding aerosol images are shown in Fig. 5.28. The aerosol number density also increased with time.

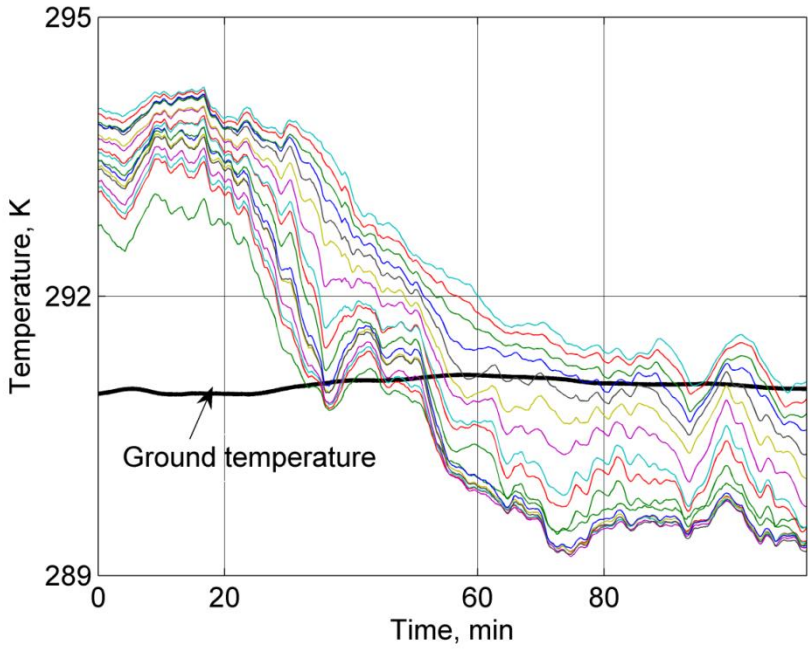

Figure 5.29. The temperature of air layers and the ground temperature after heavy rain.

The same phenomenon was observed on another night, where more heavy rainfall had occurred and hence the surface was wet. In this case as well, the profile near the ground was initially an inversion-type and shifted to an LTM-type after some time. In Fig. 5.29, the

temperature of air layer and ground are plotted with respect to time. The inversion temperature profile shifted to LTM type profile after some time and is shown in Fig. 5.30.

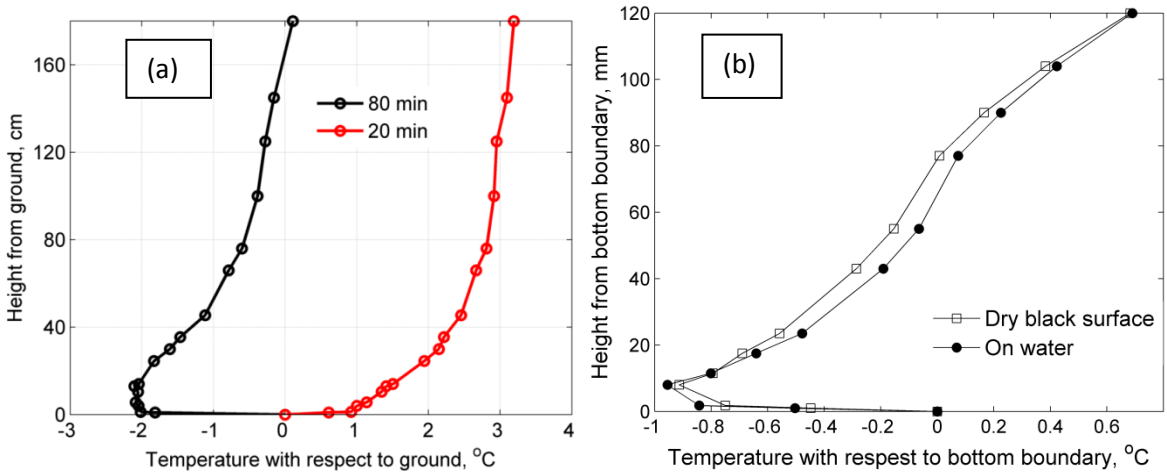

Figure 5.30 (a) The vertical temperature profiles at various durations on wet surface in field experiment. (b) The vertical temperature profiles in the test section in the laboratory on dry surface and over 5 mm deep water layer.

For instance in our observation presented in Fig. 5.30a, even though LTM is absent at 20 min after the rain event, LTM has reemerged after 80 min, note that the ground is still wet. To get the clarity on the role of wet surface in determining the formation of LTM, we carried out an experiment over the 5mm deep water layer in the laboratory. First, an experiment was performed over dry, black Aluminum surface and LTM was obtained (see Fig 5.30b). Later, in the same setting water was filled up to 5mm depth in the bottom tray and the experiment was repeated. Now the reference level for the temperature measurements is the upper surface of the water layer. In this case also we obtained LTM profile as shown in the Fig. 5.30b. The result is not surprising, if one looks into this result in terms of Ramdas-Zdunkowski factor, the R_{Zf} value for the water surface is similar (>>1) to that for the black-painted Aluminum surface, hence we expect to observe an LTM. Other factor is the occurrence of a week-LTM

over a grass surface as in the cases of present observation (Fig 5.22b) and in the study of Oke (1970), who talks about grass-tip minima. In the Steeneveld et al, (2010) study temperature measurements close to the ground is at 10cm height (T_{Veg}) and next one is at 1.5m height ($T_{1.5m}$), thus here also we cannot rule out the presence of a week minima. The reason for a week minima over a grass-surface could be understood by again appealing to the Ramdas–Zdunkowski factor (R_{zf}). Grass surface has a low thermal inertia, hence R_{zf} will be small, similar to thermofoam surface studied in the laboratory, hence as presented in the Chapter-2, we are expected to get a week minima over grass surface.

5.5. Conclusion

The field experiments were carried out over bare soil ground with surface properties of high emissivity and high thermal inertia. In addition to measures of vertical temperature profile, wind speed, humidity, and image of aerosols were monitored. The observations showed that wind speed and turbulence levels have a strong effect on the LTM type profile. The magnitude of temperature gradient and radiative flux divergence just above the ground is very high and decreases with decreasing intensity of minimum. The calculated Rayleigh number for this layer (the ground to LTM height) based on intensity and height of minimum are varied from O (10^4) to O (10^6) and in this region, at low wind condition, convection motion is observed. The height of formation of convection rolls is around LTM height and the estimated penetrating length is matching well with experimental observations. We have also observed that the formation of radiation fog occurs around the LTM height, rather than on the ground and presence of aerosols must be model for predicting radiation fog. The LTM-type profile plays an important role in the formation of radiation fog. During the radiation fog, LTM-type profile should be different and height of convection rolls becomes infinite. Finally we have also observed the effect of rain. After rains, aerosols settle down on the ground, and the resulting vertical temperature profile is an inversion-type.

CHAPTER 6

Conclusion

The present thesis has focused on the role of aerosol and radiative heat transfer in the nocturnal atmospheric boundary layer. Detailed discussion and conclusions are provided at the end of the each chapter. Here, we summarize important conclusions from the present study.

In chapter 2, we show that the formation of an LTM type profile in the nocturnal boundary layer is a norm under calm and clear sky conditions. The occurrence of such a profile implies that, after the sunset, the near-surface air layers (rather than ground) cool faster and thereby, drive the cooling process. LTM type profiles have been re-produced for different bottom boundary conditions in the laboratory. Results indicate that the intensity of the minimum, over a low emissivity boundary is approximately double compared to that over a high emissivity bottom boundary and is similar to earlier observation in the field. Important result from our experiments is the demonstration that the suspended aerosol particles are indeed necessary to explain the origin of LTM profile, thus solving an eighty year old micro-meteorological mystery. The presence of aerosols, not normally accounted for in radiation models, resolves the apparent contradiction between observations of radiative cooling presented here, and theoretical predictions reported earlier of near-surface warming in a homogeneous atmosphere. The existence of the near-surface heterogeneity (leading to the LTM) provides a natural explanation for the observed hyper-cooling. In the nocturnal atmospheric boundary layer, we define a new a non-dimensional parameter called Ramdas –

Zdunkowski factor (R_{zf} , which is the ratio of air and ground cooling rates) which determines the type of temperature profile (LTM or inversion).

In chapter 3, the experimental observation for the equilibrium temperature profiles arising in a radiatively participating heterogeneous medium (the heterogeneity arising due to the presence of suspended aerosols) sandwiched between two horizontal plates have been presented. Our observations show a significant deviation of the equilibrium profiles from the linear conduction profile due to radiation forcing caused by aerosols. Maximum deviation from the conduction profile is observed when the aerosol concentration is high corresponding to pre-monsoon dry conditions, and the deviation is 2.5 times greater than that for air with less aerosols during monsoon. A symmetric temperature profile is exhibited for air with a uniform distribution of aerosols, along with top and bottom boundaries having same emissivity. However, an asymmetric temperature profile is observed for the case of differing boundary emissivities at top and bottom, and also for the case of identical boundary emissivities with an inhomogeneous aerosol distribution.

In chapter 4, experiments with decoupled boundary conditions for radiation and conduction, and effect of aerosol-forcing on the onset of convection were investigated. In these experiments with aerosol laden air layer, under normal atmospheric pressure and temperatures, we demonstrate that the critical Rayleigh number for the onset of convection can be enhanced by up to seven times more than that for the case of standard Rayleigh-Bénard convection, through radiation stabilization. This has been explained by faster time response of the system (determined experimentally) and modified temperature profiles with reduced temperature gradient at the core region due to radiative-forcing. Even when the

convection is observed, both the convective velocities and the temperature fluctuations are markedly lower due to radiation-stabilization compared to those observed in standard Rayleigh-Bénard convection with similar Rayleigh number.

In chapter 5, in the field experiments, the estimated Rayleigh number for the LTM-layer, based on the intensity and height of the minimum are in the range of 10^4 to 10^6. . When turbulence levels were lower, convection rolls were observed in the LTM-region. The height of convection rolls is around LTM-height and the estimated penetrating height into the inversion layer matches well with experimental observations. In the field, radiation fog occurs at few decimeters above the ground (around LTM height) rather than touching the ground, also during this period the ground temperature is much higher than the dew point temperature. Thus, we show that the presence of aerosols must be modeled for predicting the formation radiation fog. The vertical temperature profiles near the surface shows a marked difference before and during the fog period. The results presented in the thesis thus helps in the parameterization of transport process in the NBL, and highlight the need for accounting the effects of aerosols and ground emissivity in climate models and in modeling other micro-meteorological processes.

REFERENCES

AGARWAL, P. Y., AK, GULATI, A. RAMAN, S. RAO, S., SINGH, MP. NIGAM, S. ,AND REDDY, N. (1995), Surface layer turbulence processes in low wind speeds over land. *Atmos. Environ, 29* 2089–2098.

ALBANI, F. (1951), Investigaciones sobre la distribuci´on vertical de las temp. minimas en las capas de aire pr´oximas al suelo. Arch. , *Fitot´ecnico del Uruguay, 4*, 361–376.

ANFOSSI, D. B. P., AND LONGHETTOS, A. (1976), Forecasting of vertical temperature profiles in the atmosphere during nocturnal radiation inversions from air temperature trend at screen height, Quart. J. R. Met. Soc., 102, 173-180.

ARPACI, V. S., AND GOZUM, D. (1973), Thermal stability of radiating fluids, the b´enard problem. 16-5, 581–588.

AUDUNSON, T., AND GEBHART, B. (1972), An experimental and analytical study of natural convection with appreciable thermal radiation effects, *J. Fluid. mech., 52*(1), 57-95.

ANDRE J C, A. M. L. (1981), The nocturnal surface inversion and influence of clear-air radiative cooling. *J. Atmos. Sci., 39*, 864–878.

ANFOSSI, D. O. D., DEGRAZIA G, AND GOULART A. (2005), An analysis of sonic anemometer observations in low wind speed conditions. *Bound. Lay. Meteorol. , 114-1*, 179–203.

BHAT, G. (2006), Near-surface temperature inversion over the Arabian sea due to natural aerosols. *Geophys. Res. Lett., 33*, L02802.

BRAWAND, H., AND KOHNKE, H. (1952), Micro-climate and water vapor exchange at the soil surface. *Proc. Soil. Sci. Soc. Amer, 16*, 195–198.

BDEOUI, F., AND SOUFIANI, A. (1997), The onset of rayleigh-bernard instability in molecular radiating gases, *Phys.Fluids 9-12*, 3858–3872.

DAVIS, J. R., F. K. (1957), Publications in climatology, 10, 1-37.

DYER, A. (1963), The adjustment of profiles and eddy fluxes, *Q.J.R. Meteorol. Soc., 89*, 276–280.

CHRISTOPHORIDES, C., AND DAVIS, S. H. (1970), Thermal instability with radiative transfer, *Phys.Fluids 13*, 222.

CHANDRASEKHAR, S. (1981), Hydrodynamic and hydromagnetic stability. *Dover*, 652

DEARDORFF, J. W., (1970) Convective velocity and temperature scales for the unstable planetary boundary layer and for Rayleigh convection. J. Atmos. Sci., 27, 1211-1213.

DEVARA, P., and RAJ, P. (1993), Lidar measurements of aerosols in the tropical atmosphere. *Advances in Atmospheric Sciences*, *10*(3), 365-378.

DEVARA, P. C. S., AND ERNEST, RAJ P. (1993), Lidar measurements of aerosols in the tropical atmosphere. *Advan. Atmos. Sci*, *10*(3), 365-378.

DEVARA, P. C. S. and RAJ P. (1997), A lidar study of atmospheric aerosols during two contrasting monsoon seasons. *Atmosfera., 11*, 199-204.

EDWARDS, J. (2009), Radiative processes in the stable boundary layer: Part I. Radiative aspects. *Bound. Lay. Meteorol*, *131*, 105–126.

EZEKWE, C. (1986), Nocturnal radiation measurements in Nigeria. *Solar Energy*, *37* (1), 1-6.

FLEAGLE, R. G. (1953), A theory of fog formation. *J. Mar. Res.*, *12*, 43–50.

FLEAGLE, R. G. (1955), The temperature distribution near a cold surface, *J. atmos. Sci. , 13-2*, 160–165.

FUNK, J. (1960), Measured radiative flux divergence near the ground at night. *Q. J. Roy. Meteorol. Soc.*, *86*, 383–389.

FERNANDO, H. J. S., (1991), Turbulent mixing in stratified fluids. Anuu. Rev. Fluid Mech. 23, 455–493.

GARRATT, J. R. A. B., R. A. (1981), Radiative cooling effects within and above the nocturnal boundary layer, *J. Atmos Sci.*, *38*, 2730–2746.

GEIGER, R. (1995), The climate near the ground. *Harvard University Press*.

GOODY, R. (1956), The influence or radiative transfer on cellular convection. *J. Fluid. mech.*, *1*, 424–435.

GILLE, J. AND GOODY, R. M. (1964), Convection in a radiating gas. *J. Fluid. mech.*, *20-1*, 47–79.

GRAF, W. H., and CELLINO, M. (2002), Suspension flows in open channels; experimental study. *Journal of Hydraulic Research*, *40*(4), 435 - 447.

HA, K., AND MAHRT, L. (2003), Radiative and turbulent fluxes in the nocturnal boundary layer. *Tellus*, *55A*, 317–327.

HOCH, S. W. (2005), Radiative flux divergence in the surface boundary layer, a study based on observations at summit, greenland. PhD thesis, Swiss Federal Institute of Technology ETH, Zurich, Zurich, Switzerland.

HUTCHISON, J. E., AND RICHARDS, RF. (1999), Effect of nongray gas radiation on thermal stability in carbon dioxide. *J.Thermophys Heat.tr.*, *13-1*, 25–32.

JOSEPH, D.D. (1965) Nonlinear stability of the Boussinesq equation by the method of energy. Arch. Ration. Mech. Anal., 22, 163-184.

LAKE, J. (1956), The temperature profile above bare soil on clear nights. *Q. J. Roy. Meteorol. Soc.*

LUTZKE, R., (1960), Unter welchen bedingungen hebt sich das nachtliche, temperatur minimum von der bodenoberflache ab? , *Anggewandte Met.* , *4* 1–10.

LIESKE, B. J. A. A. S. L., (1967), Measurements of radiative flux divergence in the arctic, *J. Clim. Appl. Meteorol.* , *15*(1-2), 67–81.

LETTAU, H. (1979), Wind and temperature profile prediction for diabatic surface layers including strong inversion cases. *Bound.-Lay. Meteorol.* , *17*, 443–464.

LIESKE, B. J. AND A. A. STROSCHEIN, L. (1967), Measurements of radiative flux divergence in the arctic. *J. Clim. Appl. Meteorol.* , *15*(1-2), 67–81.

LARSON, V., (2000), Stability properties of and scaling laws for a dry radiative-convective atmosphere, *Q. J. Roy. Meteorol. Soc.*, *126*, 145–171.

LARSON, V., (2001), The effects of thermal radiation on dry convective instability, *Dyn. Atmos. Oceans*, *34*, 45–71.

LIOU, K. N., (2002), An introduction to atmospheric radiation, *Academic Pres, N.Y.*

LIU, W. W., PY. LIU, WY. LI, JT., AND LI ,PJ. (2008), The importance of radiation fog in the tropical seasonal rain forest of xishuangbanna, south-west china.. , *Hydr.Res.*, *39-1*, 79–87.

M. MURGAB AND P. KHOLO (1962). A study of the combined effect of thermal radiative transfer and a magnetic field on the gravitational convection of a ionized fluid, J. Fluid Mech. 14, 433.

MUKUND, V. (2008), Field observations and laboratory simulation of the lifted temperature minimum. *Ph.D. thesis, Jawaharlal Nehru Centre for Advanced Scientific Research, Bangalore, India.*

MUKUND, V., PONNULAKSHMI, VK., SINGH, DK., SUBRAMANIAN, G., AND SREENIVAS, KR. (2010), Hyper-cooling in the nocturnal boundary layer: the Ramdas paradox. *Phys.Scripta, T142*, 014041.

MUKUND, V., SINGH, D. K., PONNULAKSHMI, V. K., SUBRAMANIAN, G. ,AND SREENIVAS, K. R. (2013), Field and laboratory experiments on aerosol-induced cooling in the nocturnal boundary layer, *Q.J.Roy.Meteor.Soc.*

NOVOTNY, J. L., AND OLSOFKA, F. A. (1970), The influence of a non-absorbing gas in a radiation conduction interaction, *AIAA 5th Thermophysical Conference.*

NOVOTNY, J. O. F. A., AND SCHIMMEL, WP. (1970), Interferometric study of radiation-conduction interaction, *Proc. 4th int. Heat Transfer Conference*.

NARASIMHA, R. (1994), dynamics of the ramdas layer. *Curr. Sci. , 66*, 16–23.

NARASIMHA, R., AND VASUDEVAMURTHY, A. S. (1995), The energy balance in the ramdas layer. *Bound.-Lay. Meteorol 76*, 307–321.

NIELSEN, P., and TEAKLE, I. A. L. (2004), Turbulent diffusion of momentum and suspended particles: A finite-mixing-length theory. *Physics of Fluids*, *16*(7), 2342-2348.

NKEMDIRIM, L. (1978), A comparison of radiative and actual nocturnal cooling rates over: grass and snow. *J. Appl. Meteorol*, *17-11*, 1643–1646.

OKE, T. R. (1970), The temperature profile near the ground on calm clear nights. *Q. J. Roy. Meteorol. Soc.*, *96*, 14–23.

P. KHOLO AND M. MURGAB, (1963), A study of the combined effect of thermal radiative transfer and rotation on the gravitational stability of a hot fluid, J. Fluid Mech. 16, 97.

PONNULAKSHMI, V., SINGH, D.K., MUKUND, V., SREENIVAS, K.R. ,AND SUBRAMANIAN, G. (2012a), Hypercooling in the atmospheric boundary layer: beyond broadband emissivity schemes, *J. Atmos. Sci.*

PONNULAKSHMI, V., MUKUND, V., SINGH, D.K., SREENIVAS, K.R. ,AND SUBRAMANIAN, G. (2012b), Hypercooling in the Nocturnal Boundary Layer: Broadband Emissivity Schemes, *J. Atmos. Sci.*

PRASANNA, S., (2012), Studies on the effects of surface radiation and radiation in participating medium on natural convection, *PhD thesis, Indian Institute of technology Madras, Bangalore, India*.

PONNULAKSHMI, V. K. (2013), The role of radiation in the nocturnal boundary layer: the origin of the lifted temperature minimum, *PhD thesis, Jawaharlal Nehru Centre for Advanced Scientific Research, Bangalore, India.*

PONNULAKSHMI, V. K., G. SUBRAMANIAN, V.MUKUND, AND K.R. SREENIVAS (2009), The Ramdas layer remains a micro-meteorological puzzle. *Jawaharlal Nehru Centre for Advanced Scientific Research*(Rep. JNCASR/EMU/2009-1), 41 pp.

ROUSE, H., (1937), Nomogram for the settling velocity of spheres. In: Division of Geology and Geography, Exhibit D of the Report of the Commission on Sedimentation, *National Research Council, Washington, D.C.*, 57-64.

RIDER, N. E., AND ROBINSON, G.D., (1951), Quart. J. R. Met. Soc., 77, 375.

R¨AIS¨ANEN, P., (1996), The effect of vertical resolution on clear-sky radiation calculations: tests with two schemes, *Tellus 48-3*, 403–423.

RAGOTHAMAN, S., NARASIMHA, R. ,AND VASUDEVAMURTHY, A. (2001), The dynamical behavior of the lifted temperature minimum. *Il Nuovo Cimento 24*, 353–375.

RAMDAS, L. (1953), Convective phenomena near a heated surface. *Proc. Indian. Acad. Sci., A-37*, 304–316.

RAMDAS, L. A., AND ATMANATHAN, S. (1932), The vertical distribution of air temperature near the ground during night. *Beitr. zur Geophysik 37*, 116–117.

RASCHKE, K. (1957), ¨ Uber das n¨achtliche temperaturminimum ¨uber nackten boden in poona. *Met. Rundschau, 10*, 1–11.

RYDER, E. J., AND ROBINSON, B. J., (1991), Pacific lettuces, *Hort Science 26*, 437–438.

RAJ, P., DEVARA, PCS. , MAHESKUMAR, RS. , PANDITHURAI, G., AND DANI, KK (1997), Lidar measurements of aerosol column content in an urban nocturnal boundary layer Atmos. Res., 45(3), 201–216.

RAMANATHAN, V. AND P.J.CRUTZEN (2003) New directions: Atmospheric Broun Clouds. Atmos. Environ., 37, 4033-4035.

STEWART, K.H., (1955), Radiation fog: Investigation at Cardington. Met. Res. Cttee. (London), 1951-54.

SPIEGEL, E., (1957), The Smoothing of Temperature Fluctuations by Radiative Transfer, *Astrophys J., 126*, 202-207.

SAVITZKY, A., AND GOLAY, M.J.E., (1964), Smoothing and differentiation of data by simplified least square procedures, *Anal.Chem., 36*, 1627-1639.

SCHIMMEL, W. P., N. J. L. AND OLSOFKA, F. A. (1970), Interferometric study of radiation-conduction interaction, *In Proceedings of the 4th International Heat Transfer Conference, 3. Elsevier*.

SREENIVAS, K. R., DEY, P. K., ARAKERI, J. H., SRINIVASAN, J., (1995), Study of the erosion of stably stratified medium heated from below. Fourteenth International Conference on Numerical Methods in Fluid Dynamics Lecture Notes in Physics, 453, 551-555.

SAVIJÄRVI, H. (2006), Radiative and turbulent heating rates in the clear-air boundary layer. *Q.J. Roy. Meteorol. Soc. , 132*, 147–161.

SIEGEL, R., AND HOWELL, J. R. (2002), Thermal radiation heat transfer *Taylor and Francis, N.Y.London.*

SNYDER, W., WAN, Z., ZHANG, Y., AND FENG Y. (1998), Classification-based emissivity for land surface temperature measurement from space. *Int.J.Remote.Sens., 19-14*, 2753–2774.

SOULSBY, R. (1997), Dynamics of Marine Sands: a manual for practical application. *Thomas Telford, London, ISBN 0-7277-2584-X.*

STULL, R. (1988), An introduction to boundary layer meteorology, *Springer*, 670.

STEENEVELD, G. J. (2007) Understanding and prediction of stable atmospheric boundary layers over land. PhD thesis, Wageningen Universiteit, Netherlands.

STEENEVELD, G. J., WOKKE, M.J.J, GROOT ZWAAFTINK, C.D, PIJLMAN, S., HEUSINKVELD, B.G., JACOBS, A.F.G., AND HOLTSLAG, A.A.M. (2010) Observatios of the radiation divergence in the surface layer and its implication for its parameterization in numerical weather prediction models. Journal of Geophysical Reasearch, Vol. 115, D06107,doi:10.1029/2009JD013074,2010.

SUN, J., BURNS, S.P., DELANY, A.C., ONCLEY, S.P., HORST, T.W., AND LENSCHOW, D.H. (2003), Heat Balance in the Nocturnal Boundary Layer during. CASES-99, *J.Appl.Meteorol., 42* 1649-1666.

TAYLOR, G. I. (1917), The formation of fog and mists, Quart. J. R. Met. Soc., 43, 241-268.

TIWARI, P., (2006), Laboratory simulation of lifted temeprature minimum, *PhD thesis, Jawaharlal Nehru Centre for Advanced Scientific Research, Bangalore, India*.

VARGHESE, S. (2003), Band model computation of near-surface long wave fluxes. *Ph.D. thesis, Jawaharlal Nehru Centre for Advanced Scientific Research, Bangalore, India*.

VARGHESE, S., VASUDEVAMURTHY, A. S., AND NARASIMHA, R. (2003b), A fast accurate method of computing near-surface longwave fluxes and cooling rates in the atmosphere. *J. Atmos. Sci., 60*, 2869–2886.

VASUDEVAMURTHY, A. S., R.NARASIMHA, AND S.VARGHESE (2005), An asymptotic analysis of a simple model for the structure and dynamics of the ramdas layer, *Pure Appl. Geophys*, *162* 1831–1857.

VASUDEVAMURTHY, A. S., SRINVASAN, J. & NARASIMHA, R. (1993), A theory of the lifted temperature minimum on calm clear nights, *Proc. Roy. Soc. Lond*, *23*, 183–206.

WHITEHEAD, J., AND CHEN, M.M., (1970), Thermal instability of a thin fluid layer bounded by a stably stratified region, *J. Fluid. Mech*, *40*, 549–576.

ZDUNKOWSKI, W., HENDERSON, D., AND HALES, J., (1966), The effect of atmospheric haze on infrared radiative cooling rates, *J. Atmos. Sci. , 23*, 297–304.

ZDUNKOWSKI, W., (1966a), The nocturnal temperature above the ground, *Beitr.Phys.Atmos*, *39*, 247–253.